PhD Thesis

Institute of Physical Chemistry
Polish Academy of Sciences

Kasprzaka 44/52
01-224 Warsaw, Poland

PhD Thesis

Electrochemical preparation of Ag- and Au-based plasmonic platforms

Marta Maria Siek

Supervisor: dr hab. inż. Joanna Niedziółka-Jönsson

This dissertation was prepared within the International PhD Studies
at the Institute of Physical Chemistry of the Polish Academy of Sciences in Warsaw

Warsaw, July 2015

Acknowledgments

I would like to express my sincere gratitude to:

my supervisor, *Dr. Eng. Joanna Niedziółka-Jönsson*, for introducing me to the world of plasmonics and electrodeposition,

Prof. Marcin Opałło for encouraging me to start this "PhD journey",

Prof. Sabine Szunerits and *Prof. Rabah Boukherroub* from for their support, kindness and fruitful discussions during my stay in Lille,

Dr. Marcin Koba from the National Institute of Telecommunications for silica layers,

co-authors of my publications for their commitment to our research and for all the knowledge they shared with me,

my students – *Eng. Beata Szydłowska* and *Marta Podrażka* – for teaching me how to teach and for their great contribution to our research.

I am also very grateful to my colleagues for all discussions (not only work-related) and really nice atmosphere at the workplace.
Big „thank you" for *Ewa R., Wojciech A., Wojciech N., Marta J., Martin J.-N., Tomek A., Michalina I., Janek P., Kinga M* and *Witek A.* Your support was invaluable!

Specjalne podziękowania należą się *mojej Rodzinie* – za oparcie jakie w Was zawsze mam; za motywowanie mnie do pracy, nawet kiedy nie mam sił otworzyć oczu; za wspieranie mnie w moich decyzjach, nawet jeśli się z nimi nie zgadzacie.
Dziękuję, że jesteście!

The work was supported by:

- the project FOCUS F3/2010/P/2013 operated within the Foundation for Polish Science

- the project LIDER Lider/15/24/L-2/10/NCBiR/2011 operated within the National Centre for Research and Development

- the project NOBLESSE FP7-REGPOT-CT-2011-285949-NOBLESSE operated within the Seventh Framework Programme of the European Union

- the project Bio-SERS PBS2/A1/8/2013 operated within the Applied Research Programme of the National Centre for Research and Development

Abstract

Plasmonic-based sensors are valuable tools in studying molecular interactions and label-free detection in real time to mention just a few examples. Used setups are relatively simple and can be miniaturized and integrated. Their crucial element is the sensing platform. This dissertation was focused on the fabrication of Ag- and Au-based platforms showing a narrow plasmon resonance peak in the UV-Vis spectrum and high refractive index sensitivity for use in localized surface plasmon resonance (LSPR), and/or a high enhancement factor for use in surface enhanced Raman spectroscopy (SERS). The fabrication method of choice was electrodeposition. It allows the growth of particles of specified size, shape and properties in a very precise and cheap manner. Potentiodynamic methods were chosen, specifically cyclic voltammetry, to grant the possibility of tuning the number of nucleation and growth steps (with the number of cycles used) as well as the relaxation time of the system (with changing the scan rate). The use of the environmentally-friendly reducing agents, as citrate ions and glucose, was preferred because of their harmlessness and lack of reports about usage in potentiodynamic methods.

A broad range of applications of obtained platforms in plasmonic methods was shown. Fabricated platforms exhibited very high SERS enhancement factors (EF) therefore it was possible to record SERS spectra of neurotransmitters in physiologically relevant concentrations. In the field of LSPR it was possible to study molecular interactions with lectins-to-sugars binding. Also, developed platforms were sensitive enough to sense the difference in dielectric coefficient between Gram-positive and Gram-negative bacteria. Moreover, it was possible to differentiate bacteria according to their viability. As last, the proof-of-concept of a biosensor was shown, where T7 bacteriophages were recognized with specific antibodies covalently bound to the platform.

Streszczenie

Czujniki oparte o struktury plazmoniczne metali wykorzystywane są, m.in. do badania oddziaływań molekularnych oraz bezznacznikowego oznaczania analitów w czasie rzeczywistym. Struktury te odpowiadają za przetworzenie sygnału chemicznego na sygnał optyczny. Niniejsza dysertacja miała na celu opracowanie podłoży opartych na strukturach srebra lub złota, wykazujących wąski pik rezonansowy w spektrofotometrii UV-Vis i wysoką czułość na zmiany współczynnika dielektrycznego (do zastosowań w zlokalizowanym rezonansie plazmonów powierzchniowych, LSPR) oraz/lub wykazujących wysokie współczynniki wzmocnienia w powierzchniowo wzmocnionej spektroskopii Ramana (SERS). Podłoża wytwarzano w procesie elektroosadzania. Jest to prosty i tani sposób umożliwiający wzrost cząstek o pożądanych właściwościach. Aby zapewnić kontrolę nad ilością cykli zasiewanie-wzrost oraz czasem relaksacji systemu, wybrano metodę potencjodynamiczną – woltamperometrię cykliczną. Zastosowane substancje redukujące (jony cytrynianowe oraz glukoza) zostały wybrane ze względu na swoją nieszkodliwość dla środowiska oraz brak doniesień literaturowych nt. stosowania ich do elektroosadzania nanocząstek metali metodami potencjodynamicznymi.

W dysertacji zaprezentowano przykłady zastosowań otrzymanych podłoży. Ze względu na uzyskanie wysokich współczynników wzmocnienia możliwym było zarejestrowanie widm SERS neuroprzekaźników w stężeniach fizjologicznych. Zastosowanie w technice LSPR pozwoliło na badanie oddziaływań molekularnych na przykładzie układu lektyna-cukier. Ponadto, wysoka czułość uzyskanych platform pozwoliła na badanie różnic we współczynnikach dielektrycznych bakterii Gram-dodatnich i Gram-ujemnych, a także na różnicowanie bakterii ze względu na ich żywotność. Jako ostatni przykład przedstawiono prototyp immunoczujnika do wykrywania bakteriofagów T7.

Major abbreviations

η overpotential

$\Delta\mu$ electrochemical saturation

i current density

E potential

E_{crit} critical nucleation potential

ITO indium-tin oxide

CV cyclic voltammetry

AuNPs gold nanoparticles

AgNPs silver nanoparticles

NPs nanoparticles

AAO anodized aluminum oxide

PVP poly(vinylpirrolidone)

SPR surface plasmon resonance

LSPR localized surface plasmon resonance

λ wavelength

n refractive index

SERS surface enhanced Raman spectroscopy

EF enhancement factor

AEF analytical enhancement factor

SSEF SERS substrate enhancement factor

SMEF single molecule enhancement factor

RIS refractive index sensitivity

RIU refractive index unit

SCE standard calomel electrode

4-ATP 4-aminethiophenol

SEM scanning electron microscopy

CCD charge-coupled device

LC lectin from *Lens culinaris*

MA lectin from *Maackia amurensis*

FWHM full width at half maximum

K_a acid dissociation constant

pI isoelectric point

AgCitNPs silver nanoparticles electrodeposited from solution containing citrate ions

AuCitNPs gold nanoparticles electrodeposited from solution containing citrate ions

GO graphene oxide

rGO reduced graphene oxide

BSA bovine serum albumin

G+ Gram-positive bacteria

G− Gram-negative bacteria

VBNC viable but non-culturable bacteria

CFU colony forming unit

λ_{max} wavelength of the peak maximum

PACVD plasma-assisted chemical vapor deposition

EDC N-(3-Dimethylaminopropyl)-N′-ethylcarbodiimide hydrochloride

PBS phosphate buffer saline

PFU plaque forming unit

APTES (3-aminopropyl)triethoxysilane

List of contents

Chapter 1

Theory and literature review

1.1 Electrodeposition

1.1.1 Historical and theoretical background

The dream of turning other metals into gold partially came true due to the revelation of plating. Since ancient times alchemists were looking for a way to cover different metals with other metals. The goal was achieved by means of simple reduction in solution. After the discovery of the electricity in 1789 this type of plating was supplemented with electroplating. To Luigi Brugnatelli we owe the first electrogilding. In 1805 he wrote to the Belgian Journal of Physics and Chemistry: *"I have lately gilt in a complete manner two large silver medals, by bringing them into communication by means of a steel wire, with a negative pole of a voltaic pile, and keeping them one after the other immersed in ammoniuret of gold newly made and well saturated*" [1] The first viable patent for silver and gold electroplating was secured in 1839 by Henry and George Elkington. [2] The term "electro-metallurgy", meaning the process of working in metals via electrolysis, was originated in 1841 by Alfred Smee. [3]

Nowadays, in use is the term "electrochemical deposition", which includes "electrodeposition" and "electroless deposition". The former is defined in the Electrochemical Dictionary [4] as *"the process of forming a film or a bulk material using an electrochemical process where electrons are supplied by an external power supply"*. The latter is the autocatalytic process where the reducing agent is the source of electrons.

In 1899 Caspari introduced the term “overpotential” [5] to describe the difference between the potential of the electrode through which an external current is flowing (*E(I)*) and the equilibrium potential of this electrode (*E*):

$$\eta = E(I) - E \qquad (1)$$

The overpotential is the potential required to overcome the hindrance of the overall electrode reaction – the activation energy. It is proportional to the electrochemical saturation - $\Delta\mu$ - which is the difference between the electrochemical potential of solution and of newly created crystal.

Six years later Tafel [6] showed the relationship between the overpotential and the current density:

$$\eta = a + b \log i \qquad (2)$$

Then it was already known that the electrodeposition of a metal on a substrate of the same metal occurs at the equilibrium potential. In the 1940’s it turned out that in many cases metal can be deposited on a foreign substrate at potentials more positive than the Nernst potential (the reduction potential of the deposited metal). This phenomenon is called underpotential deposition. [7, 8] It typically occurs only up to one or two monolayers of deposited material. Since the 1930’s a systematic development of the theory of electrochemistry and electrodeposition took place. Volmer and Erdey-Gruz derived the current-potential relationship for the reaction rate constant. [9] Moreover they introduced the 1st nucleation model for electrochemical crystal growth (*vide infra*). When Frank and Burton [10, 11] realized that the substrates surfaces have had imperfections, which can act as independent growth sites, a series of new growth models were developed.

1.1.2 Growth of deposits [2]

From a chemical point of view electrodeposition is a very complex process. One has to consider many aspects of physical chemistry, especially of surfaces, like kinetics, electrochemistry and/or crystallography. It is worth looking a bit closer into the mechanisms of nucleation and growth of deposits.

In general the theory states that metal electrodeposition starts at the electrode with the formation of individual growth centers *via* direct reduction of ions onto the electrode surface (see *Fig. 1*). It is common that surface defects become nucleation centers [12] because of their lower energy in comparison to the ideal surface. Such places attract hydrated metal ions from the electrical double layer to adsorb at the surface. Adsorbed ions (so-called adions) migrate to the places with the lowest energy and they create a cluster – a zero-dimensional nanostructure. Clusters can undergo aggregation, dissolution and/or Ostwald ripening (detaching of the surface atoms from the crystal and their condensation on the surface of a bigger crystal). When the cluster is built of a sufficient number of adions it becomes a nucleus. The critical radius of nucleus (meaning the minimum size that must be reached by atoms or molecules clustering together to form a stable aggregate) depends on the area occupied by one atom, therefore it is different for different materials.

The nucleation process can occur in two ways:

- instantaneously, when the nucleation constant is large and almost all the nuclei have possibility to grow on the surface are created at the same time,
- progressively, when the nucleation constant is low and the growth of nuclei is extended in time.

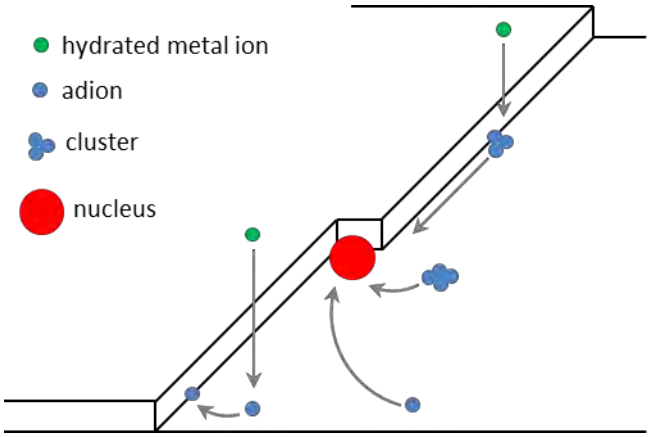

Fig. 1 The schematic representation of adsorption of hydrated ions at the surface and of migration of adions to create clusters and nuclei. Adapted from [2]

The form of the created nucleus (whether it's planar or three-dimensional) mainly depends on the molecular weight, nucleation rate constant and density of the deposit. The created nucleus should have the smallest energy possible. Moreover, the number of created nuclei is affected by the current density. [13] Deposits obtained at low current densities consist of a small number of nuclei. With increasing current density or overvoltage the number of growth centers increases and their sizes start to decrease.

Basically three growth models can be distinguished (chronologically):

- the "simple classical model" of Volmer and Weber (with further changes) [9, 14, 15]
- the model of Scharifker and Hills (with further changes) [16, 17]
- the electrochemical aggregative growth mechanism [18-20]

The oldest model, by Volmer and Weber [14] (continued by Volmer and Erdey-Gruz [9, 15]) assumes that the crystalline aggregates of the new phase have the same composition, structure and the thermodynamic properties as the bulk material. To correct this statement Milchev and Stoyanov [21] proposed the atom by atom growth of nanometric size clusters. But still it was presumed that all the nuclei grow independently of each other until the Scharifker and Hills publication [16]. They showed that when a constant

overpotential is applied nuclei are formed progressively on the surface and grow (presumably) by the direct attachment of adions. The growth of each of them affects the overpotential distribution over the electrode surface and reduces the concentration of active species in the vicinity of the nucleus, thus reducing the nucleation rate. Then, if one considers the multiple clusters case, the local zones of reduced nucleation rate spread and start to overlap (see *Fig. 2*). This is the reason why the new nuclei are expected to grow only at a given distance from each other.

Lately a new mechanism was proposed for growth of 3D particles focusing on the early stages of electrochemical formation of deposits. [18, 19] It revises the statement that the electrochemical growth is only driven by the direct attachment. The growth process, according to Ustarroz *et al.* [19], starts with the nucleation of primary nanoclusters. They can be either very small or "medium" sized because of occurring coalescence of two clusters which were formed very close to each other.

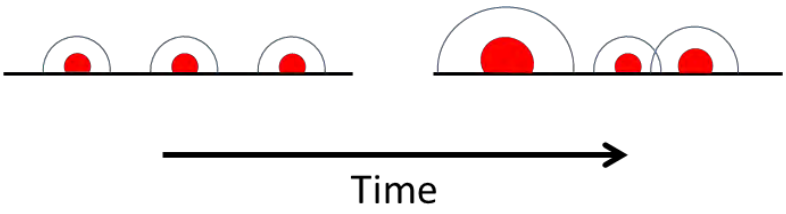

Fig. 2 A schematic representation of growth of nuclei (red) and, consequently, of the overlap of the local zones of reduced concentration of active species (blue semicircles).

The small clusters are formed until the nucleation zones start to overlap and cover the entire surface. To this time three parallel processes can be observed: the nucleation of new small clusters, surface movement of small clusters forming aggregates (situation like with moving adions) and direct attachment of metal ions to aggregates. The electrochemical potential driven surface diffusion of these primary nanoclusters is caused by their large surface to volume ratio and low degree of crystallinity hence by their instability. An

increase of the degree of crystallinity causes a decrease of the energy of the system, and is more favorable. Finally, the degree to which aggregates undergo partial or full coalescence dictates to which extent further growth by direct attachment (or classical island growth) occurs. This model was developed on the basis of transmission electron microscopy experiments. It was seen that the primary clusters of electrodeposited silver are monocrystalline but the aggregates are at first polycrystalline and later undergo recrystallization (what was also shown earlier in [22]). It is a very important finding because many properties of nanoparticles (e.g. electrocatalytic) depend on their crystalline structure. [23, 24]

In 2015 the group of Patrick Unwin showed that electrodeposition of metal nanoparticles does not require surface defects or atomic steps to occur. [25] The electrodeposition of silver on the basal plane of highly oriented pyrolytic graphite (HOPG) was tested. Using scanning electrochemical cell microscopy (SECCM) authors showed that nucleation occurred at the basal plane of HOPG. The created nucleus grew via aggregative mechanism. It was simultaneously moving along the surface and searching for the “anchoring point” (having the lowest energy thus allowing the creation of a bigger particle). The growth stops when the entropic gain of the free particle in bulk solution is greater than the interaction energy between this particle and the HOPG substrate. At this point the created particle is detaching from the surface. One can conclude that surface defects are crucial to the mechanical stability of the resulting electrodeposited material.

Besides layers and islands it is possible to form e.g. dendrites, powdered or spongy deposits. Dendrites are protrusions growing under charge-transfer control while electrodeposition of the rest of the cathode goes on under diffusion control. They display a highly oriented three-dimensional structure, growing and branching in well-defined directions. Formation of dendrites is favored by decrease of concentration of deposited ions, increase of the concentration of the supporting electrolyte or of the viscosity of the bath, decrease of the temperature and/or stirring. Most common are dendrites of Ag [26], Cu [27], Pb [28] (for others see [29]). Powdered deposits are formed from dendrites which spontaneously fall apart during growth or can be abrupted by mechanical action. This process is controlled by diffusion. The

morphology of the powder can be affected by electrolyte concentration, stirring, temperature, galvanostatic or potentiostatic deposition modes. Spongy deposits are structures with nanometric grains and filaments, obtained under conditions of low nucleation rate. The mechanism of their formation is not fully understood but it seems that the initiation of spongy growth is due to the amplification of surface protrusions within the spherical diffusion layer forming around each independently growing grain. Spongy deposits were reported e.g. for ZnO [30], Cu [31], Ag [32] and Au. [33]

1.2 Nanoparticulate deposit as a 3D nanostructure

A three-dimensional island of deposited material which size is below 100 nm is referred to as a *nanoparticle* (NP). One of the most important features of NPs is their high surface area per volume unit. As a result they possess considerable surface energy, what is one of the main causes of their different physical properties compared to the bulk materials.

Metal NPs are potentially useful for catalysis [34], electronics, environmental analysis and sensing [35], even in many biological and medical applications. [36]. That is why the design of novel synthesis protocols is of interest to researchers for almost two decades now.

In general NPs can be classified by their chemical composition, shape and properties. They can be produced by a vast range of procedures which can be grouped into top-down and bottom-up strategies (*Fig. 3*). The top-down approach mainly consists of physical methods which allow generating nanoscale assemblies directly from bulk materials. Typical examples are micromilling and photolitography followed by physical vapor deposition. The bottom-up methods start with molecular components which form more complex structures via chemical reactions, nucleation and growth processes. Different protocols allow producing NPs of different shapes such as spheres [37], rods [38], prisms [39], flowers [40] etc. The representative example

relevant for this thesis is electrochemical deposition. With top-down methods it is easier to control the shape of the final product, whereas the bottom-up methodology often gives more control over the chemical composition of the NPs.

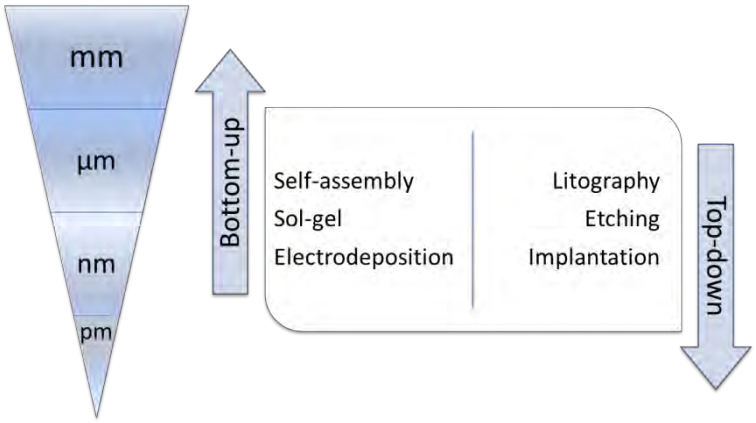

Fig. 3 A schematic differentiation between top-down and bottom-up methods of obtaining nanostructures.

1.2.1 Possible ways of electrodeposition of submicrostructures

Electrodeposition has become a very promising process used to synthesize the so-called supported nanoparticles because of the many advantages of the technique. These include possibility to tune up the properties of obtained structures *via* simple changes of electrolyte or deposition parameters. Moreover no need of further sample preparation is needed (e.g. no need of removal of photoresists like in photolitography). It is also cost-effective because the equipment used is relatively cheap and there is no need of work in ultra-clean environment. What is very interesting, electrodeposition is also used to precisely microfabricate surfaces to be used in the electronics and microsystems industries. [41, 42] In the literature many reports can be found about electrodeposition of different materials, e.g.:

- metals, such as Ag [26], Au [43], Ni [44], Co [45], Pd [46], Pt [47], and others [48];
- alloys (e.g. Cu-Pd [49], Sm-Co [50] etc.);
- composite materials [51] or
- oxides/chalcogenides. [52]

The process of electrodeposition needs proper conductive material which can be used as a working electrode. The most commonly reported substrates are: gold [53, 54], glassy carbon [55], highly oriented pyrolytic graphite [44], carbon nanotubes [56], indium- [57] or fluoride-doped tin oxide [58], etc. [59, 60] These can be pretreated e.g. with silica layer [61] or polypyrrole. [62] It is possible to deposit structures from aqueous solutions [63], from organic [48] or eutectic solvents [64] or from ionic liquids. [65] To obtain desired shapes researchers are using templates [66-68] or additives (e.g. surfactants [69], aminoacids [70] or polymers [71]).

It is possible to electrodeposit nanoparticles in two- [26, 72, 73] or three-electrode systems. In the latter arrangement one can find potentiostatic [74] or potentiodynamic methods [75] as well as chronoamperometric [76] (single [77] or double pulse method [78, 79]), chronoculometric [80], chronopotentiometric [81] methods, etc.

Given such a vast range of possibilities this thesis can not cover all of them. The review will be focused only on electrodeposition of gold and silver structures and will give a more detailed representation of some relevant cases.

1.3 Electrodeposition of silver and gold submicrostructures - state of the art

Control over the morphology of electrodeposited structures can be tuned in two main ways: physical or chemical.

The physical means include control over the stirring, temperature, pressure and all electrochemical parameters like potential or current density. Among the chemical factors one can mention the choice of the substrate and its pretreatment and the composition of the deposition bath. A careful selection of the precursor and the reducing agents is crucial for proper control over the nucleation and growth of the deposited structures. Moreover, it can determine whether the deposit will be strongly bound to the substrate surface or not.

1.3.1 Physical methods of control over the morphology

All the nucleation and growth models described in *Section 1.1.2* assume that the nucleation and growth are occurring under supersaturation conditions and the growth is only diffusion-controlled. Forced circulation (like stirring [82] or the use of a rotating disc electrode as substrate [83]) is needed when the electrodeposition process occurs e.g. with low concentrations of metal salts. The main reason is to avoid growth of dendritic structures.

Mostany *et al.* [84] showed that the changes of the reaction temperature induce changes in surface energies and in activation energies for nucleation. Ramirez *et al.* [85] established that with the increase of the temperature a smaller overpotential was needed to initiate the electrodeposition of Ag onto GC electrodes.

Morphology of the deposit differs with the change of used technique. In single-pulse potentiostatic methods only one value of the cathodic potential is set. The morphology of the deposit is tuned (physically) by changing the time of deposition or the pulse potential. The double-pulse method is characterized

with two pulses at different potentials E_1 and E_2, lasting for times t_1 and t_2 (usually $t_1 << t_2$), respectively (see *Fig. 4*). The first pulse is called the nucleation pulse. The nuclei are created only when E_1 is lower than the critical nucleation potential (E_{crit}). The second pulse is the growth pulse. The potential E_2 of this pulse is more positive than E_{crit} (so no further nucleation can occur) but is still below the reduction potential of the deposited metal allowing the nuclei to expand. [86] The morphology is tuned by varying the pulses potentials and/or their duration. Sandman *et al.* presented a systematic study of Ag electrodeposition on ITO by means of the double-pulse method. [87]

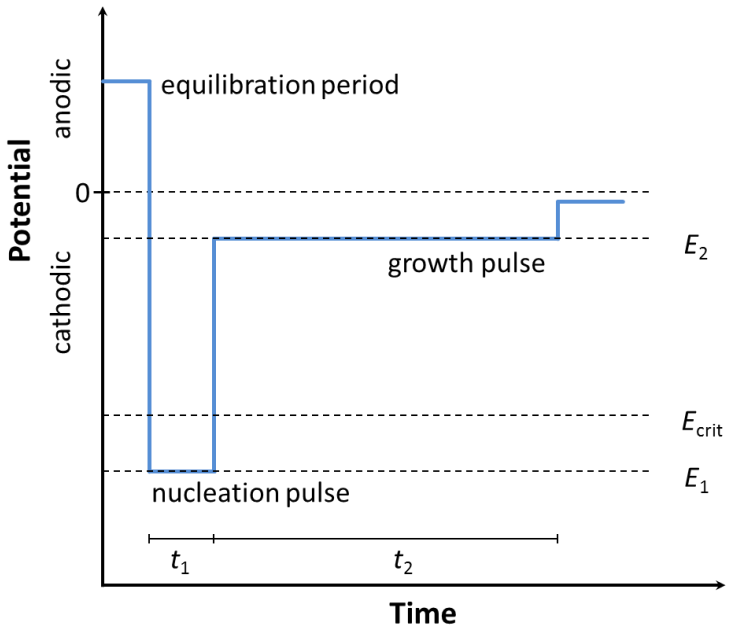

Fig. 4 Scheme of potential steps in the double-pulse method.

According to this research the more negative the nucleation potential and the longer the growth pulse the narrower size distribution of deposited particles will be. It can be seen that the number of created nuclei depends on the time of nucleation, t_1. This phenomenon is called progressive nucleation mechanism. It is opposite to the instantaneous nucleation mechanism where all the possible nuclei are created at the same time and are only growing over time. Moreover in the examined system the minimum nucleation time was determined to be

40 ms. The authors also showed that increasing the time t_2 leads to a decrease in the surface coverage. It is caused by destabilization and dissolution of particles smaller than the critical radius of the nucleus which lies in a growing region of reduced concentration of active species around growing nucleus.

Useful comparisons of the single- and double-pulse methods can be found in [88] and [89].

One of many successful uses of the chronoamperometric method was described by Li and Shi. [62] The authors showed the Au electrodeposition with control of the shape under constant current density conditions. The structure depended on the current density and the deposition time (adequate to the charge density). Increasing the time of deposition for low current density (0.125 mA cm^{-2}) changed the shape of the deposited structures from big, flower-like structures to a flat film. When high current density was used (1.2 mA cm^{-2}) the shape changed from small pinecones, through dense, rod-like structures to vertical nanosheets.

Ivanova and Zamborini [90] used a chronoculometric method to assure equal amount of gold electrodeposited on ITO under different potentials. They showed that the average AuNPs size increased with increasing deposition potential (see *Fig. 5*).

Potentiodynamic methods are mainly used to establish the reduction potential of metal in chosen baths. [87] Only a few groups, e.g. the group of Di or the group of Kerman, reported using cyclic voltammetry (CV) to electrodeposit gold nanoparticles on ITO. The plating bath presented by the group of Di contained potassium dicyanoaurate(I) and phosphate buffer solutions (pH 7.4 to 8). The potentials were measured vs. saturated calomel electrode (SCE) with Pt wire as counter electrode. CV was performed in different regimes in range from -0.2 V to -1.3 V (see *Fig. 6B*) for 20 cycles at 50 mV s^{-1}. The temperature of the reaction was 25˚C in [91] or 50˚C in [92-94]. A successful attempt was done to electrodeposit AuNPs from an environmentally friendly solution using CV. [95]

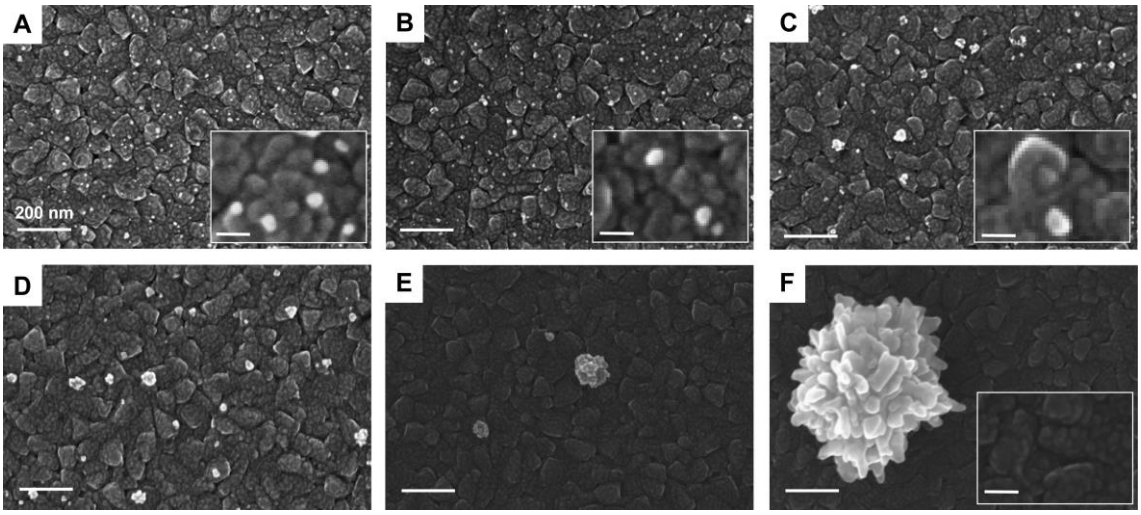

Fig. 5 SEM images of AuNPs deposited on ITO-covered glass at different potentials (vs. Ag|AgCl): (A) -0.2 V, (B) 0 V, (C) 0.2 V, (D) 0.4 V, (E) 0.6 V, (F) 0.8 V. The inset in F shows bare ITO-covered glass (scale bars represent 50 nm). Source: [90]

The bath contained chloroauric acid, potassium chlorate and phosphate buffer pH 2. The authors tested the influence of various numbers of deposition cycles, different potential ranges, various temperatures of the reaction and various concentrations of chloroauric acid. The effects were studied with UV-Vis spectrophotometry (see *Fig. 6*). Besides the aforementioned characteristics of deposits, Hu *et al.* do not show any relationship between the morphology and properties of the NPs and e.g. the potential scan rate or pH of the solution.

The group of Kerman showed in 2014 electrodeposition of AuNPs on ITO from baths containing solution of $HAuCl_4$ in phosphate buffer with varying concentrations of KCl. [96] They applied CV in a range of potentials -1 – 1.15 V vs. Ag|AgCl at potential scan rate of 0.1 V s^{-1} for 5 to 30 cycles. The as-deposited bumpy AuNPs were applied to detect DNA hybridization by means of localized surface plasmon resonance and electrochemical impedance spectroscopy.

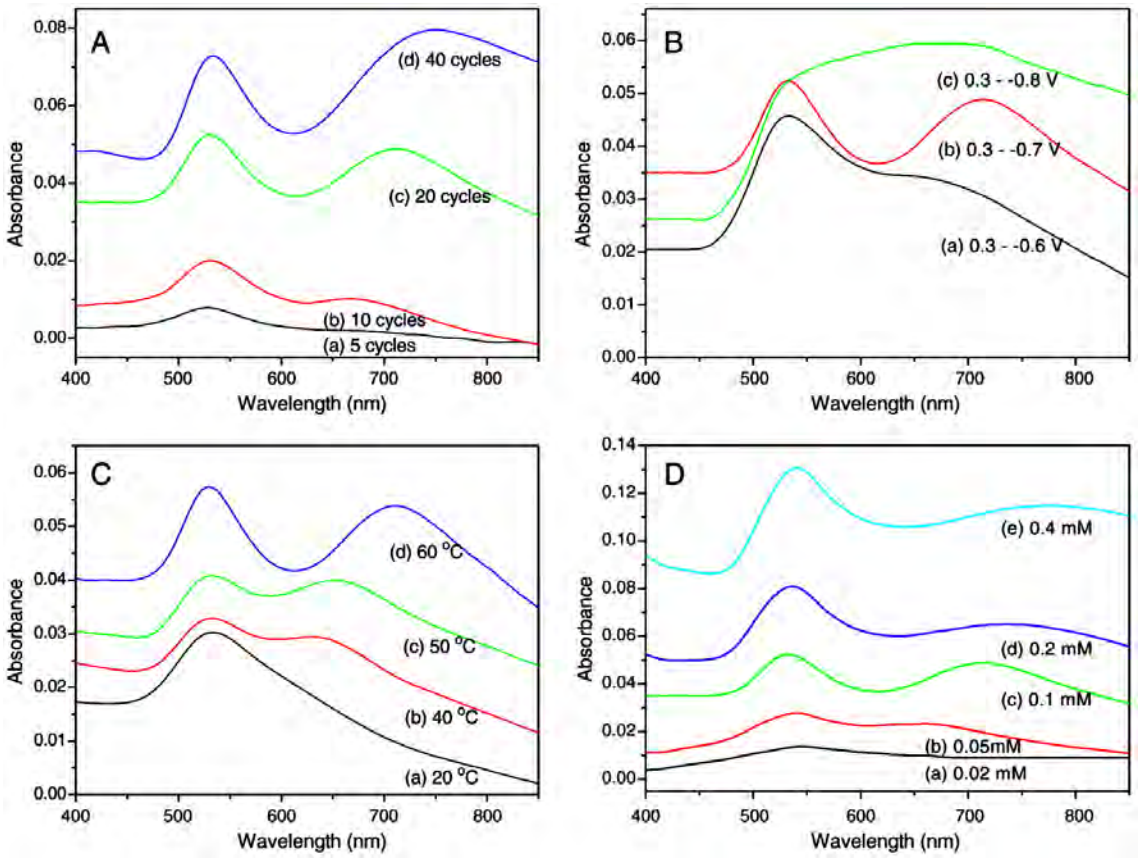

Fig. 6 UV-Vis spectra of AuNPs fabricated at various conditions in CV: (A) different number of cycles, (B) different potential ranges, (C) different temperatures, (D) different concentrations of chloroauric acid. Source: [95]

1.3.2 Chemical methods of the morphology control

There are three main ways to chemically influence the morphology of the deposit. The most basic one is proper selection of the substrate. Although Sakai *et al.* [97] and Gao *et al.* [70] showed that the deposits obtained at ITO electrodes as well as at glassy carbon (GC) electrodes under the same conditions are very similar, such reports are in a minority. The commonly accepted view is that the substrates morphology directly influences the morphology and crystallinity of the deposit. [98]

Another way is the pretreatment of the substrate, whether it is with the use of a template or an “interacting” layer. Templates make it possible to obtain structures of controlled size, shape and distances. Probably the most popular template is anodized aluminum oxide (AAO). [77] The AAO is an easy-to-produce array of nano-pores with high aspect ratios, assembled hexagonally. The material is deposited inside the pores and afterwards the template can be dissolved with no harm to the deposits. Other frequently used templates are silica microspheres [99], track etched polycarbonate membranes [66] or ionic-track membranes. [100] As “interacting” layers metals or polymers can be used. Hernandez-Santos *et al.* [101] showed a study of the influence of different metals deposited at carbon paste electrode on the morphology of subsequently deposited AgNPs. According to those results layers of Co, Pd, Pt or Cu accelerated the Ag deposition by changing the reduction potential of Ag to less negative values. Among the polymers used to cover the substrate can be mentioned e.g. poly(3,4-ethylenedioxythiophene) (PEDOT) or polypyrrole. As the EDOT polymerizes in a regular way, forming a well-oriented, spiderweb-like structure, it was reported to provide a uniform distribution of the electrodeposited Ag structures on a polymer-covered ITO surface. [80] Li *et al.* showed that Au nanoparticles electrodeposited at polypyrrole films tend to aggregate and form 3D structures. [62]

The last way to chemically influence the electrodeposition process and the obtained structures is the composition of the bath. Every bath contains ingredients which serve at least one of the following functions:

- to provide a source of the metal or metals being deposited;
- to form complexes with ions of the depositing metal;
- to provide conductivity;
- to stabilize the solution e.g. against hydrolysis;
- to act as a buffer to stabilize the pH;
- to modify or regulate the physical form of the deposit;
- to aid in dissolving the anodes (in case of the 2-electrodes system);
- to modify other properties, either of the solution or of the deposit, adequate to the specific case.

The two most fundamental components are the metal precursor (salt, acid or ionic liquid) and the solvent. According to Zheng *et al.* [76] a lack of supporting electrolyte is crucial to obtain silver nanowires (without using any template) and dendrites. The authors emphasize that nanowires were produced on HOPG electrodes from very diluted solutions (0.1 – 1 mM of aqueous $AgNO_3$). With increase of the Ag salt concentration the morphologies changed to dendritic. In classical electrochemical experiments a supporting electrolyte should be added to reduce the resistance of the solution. In this study the addition of 0.1 M KNO_3 resulted in the deposition of uniform grains. Other reports about electrodeposition without supporting electrolyte include the work of Gu *et al.* [72] and the work of Tang *et al.* [73] Both groups showed direct-current electrodeposition of Ag structures in 2-electrodes system from aqueous solutions of $AgNO_3$. In these cases it can be seen that the change of the morphology of deposits to dendritic was induced by the change of the electrodeposition potential (see *Fig. 7*).

The choice of the proper metal precursor gives control over the stability of the metal cation in the bath thus over the uniformity of the deposit. Some metals, like gold or silver, are not stable in hydrated form but their stability increases when they are complexed by a ligand. For example the cyanide ion, CN^-, is a common ligand forming complexes with both Ag and Au. For Ag ion complexed by other ligands the stability order is $AgBF_4 > AgClO_4 > AgNO_3$. [102] This is the primary reason of the popularity of the cyanide and perchlorate baths for electrodeposition of gold and silver structures (for references for using cyanides see e.g.: [78, 91, 93]; perchlorates applications, e.g.: [103, 104]). Unfortunately those compounds are toxic and need special treatment before waste can be disposed to the environment. [105] More environmentally friendly precursors, like $AgNO_3$ and $HAuCl_4$ are also often used [62, 77, 95, 106, 107] in most of the cases with citrate ions as ligands.

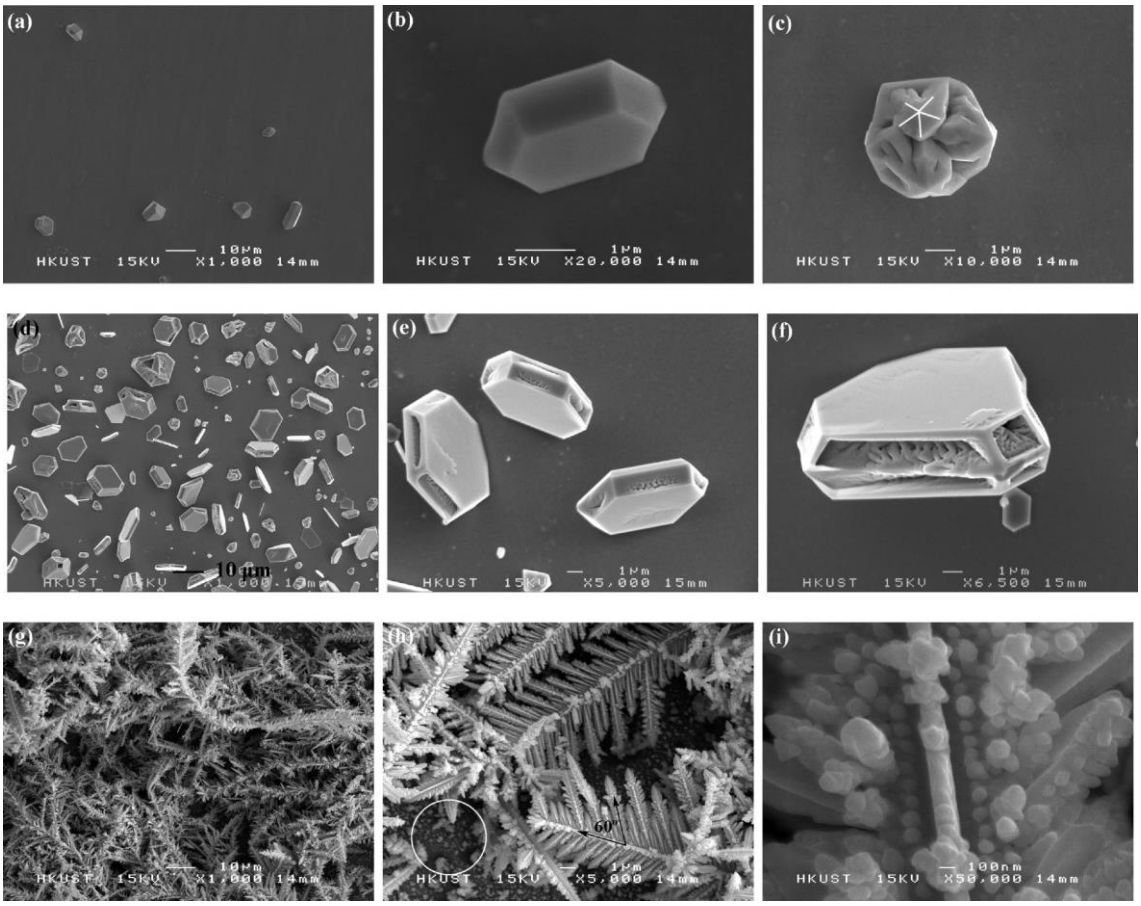

Fig. 7 SEM images with different magnifications of Ag crystallites prepared by the electrochemical process at different applied potentials for 30 min: (a-c) -0.4 V, (d-f) -1 V, and (g-i) -2 V. Decrease of the deposition potential caused change of the morphology of the deposits toward dendritic structures. Source: [72]

1.3.2.1 Citrate ion reduction method

The citrate ion reduction method was introduced by Turkevich in 1951 to produce colloidal gold. [108] It involved the reaction of small amounts of hot chloroauric acid with small amounts of sodium citrate solution. As a result 10-20 nm nearly spherical nanoparticles with good monodispersity were formed. This method is also suitable for production of silver nanoparticles however of larger size (60 – 200 nm) and of wide range of shapes. [109] The mechanism of metal reduction with citrate ions has been studied for a long time. Turkevich as the first postulated that before the gold nuclei will be

created the oxidation of citrate should take place. Species like dicarboxyacetone (one of the products of the citrate oxidation) act as multidentate ligands being crucial for production of clusters of Au(I) from Au(III). In the 1990's Chow and Zukoski demonstrated that in the initial phase of the reaction large gold aggregates are formed as a result of Au(III) reduction by citrates. During the course of the reaction those aggregates fall apart appearing as small monodisperse nanoparticles. [110] After careful electrochemical studies the group of Liz-Marzán postulated that the rate limiting step of the reaction is the reduction of Au(III) to Au(I). [111] It is important to highlight that the reactivity of both the citrate and auric species is pH-dependent. When the pH of the initial reaction mixture is high the AuNPs are formed slowly *via* the nucleation-growth pathway. Meanwhile at low pH the reaction rate is faster and the particles are created through the nucleation-aggregation-smoothing mechanism. [112] Basing on those and many other results Ojea-Jimenez and Campanera proposed mechanisms of the reduction of Au(III) by the oxidation of the citrate in mediums of various pH values. [113] The authors explain that the different reaction rates at different pH are caused by particular protonation state of the citric acid and the different number of OH^- ligands inserted into the Au(III) complex.

In response to the demand for environmentally-friendly approaches the citrate reduction method was adopted to electrodeposition. The as-obtained deposits are similar in their properties to those produced with cyanide baths – they are compact and homogeneous.

Zarkadas *et al.* [83] studied the influence of citric acid on silver electrodeposition from aqueous solutions. Their results are consistent with the aforementioned conclusions for bulk NP preparation – to tune the characteristics of the deposits one has to modify the concentrations of $AgNO_3$ and/or citrate ions and control the pH of the deposition bath.

Besides the control over the pH, to assure the defined properties of the deposits various compounds are added to the plating bath. Kaniyankandy *et al.* [26] reported that addition of ammonia to the plating bath drastically changed the Ag^+ reduction potential resulting in kinetic anisotropy of the electrodeposition process and thus in formation of dendritic structures. The tuning of the morphology (modifying the crystallite sizes and formation of branched nanodendrites) was done by change of the NH_3 concentration. To delay the dendritic growth e.g. boric acid can be used. [104] To reduce the grain size of deposits in aqueous solutions Gomez *et al.* [104] used sodium gluconate and El-Deab used iodide ions (they also increased homogeneity of the deposit) [98] whereas in ionic liquids Schaltin *et al.* [13] showed usefulness of thiourea and benzotriazole (see *Fig. 8*). There are reports about using citrate ions [76] or ethylenediaminetetraacetic acid (EDTA) [114] to obtain smoother coatings. To create the Au or Ag deposit with specific crystallographic structure one can use polyvinylpirrolidone (PVP). This polymer specifically binds to the <111> plane of crystal, blocking it and preventing ions deposition on it. [71] Another often used additive is L-cysteine. According to El-Deab *et al.* its effect depends on the type of the substrate used. For example on clean HOPG cysteine gives perfect spherical shape of AuNPs [98], on GC AuNPs grow along the <111> crystalline orientation while on ITO they are bumpy and rough. [97]

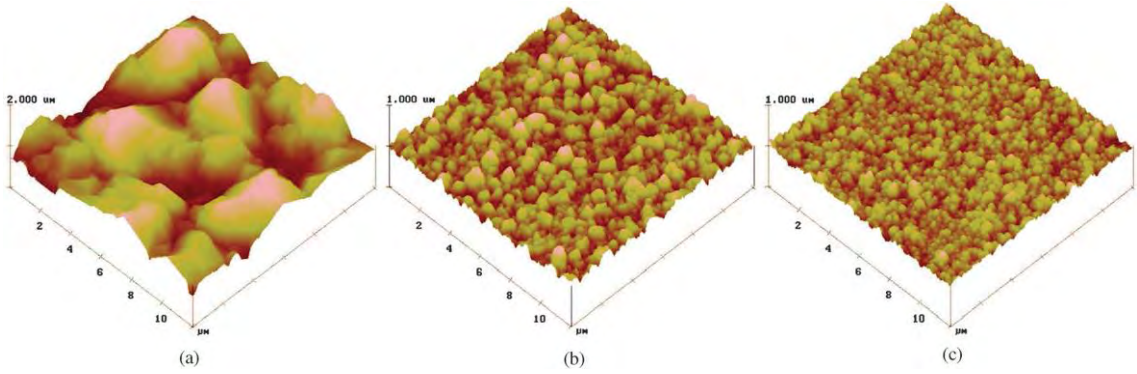

Fig. 8 AFM topologies of silver deposits obtained with (a) no additive, (b) thiourea, (c) 1H-benzotriazole. Source: [13]

Aside from the use of the classical two-phase system (substrate + bath) one can tune the properties of the deposit by changing the number of phases. A good example, shown by Kaminska *et al.* [115], was obtaining stripe-like deposits at the three-phase junction electrode | aqueous solution | ionic liquid. Another proposition was from Fu *et al.* [116] who electrodeposited AuNPs from a water-in-ionic liquid microemulsion. An alternative way is co-electrodeposition of bulk-prepared nanoparticles with silica sol-gel as made by Toledano and Mandler. [117]

1.4 Optical properties of metallic nanostructures

By controlling the material, size and shape of NPs it is possible to tune their optical properties – absorption, refraction and/or scattering of electromagnetic waves. [118]

It was already known in ancient times that addition of some metal salts to glass can give an astonishing effect. The perfect example is the Lycurgus Cup. It is a vessel probably made in Rome in the 4th century AD. [119] It was made of a dichroic glass, which shows a different color depending on the light reflection – when lit from behind the glass turns red and if lit from the front it turns green. Moreover, when various liquids fill the cup it can also change the color. The reason for this phenomenon is the presence of colloidal gold and silver nanoparticles of size ~70 nm [120] which enables the surface plasmon resonance effect.

According to the Drude model [4], introduced over a 110 years ago, metals are composed of mobile “free” electrons and the lattice of stationary cations. It is known that when the metal surface is irradiated with electromagnetic wave (light) of the appropriate frequency, those “free” electrons start to oscillate coherently. This oscillation of the conduction electrons is called a *plasmon* (because of its similarities to electronic plasma oscillations observed in gaseous discharges) and it can be described as fluctuations of the surface

electron density. [121] This is one of the effects resulting in colors seen by the human eye. The frequency of the oscillation is a characteristic feature of the metal. If it is slower than the frequency of incident visible light, the light is reflected and metal appears to shine. If it is faster than this frequency, the light is transmitted. If the electronic interband transition occurs in the visible range, specific light energies (colors) are absorbed and, as a result, it is possible to see characteristic color (e.g. blue for absorbed light wavelengths of 400-500 nm or red for 600-700 nm).

When we are considering the structure with small roughness, so a bulk metal or a thin film, plasmons can propagate along the surface (metal – dielectric interface) and evanescently decay perpendicular to the plane. This phenomenon is called the surface plasmon resonance (SPR). [122] However when we are looking into nanostructures with size less than the wavelength of incident light, the plasmon is localized directly on the surface of the NP and we are dealing with the localized surface plasmon resonance (LSPR). The difference is clearly seen when comparing the bulk gold, which is yellow, with gold nanoparticles which color ranges from red to blue. The color of a suspension of nanoparticles (or particles on a surface) is caused by adsorption of a very narrow range of light highly localized around a metal particle. The coherent oscillation of the electrons due to adsorption of the light with the proper frequency cause the local enhancement of the electromagnetic field near the particles surface. This enhancement is the greatest in places called hot spots – sharp tips of particles, inside gaps between particles (plasmon coupling) or between particles and a substrate (see *Fig. 9*). [122] What is very important, those field enhancements decay rapidly with distance from the nanoparticle surface. Moreover the particles` optical extinction displays a maximum at the plasmon resonance frequency (in the range of visible light for noble metal particles). A change of the AuNPs color from red to blue depending on their size is a direct evidence of the size dependence of the plasmon resonance frequency. [123]

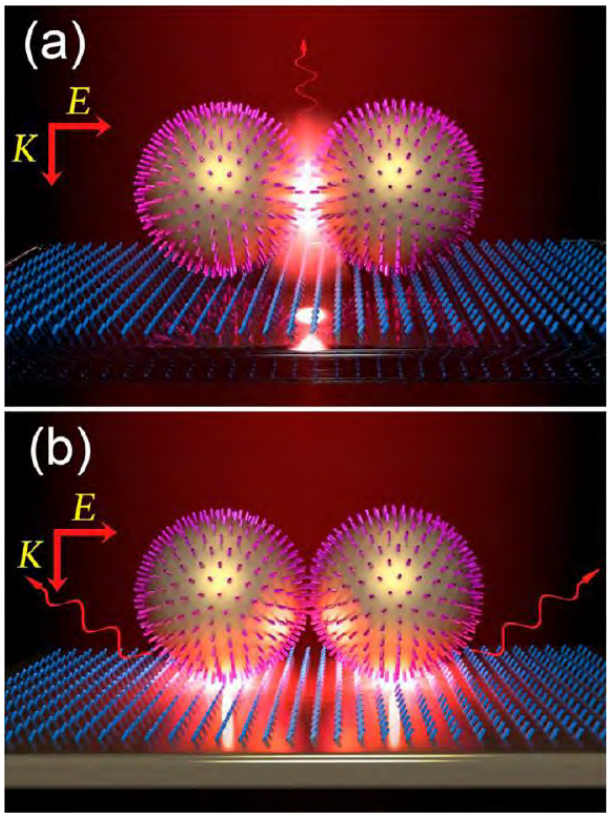

Fig. 9 Metal nanoparticles dispersed on a dielectric substrate. Creation of hot spots occurs in the gap between metal particles (a) or between particles and the substrate (b). Source: [124]

Typically the strongest plasmon resonances can be found in metals which are close to the Drude model. These are silver, gold, copper, platinum and aluminum with their relatively high conductivity and slight interband transitions in the visible region of the electromagnetic spectrum. Also alkali metals would be suitable if they would be easier to work with (e.g. work with Na needs water-free environment and work with Li needs oxygen-free environment). Furthermore, a great impact on the plasmon resonance has the local environment of the nanostructures – either the solvents refractive index or the adsorption of some species to the NPs surface. [118]

As a quantitative description of this phenomena the Mie theory is often used, which is an analytical solution of Maxwell's equations (for particles of spherical and cylindrical symmetry). [125] Considering a sphere with dimensions in the range of the wavelength of the incident light ($a \approx \lambda$), the

extinction* cross-section, $E(\lambda)$, of the sphere can be estimated by the following equation:

$$E(\lambda) = \frac{24\pi^2 a^3 \varepsilon_m^{3/2}}{\lambda \, ln(10)} \left[\frac{\varepsilon_i}{(\varepsilon_r + 2\varepsilon_m)^2 + \varepsilon_i^2} \right], \qquad (3)$$

where ε_m is the dielectric constant of the medium surrounding the sphere and ε_r and ε_i are the real and imaginary portions of the spheres dielectric function, respectively.

From this simple estimation, it can be seen that the extinction of a single sphere depends on its size (a), material (ε_r, ε_i), and the surrounding environment (ε_m). For non-spherical particles the cross-section also depends on the geometry, and then the substitution of $2\varepsilon_m$ with $\chi\varepsilon_m$ is needed, where χ contains information about the shape and aspect ratio of a particle of non-spherical geometry. Typically, to solve Maxwell's equations for those more complicated geometries in various dielectric environments, numerical methods are used. [126, 127] The important limitation of this theory is the assumption of noninteracting metal spheres.

For objects with sizes much lower than the wavelength of the incident light the Rayleigh scattering theory is used. Here the scattered intensity (σ_s) varies inversely as the fourth power of the wavelength according to the equation:

$$\sigma_s = \frac{2\pi^5 d^6}{3\lambda^4} \left(\frac{n^2 - 1}{n^2 + 2} \right)^2, \qquad (4)$$

where d is a diameter of scattering particle, n – its refractive index, λ - wavelength of unpolarized incident light.

* The scattering and absorption are jointly called extinction.

1.4.1 Applications of the Localized Surface Plasmon Resonance

The simplest use of LSPR is sensing the changes of the refractive index (RI) in the metal NPs environment. It is done by following the change in the resonance wavelength on UV-Vis spectrum. According to the Drude model the relation between the resonance wavelength shift and the refractive index is linear in small ranges of refractive indices. [128] The sensitivity towards changes in RI differs depending on the metal and shape of the used NPs (see *Table 1* below). [129]

Since the enhancements due to LSPR decay rapidly with distance from NPs surface, shifts of resonance wavelength caused by RI changes are sensed only in a direct vicinity to the NPs. Thus LSPR seems to be the perfect tool to observe short-distance molecular interactions. A model system used to study biomolecules interactions is the biotin-streptavidin couple. [130, 131] Streptavidin is a tetrameric protein which creates with biotin molecules one of the strongest non-covalent interactions known in nature. As shown by Haes and Van Duyne, exposure of biotin-functionalized Ag-nanotriangles to a 100 nM solution of streptavidin caused 27 nm shift of the resonance wavelength. The system had a limit of detection in the range of 1 pM. [132]

Another possible way of sensing using LSPR was shown in 2012 by Park *et al.* The resonance wavelength changed upon addition of sulfides to Au-core@Ag-shell nanocubes where S^{2-} ions reacted with Ag creating a stable Ag_2S shell (see *Fig. 10*). This system could detect sulfides in water with limit of detection of 10 ppm. [133]

Table 1 Refractive index sensitivities obtained for different Au and Ag nanostructures. Source: [129]

Nanostructure	Size (nm)	λ_{max} (nm)	Sensitivity (nm RIU^{-1})
Au nanospheres	13, 15, 30, 50	520	76, 44, 71, 60
Au nanorings	75 – 150	1058 – 1545	880
Au nanocubes	44	538	83
Au nanobypiramids	27 – 189	645 – 1096	150 – 540
Au nanostars	100	647, 700, 783	879
Ag nanospheres	40 – 90	400 – 480	160
Ag nanoprism	55 – 120	600 – 700	200 – 350
Ag nanocubes	30	430	1569

Other example of using colloids in LSPR detection was shown by Lesniewski *et al.* [134] In their setup AuNPs were functionalized with specific antibodies to selectively detect T7 bacteriophages. Due to the interaction of many antibodies with single bacteriophage the aggregation of AuNPs occurred. The result was a change of color of the solution from red to purple visible with the naked eye.

A different example of taking advantage of the plasmon resonance is the photothermal effect. When the plasmon resonance is triggered with the laser radiation of a specific wavelength a photothermal conversion occurs (exchange of the photon energy into heat energy). This phenomenon allows for very rapid, localized heating with high selectivity. It can be used instead of lithography or etching to create conductive lines and nanostructures like periodic holes or gratings. [135]

The sensitivity of plasmon coupling to the distance between nanostructures was used to develop a so-called plasmonic molecular ruler (PMR). [136] The group of El-Sayed showed that the interparticle plasmon coupling strength decays nearly exponentially with a decay length (for polarization of incident light along interparticle axis). Thanks to that PMRs can be used to measure the

size of biomolecules in a label-free manner and to measure realtime molecular conformation changes and binding events in a distance up to ~70 nm. [137]

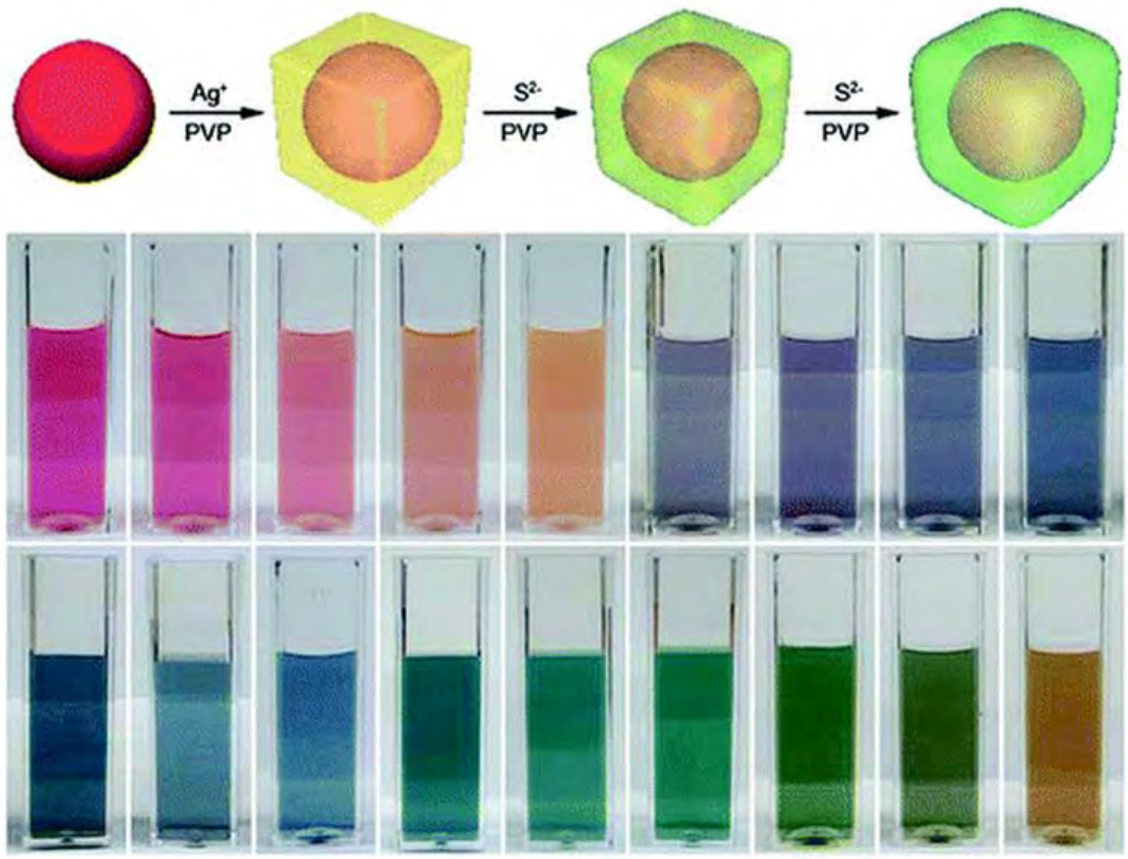

Fig. 10 Sulfide sensing system described by Park *et al.* Top panel – synthesis of Au-core@Ag/Ag2S-shell nanocubes; bottom panel – photographs of aqueous dispersions of synthesized nanocubes upon addition of increasing amount of S^{2-} ions. Source: graphical abstract of [133]

Localized surface plasmon resonance is also used in many spectroscopic techniques to enhance the signal. For example, when the molecule adsorbed on the nanoparticle has an absorption band overlapped with the LSPR, resonant energy transfer occurs between the metal and the molecule. In consequence plasmonic resonance energy transfer (PRET) is observed. It can be applied to detect metal ions [138] or bioimaging of molecules inside the living cells. [139] Plasmonic enhanced fluorescence (PEF) acts on the same basis – the absorption

and scattering spectra of the metal NPs should overlap with the absorption and emission spectra of fluorophore adsorbed on the NPs. Such sensors were successfully used e.g. to imaging prion proteins in living cells. [137] Moreover the same energy transfer between metal and adsorbed molecule has a contribution in surface-enhanced Raman spectroscopy.

1.4.2 Surface enhanced Raman spectroscopy

The Raman effect occurs when the incident light is scattered inelastically due to the interaction between the wave and the dispersing molecule. The change of energy of the scattered photon can be positive or negative (see *Fig. 11*). When the photon loses its energy it is called Stokes scattering. When it gains energy it is called anti-Stokes scattering. [122]

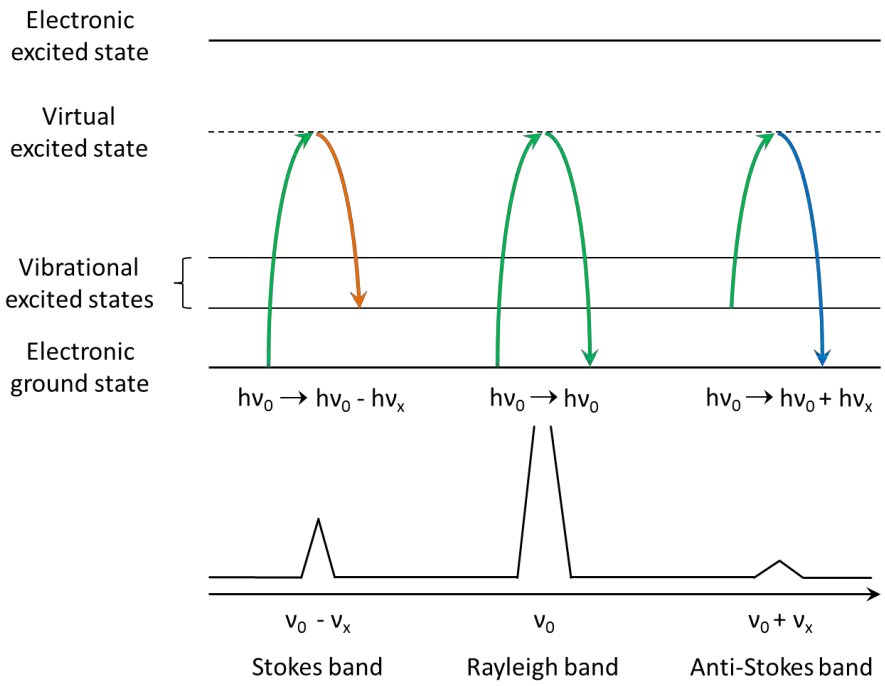

Fig. 11 Schematic representation of three types of light scattering for small particles and molecules: Stokes, when photon loses energy, Rayleigh, when the energy of the photon stays unchanged and anti-Stokes, when the energy of the photon increases.

Raman spectroscopy gives information about the rotational and vibrational structure of the examined substance. It is very specific for every compound that changes its polarity due to the excitation and thus Raman spectra are called the spectroscopic “fingerprint”.

As only one photon per million [129] is scattered inelastically one can call the Raman spectroscopy inefficient. In response several improvements have been introduced. The simplest method to enhance the signal is to illuminate the sample with the light which frequency is close to an electronic transition of the examined molecule. Using so-called Resonance Raman Spectroscopy (RRS), one can obtain an increase of the signal of up to 6 orders of magnitude. [140] Even greater improvement can be achieved with Surface Enhanced Raman Spectroscopy (SERS), where, thanks to the plasmon resonances of metal nanoparticulate substrate, it is possible to obtain even 14 orders of magnitude stronger signal. [141, 142]

In the 1970’s Fleischmann, Hendra and McQuillan were studying pyridine with Raman spectroscopy. The molecule was adsorbed on the electrochemically roughened silver. The obtained Raman signals were surprisingly strong and depended on the potential of silver roughening. [143] In 1977 two mechanisms of the enhancement of observed Raman signals were proposed: electromagnetic by Jeanmaire and Van Duyne [144] and chemical by Albrecht and Creighton. [145] The electromagnetic enhancement originates from the amplified local electromagnetic field (E) in plasmonic nanostructures. [146] The chemical enhancement is derived from charge transfer between plasmonic nanostructure and adsorbed molecule of interest. [137]

Thanks to the development of nanotechnology in 1997 it was possible to study single molecules with SERS. [147] The main difference between metallic substrates used for “normal” SERS and SERS of single molecules is the homogeneity of obtained enhancements within the substrate – for single molecules it is important to have very high local enhancements while for “normal” SERS whole substrate should give enhancement in the same order of magnitude. In general, efficient SERS substrate should have a developed surface (to assure large amount of adsorbed molecules) and work with suitable laser wavelength (to be as close as possible to the plasmons resonance region).

Moreover it should be non-toxic, disposable, mechanically and chemically stable. Thus the most common substrates are made with silver (for the lasers of wavelength below 600 nm) and gold (for the lasers of wavelength longer than 600 nm).

To evaluate the level of enhancement the enhancement factor (EF) was introduced. [148] It corresponds to the proportion of signals obtained in SERS and Raman experiments (with the same power and wavelength of the laser). In the literature there can be found three types of EF:

– analytical enhancement factor (AEF) is perfect for describing SERS in metal colloids, because it connects the enhancement with the concentration of the analyte;

$$AEF = \frac{I_{SERS}/c_{SERS}}{I_{RS}/c_{RS}}, \qquad (5)$$

where I_{SERS} and I_{RS} are intensities of the signal obtained in SERS and Raman experiments, respectively, c_{SERS} and c_{RS} are the concentrations of analyte used in SERS and Raman experiments respectively;

– SERS substrate enhancement factor (SSEF) takes into account only molecules adsorbed directly on the surface and it is considered the most adequate evaluation of substrates;

$$SSEF = \frac{I_{SERS}/N_{Surf}}{I_{RS}/N_{Vol}}, \qquad (6)$$

where I_{SERS} and I_{RS} are intensities of the signal obtained in SERS and Raman experiments, respectively, $N_{Vol} = c_{RS}V$ is the average number of particles in the scattering volume V during the Raman experiment while the N_{Surf} is the number of molecules adsorbed on the surface in the SERS experiment;

– single-molecule enhancement factor (SMEF) describes local enhancements and takes into account orientation of the molecule on the surface and orientation of the surface relative to the polarization of the

light, thus is used more often in theoretical than experimental calculations; it is the ratio between the intensity of the signal for a single molecule in SERS experiment and average intensity of the signal from Raman experiment recalculated for one molecule:

$$SMEF = \frac{I_{SERS}^{SM}}{\langle I_{RS}^{SM} \rangle} \qquad (7)$$

Moreover, if the experiment is conducted with the laser wavelength in the range of the resonance of the probe molecule and the probe molecules self-assemble to the monolayer than the equation for the EF looks as follows:

$$EF = \frac{I_{SERRS} c_{RRS}}{I_{RRS} c_{SERRS}}. \qquad (8)$$

1.4.3 Electrodeposited Ag- and Au-based platforms used in LSPR and SERS

As was stated before, electrodeposition protocols allow tuning the morphology of deposits. This possibility was exploited by many authors to obtain nanoparticles with tailored optical properties. Suitability of developed platforms to LSPR is most frequently presented with the example of response to different refractive indices of solvents [77, 95, 149-153]. Deng *et al.* (from the group of Di) showed a strategy to improve the refractive index sensitivity of electrodeposited AuNPs by covering them with a thin film of Ag. [152] Spherical AuNPs were obtained by CV in acidic phosphate buffer solution of $HAuCl_4$ (60 cycles at potential scan rate of 50 mV s^{-1} in a potential range 0.3 – -0.5 V *vs.* SCE). The Ag film was deposited from 20 mM aqueous solution of $AgNO_3$ in a potential range 0.3 – 0 V at potential scan rate of 50 mV s^{-1}. The thickness of the Ag film was tuned by changing the number of scans in the CV. Along with the change of the shell thickness, the RIS value changed. The group obtained a 76% improvement of RIS (compared to bare AuNPs electrodeposited on ITO) with applying an Ag shell of 0.7 nm (20 scans of CV) resulting in a RIS of 127 nm RIU^{-1}. This system was also used to study biotin-streptavidin interactions. The Au-core@Ag-shell structure was functionalized with biotin

and the shift of the resonance wavelength upon addition of streptavidin was recorded. A linear response was obtained in the range 10^{-10} – 10^{-6} M of streptavidin showing the effectiveness of such systems in the detection of molecular interactions. The biotin-streptavidin model was also used by e.g. Hu *et al.* [95]

Electrodeposited Ag-Au alloys were also suitable to detect mercury ions in aqueous solution in the range 0.05 – 500 ppb. [154] To obtain NPs Di's group applied CV in a potential range 0 - -0.9 V vs. SCE at a potential scan rate of 50 mV s^{-1} for 30 cycles resulting in spherical particles. The resonance wavelength of the obtained NPs was tuned by changing the Ag:Au ratio. During the detection of mercury ions the resonance wavelength shift was caused by reduction of Hg^{2+} ions by Ag atoms from Ag-AuNPs and creation of amalgamate on the surface of the NPs.

LSPR on electrodeposited bumpy AuNPs was also shown for DNA hybridization to detect specific gene mutations. [96] Other studied specific interactions include, among others, antigen-antibody interactions (performed on twin-linked AuNPs) [155] or lectin-carbohydrates interactions (performed on nanostructured gold film). [153] Apart from the works of Dang *et al.* [152] and Tao *et al.* [154], where silver is only a part of the used system, there are only few reports about using Ag-based electrodeposited sensors in LSPR. [77, 156, 157] The majority of the works were done on Au-based platforms, probably due to the higher stability of AuNPs.

In case of SERS the use of platforms prepared by means of electrochemistry is historically justified since the first SERS spectrum was recorded on electrochemically roughened silver electrode. [143] Nowadays to show the usefulness of electrodeposited platforms in SERS many different dyes are used, like rhodamine (B [73] or 6G [78, 79, 158]), crystal violet [159] or brilliant cresyl blue. [80] Other SERS probes reported are, among others, mercaptobenzoic acid (MBA) [75] and 4-aminothiophenol. [160, 161] SERS is used to study and/or detect important molecules like adenine on Ag nanoflowers [79, 161], formaldehyde on Au nanodendrites [162], methyl

viologen (a herbicide) on electrochemically roughened electrodes [160] or neurotransmitters on spherical AgNPs. [57] Moreover SERS can be used to investigate the electrodeposition process like shown by Bozzini *et al.* for electrodeposition of Ag-Au alloys. [163] One can also find reports on systematic investigation of the electrodeposition process on the SERS efficiency, e.g. by Du *et al.* about the enhancement dependences on diameter and aspect of Ag-nanowires fabricated with AAO templates [164] or by Tang and Meng showing the dependence of SERS activities on the morphology of obtained nanoflowers (see *Fig. 12*). [73] Electrodeposited platforms were also useful in single molecule SERS of 4-merctaptopyridine [165] or porphycene. [166]

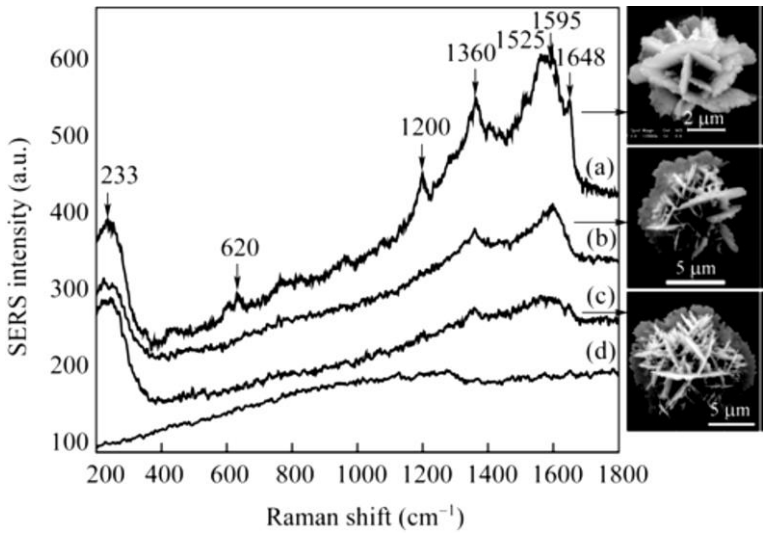

Fig. 12 SERS spectra probed with 10^{-6} M Rhodamine B adsorbed on the respective flowerlike silver particles shown on the right. Source: [73]

1.5 Conclusions and goal of the work

Electrodeposition allows the growth of particles of defined size, shape and properties in a very precise and cheap manner. With the development of the research techniques it is possible to better understand and take advantage of all the processes comprising the electrodeposition phenomenon – from the metal ion complexation to the nucleation and growth of the supported nanostructures - gaining tailored properties of as-prepared deposits.

There are two basic ways to tune the features of the obtained structures: physical (control of the temperature or electrochemical protocol) and chemical (proper choice of the substrate or the solutions composition). The current work is focused on using environmentally-friendly reducing agents replacing cyanides and perchlorates. One of the most promising candidates are citrate ions, which so far have been only used in combination with potentiostatic protocols.

The literature review showed that using potentiostatic electrodeposition procedures it is possible to produce NPs with a limited size distribution, but the obtained coverage densities are not satisfactory. Thus potentiodynamic methods were chosen, specifically cyclic voltammetry. Such approach grants the possibility of tuning the number of nucleation and growth steps (with the number of cycles used) as well as the relaxation time of the system (with changing the scan rate). This time is needed for the metal ions to diffuse from the bulk of the solution to the reaction zone near the working electrode. Moreover the use of the citrate ligand was preferred because of its harmlessness and lack of reports about usage in potentiodynamic methods.

It was shown in the literature that electrodeposited platforms are used in both LSPR and SERS studies. The majority of those experiments were performed on Au-based platforms. Only few reports described using Ag- or Au-based platforms made by means of cyclic voltammetry (e.g. Au-based LSPR sensor described by Hu *et al.* [95]).

The aim of this work was to obtain platforms built of ITO electrodes and properly distributed monodisperse NPs of gold and silver resulting in high and narrow peak in the UV-Vis spectrum (which should result in high refractive index sensitivity) and/or SERS enhancement factor above 10^5 for 4-ATP as a model probe molecule. Moreover all experiments should be performed in agreement with the principles of "green chemistry" – using environmentally-friendly reagents and causing low energy consumption.

Chapter 2

Methods and materials

2.1 Methods

2.1.1 Voltammetry

Voltammetry is a group of electrochemical techniques where the change in the current flowing through the working electrode is observed while its polarization is varied in time. The polarization of the working electrode is tuned linearly. In a typical experiment using linear sweep voltammetry (formally called linear potential sweep chronoamperometry) the potential of the working electrode is changed from E_1 to E_2 (see *Fig. 13A*). When the potential reaches E_s – the value specific for reduction/oxidation of the tested compound – the electrochemical reaction begins and the current starts to flow. The current value grows until the concentration of the reduced/oxidized substance near the working electrode surface drops almost to zero (diffusion-limited process). Then the current starts to decrease what is depicted as a peak shape at the current-potential curve (see *Fig. 13B*). If the polarization is reversed after reaching E_2 it is possible to inverse the electrochemical process to oxidize or reduce the compound near the surface of the working electrode. In such case the used technique is called the cyclic voltammetry (CV). If the electrochemical reaction is reversible it is possible to perform an infinite number of cycles. If the reaction is not reversible at some point there will be no more substance to reduce/oxidize.

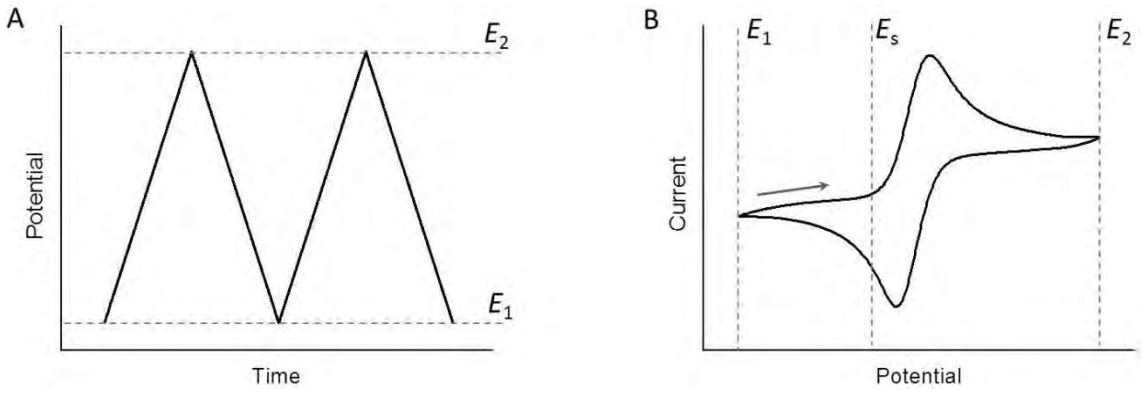

Fig. 13 A schematic representation of potential changes in time (A) and resulting changes of current (B) in cyclic voltammetry. The arrow shows the direction of the scan.

The setup needed for the voltammetric experiments is, in most of the cases, a three electrode system consisting of working, reference and counter electrodes. At the surface of the working electrode the electrochemical process under investigation takes place. The reference electrode is the internal standard to measure and control the potential of the working electrode. Through the counter electrode passes all the current needed to compensate the current observed at the working electrode.

All the CV experiments described in this dissertation were conducted in a three-electrode system (see *Fig. 14*) with ITO as a working electrode. During silver electrodeposition a platinum mesh was used as a counter electrode and an Ag wire as a pseudo-reference electrode. For electrodeposition of gold stainless steel vial was used as a counter electrode and Ag|AgCl wire as a pseudo-reference electrode. Wires were used instead of a classical Ag|AgCl|3 M KCl reference electrode to avoid accumulation of NPs at the porous diaphragm. The surface of the ITO was masked with a scotch tape to assure the repeatable area to be deposited on (20 mm^2).

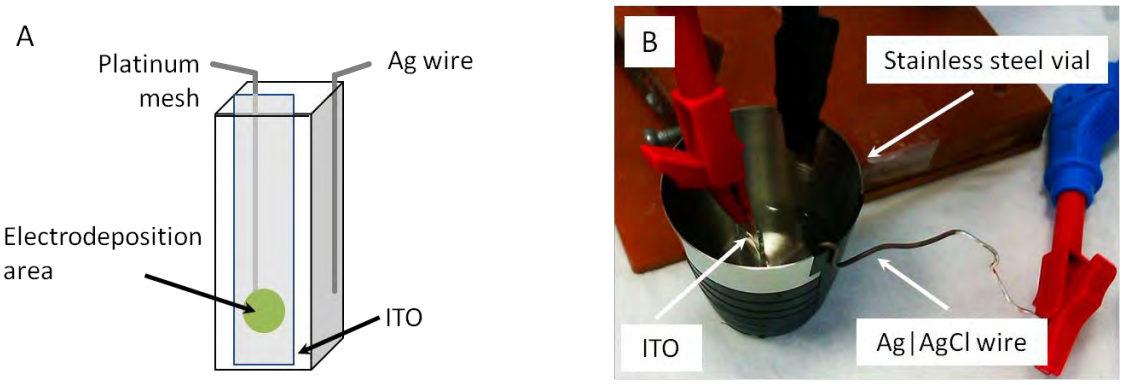

Fig. 14 A - A scheme of the setup used for electrodeposition of silver submicrostructures; B – A photo of setup used for electrodeposition of gold submicrostructures.

2.1.2 UV-Vis spectroscopy

Every matter interacts with the electromagnetic field – light can be absorbed, transmitted and/or scattered. In the visible and ultraviolet range absorption occurs when the energy of a single incident photon is equal to the gap between the ground and an excited state of an electron at the valence shell. By absorption of photon the atom gains energy and goes to the excited state. In the process of relaxation the excess of energy can be emitted in form of a photon having equal or smaller energy than the exciting one.

According to the Lambert-Beer law the intensity of the incident light decreases after passing through the sample. The resulting intensity depends linearly on the thickness and the concentration of the sample of interest and on its scattering properties. In some cases this law is not fulfilled, e.g. when the incident light is not collimated and monochromatic or when there is an interaction between substance and solvent, e.g. dissociation or solvation (different energies of solvation of excited states results in shifting of absorption maxima in the spectrum). [167]

A UV-Vis spectrophotometer is used to study the localized surface plasmon resonance and the refractive index sensitivity of nanostructures of interest. There are two basic systems used in spectrophotometers. The first one consists of the light source (usually deuterium or xenon lamp), a tunable monochromator, a place for sample and a detector (usually a photomultiplier tube). Such a system measures each wavelength separately but it stands out with low noise and high sensitivity. Second possibility is to illuminate the sample with broadband light and split it to separate wavelengths just before measurement on an array detector. The main advantage of this arrangement is almost instantaneous acquisition of the spectrum. Both systems can be used as single- or dual-beam. In single-beam setup the reference sample is measured before the sample of interest. In the dual-beam setup the measurement is simultaneous for both, reference and examined samples.

During experiments an Evolution 300 spectrophotometer from Thermo Scientific was used. It is a double-beam, monochromator-based system operating in the 190 – 1100 nm range of light. It has xenon lamp as a source of light and a silicon photodiode as a detector.

2.1.3 Scanning electron microscopy [168]

Scanning Electron Microscopy (SEM) is a well-known and very popular imaging technique. It is suitable for observation of heterogeneous organic and inorganic materials in a scale of μm to nm in 3D-like images. SEM allows for imaging of samples topography, crystallinity and composition.

The general scheme of work for the SEM microscope is always the same (see *Fig. 15*). An electron beam is created and accelerated by an electron gun and directed by a set of electromagnetic lenses. As a result a spot of approximately 10 nm diameter is created. The energy of the electron beam can be tuned in the range of *ca* 0.1 – 30 keV. The beam is moved by the deflection coils line by

line to create a raster image. As the beam interacts with the sample a multitude of signals are generated at the same time.

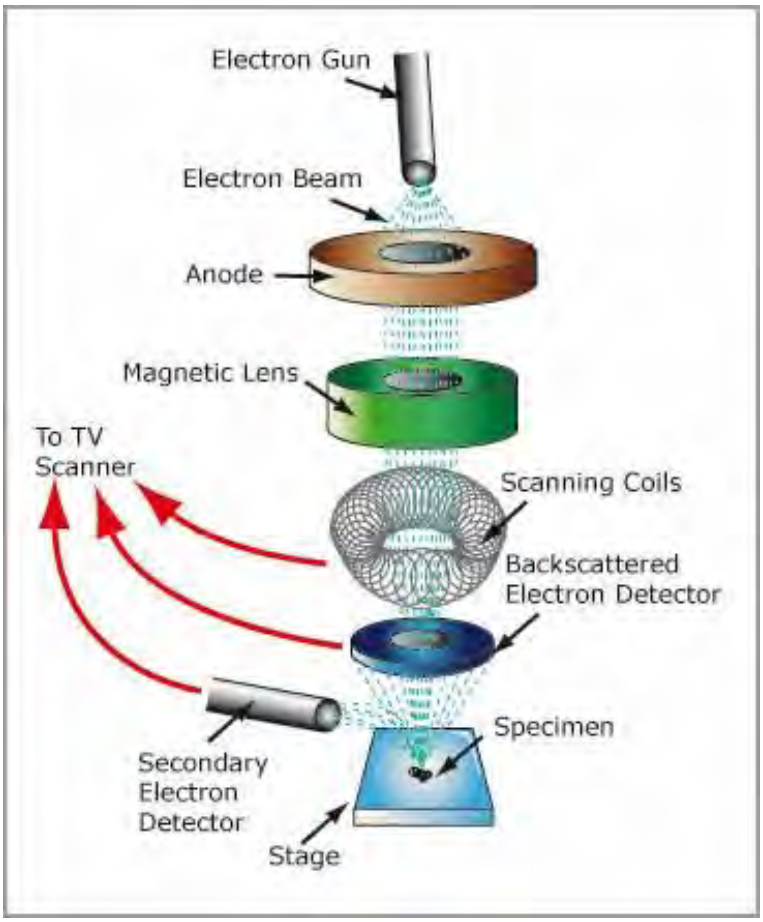

Fig. 15 A scheme of a scanning electron microscope (source: [169])

The interaction volume depends on the beam energy and of composition of the sample. The order of magnitude of its size is 10 nm in diameter and several μm of depth. From this volume backscattered electrons (BSE), secondary electrons (SE) and characteristic X-rays (among other) come. BSE and SE are the most often used types of signals used to create a SEM image – to show the topography, composition, crystal orientation, *etc.* Also frequently used to reveal the compositional features are the characteristic X-rays created by the Auger process. All those signals are collected by various detectors and converted into an image by the computer equipment.

In this work two scanning electron microscopes were used – Zeiss Supra and FEI Nova NanoSEM 450.

2.1.4 Surface enhanced Raman spectroscopy

When an electromagnetic wave (laser) interacts with a molecule an electric dipole moment can be induced. The created dipole oscillates along with incident wave causing periodical deformation of the molecules. The deformation is greater the bigger the polarizability (tendency of charge distribution to be distorted by an external electric field) of the molecule of interest is. Because of periodical deformation, the molecule starts to vibrate with characteristic frequency. In consequence this oscillating dipole can emit light of three different frequencies (see *Fig. 11* in *Section 1.4.2*): unchanged (Rayleigh scattering), increased by ν_x, where $h\nu_x$ is the energy of the molecular vibration, (anti-Stokes scattering) or diminished by ν_x (Stokes scattering). The Rayleigh scattering is predominant since only about one photon per million is scattered inelastically (with change of its frequency). Thus to obtain high-quality Raman spectrum it is necessary to filter scattered photons and exclude those having frequency of the incident light. It can be done using notch filters or spectrophotometers. The last part is detection performed using photodiode arrays (PDAs) or charge-coupled devices (CCDs).

In the surface enhanced Raman spectroscopy the enhancement of the signal is a result of the interaction between the molecule and, usually, the rough surface of a noble metal. There are two proposed mechanisms of enhancement: electromagnetic and chemical. In the first one the increase of the induced dipole moment in molecules of the analyte is caused by locally enhanced electromagnetic field (hot spots, see *Section 1.4*). In the latter one it is believed that molecules of analyte increase their polarizability due to charge-transfer effect and possible creation of chemical bonds between the molecule and the used substrate. Both, normal Raman and SERS experiment can be performed with the same setups.

In described experiments Renishaw inVia Raman system was used. It was equipped with a 632.8 nm HeNe laser and a 300 mW diode laser emitting at 785 nm. The light from the laser was passed through a line filter, and focused on a sample mounted on an X–Y–Z translation stage with a 20× microscope objective. The beam diameter for this objective was approximately 5 μm. The Raman scattered light was collected by the same objective through a holographic notch filter to block out Rayleigh scattering. A 1800 groove mm^{-1} grating was used to provide a spectral resolution of 5 cm^{-1}. The Raman scattering signal was recorded by a 1024 × 256 pixel RenCam CCD detector.

2.2 Materials

Hydrogen tetrachloroaurate (III) hydrate was purchased in ABCR.

Silver nitrate, potassium nitrate, trisodium citrate dehydrate and lactose were purchased in POCh.

L+ascorbic acid was purchased from Riedel-deHaën; formic acid, oxalic acid, α-D-glucose, α-D-mannose, 4-aminethiophenol (4-ATP), poly(vinyl pirrolidone), M_w~55000, epinephrine, dopamine, choline, acetylcholine, bovine serum albumin (BSA), *Lens culinaris* lectin and *Maackia amurensis* lectin were purchased from Sigma-Aldrich.

Ethanol, isopropanol, sulfuric acid and potassium iodide were from Chempur.

All reagents were used as received without further purification.

ITO coated glass (resistivity 8–12 Ω/square) was from Delta Technologies.

Water was purified with an ELIX system (Millipore).

2.3 Protocols

2.3.1 Electrodeposition procedure

The ITO electrodes were cleaned in an ultrasonic bath with ethanol (15 minutes) and deionised water (15 minutes). Next, the ITO electrode surfaces were dried with a stream of N_2 and defined by masking with scotch tape. The electrodeposition of metal nanoparticles was performed in a classical three-electrode system (described in details in *Section 2.1.1*). The electrodes were immersed into a deaerated aqueous solution of metal salt and reducing agent. Electrochemical protocol was executed with an Autolab (Metrohm Autolab) electrochemical system with GPES software. The exact parameters are described in adequate sections (*Chapter 3* and *4*). As prepared electrodes were rinsed with deionised water and dried under a stream of nitrogen.

All potentials are given *vs.* Ag wire (for silver electrodeposition experiments) or *vs.* Ag|AgCl wire (for gold electrodeposition experiments).

2.3.2 Evaluation of fabricated samples

The process was optimized towards the best plasmonic properties and the highest reproducibility. All protocols are described below. All the calculations were done in Origin 8 (Origin Lab, US) software.

2.3.2.1 Scanning electron microscopy

In order to record scanning electron micrographs (SEM images) samples were dried and mounted to SEM table with a conductive silver paste. The coverage density and size of electrodeposited structures were measured from recorded images using ImageJ software (NIH, US). Each measurement was done for five different pictures of the same sample.

2.3.2.2 UV-Vis spectroscopy

UV-Vis experiments were performed in polymethyl methacrylate (PMMA) cuvettes (optical path of 1 cm). Spectrophotometer operated in an absorbance mode with bandwidth of 2 nm. In order to establish the absorbance peak positions (λ_{max}) spectra were fitted with Lorenz function using Origin 8 (Origin Lab, US) software.

Refractive index sensitivity (RIS) tests were performed measuring the UV-Vis spectra of the sample (randomly chosen from the batch) in at least four solvents from the list below: air (n = 1), water (n = 1.332), ethanol (n = 1.362), isopropanol (n = 1.377), 86% glycerol (n = 1.452). λ_{max} was shown in function of refractive index, n, and fitted with linear function. The slope of the linear fit corresponds to RIS.

Spectra shown in the next sections are chosen, representative examples.

2.3.2.3 Surface enhanced Raman spectroscopy

In order to evaluate the enhancement ability of the produced submicrostructures the SERS experiments with 4-aminothiophenol (4-ATP) were conducted. Produced substrates (surface area of 20 mm^2) were immersed into 9 mL of 10^{-6} M 4-ATP ethanol solution for overnight adsorption. Then they were washed gently and dried under stream of nitrogen. The SERS measurements were taken with 632.8 nm laser (power = 5 mW), integration time for a single spot was 10 s. Every measurement was done for five separate samples. Every sample was tested in five different points. Spectra shown in the next sections are chosen, representative examples.

A reference Raman measurement was recorded with the same laser wavelength but the power and the integration time were increased to 60 mW and 60 s, respectively.

The surface enhancement factor was calculated according to the formula:

$$EF = \frac{I_{SERRS} c_{RRS}}{I_{RRS} c_{SERRS}}, \qquad (9)$$

where N_{SERS} and N_{RS} refer to the number of molecules adsorbed on the SERS probe within the laser spot area and the number of molecules probed by regular Raman spectroscopy, respectively. I_{SERS} and I_{RS} correspond to the SERS intensity of 4-ATP onto surface and to the normal Raman scattering intensity of 4-ATP in the bulk. I_{RS} and I_{SERS} were measured for the band at 1078 cm^{-1}. The crucial parameters for the quantitative analysis of the spectra are the laser spot area and the effective illuminated volume. The latter has been estimated using a formula recommended by Renishaw:

$$V = 3.21 \times \lambda^3 \left(\frac{f}{D}\right), \qquad (10)$$

where f is the microscope objective focal length and D is the effective laser beam diameter at the objective back aperture. For our setup the illuminated volume was $V \approx 2 \times 10^3$ µm^3. The laser beam diameter, defined as twice the radius of a circle encompassing the area with 86% of the total power, was about 5 µm.

The normal Raman spectrum was obtained for a cell filled with a pure 4-ATP (125.19 g mol^{-1}) of density 1.17 g cm^{-3}. Under these conditions, $N_{RS} = 11.3 \times 10^{12}$ molecules were irradiated by the laser. The crucial stage of this experiment is to ensure a less-than-a-monolayer coverage, otherwise the EF is overestimated. Assuming that the surface of our samples was 20 mm^2 and that one molecule of 4-ATP covers 42×10^{-8} µm^2, the number of deposited molecules should not exceed 5×10^{13}. This is a very rough estimation. In reality, the available surface is much larger because of the substrate roughness. The number of 4-ATP molecules for the illuminated surface of 19.6 µm^2 was estimated as $N_{SERS} = 5.3 \times 10^6$. On a basis of this data the EF for obtained substrates were calculated.

Chapter 3

Electrodeposition of silver submicrostructures

The inspiration for this work came from the paper of Zhang and Oyama [170] where the authors used a two-step procedure to attach gold nanoparticles (AuNPs) to the ITO surface. The procedure consisted of the seeding and growth steps and had no use of any electrochemical process. At the first stage the ITO substrate was immersed in a solution containing AuNPs seeds of 4 nm. They were prepared from $HAuCl_4$, trisodium citrate, and $NaBH_4$ as a reducing agent in an aqueous solution. After 2 hours the substrate was moved to the aqueous growth solution – $HAuCl_4$ (metal precursor), cetyltrimethylammonium bromide (CTAB, stabilizing agent), NaOH (pH regulator) and ascorbic acid (reducing agent) – and left for 24 hours. This method gave spherical and rod-shaped nanoparticles covering about 20% of the surface of ITO as can be seen on *Fig 16*. The seeding step is based on the physical adsorption of the AuNPs to the ITO surface. There was almost no control over the density of the resulting seeds. In addition, the growth step was very long and the solution included the surfactant CTAB.

The proposed improvement of this method comprised using electrochemistry to seed and grow the AuNPs. Also the weak reducing agent – ascorbic acid (which is unable to reduce gold salt without seeds [69]) was replaced with a stronger one – trisodium citrate. Because the citrate ions act both as reducing and capping agent, it was possible to eliminate the presence of CTAB. Moreover, citrate ions are suitable to reduce both silver and gold salts. [109]

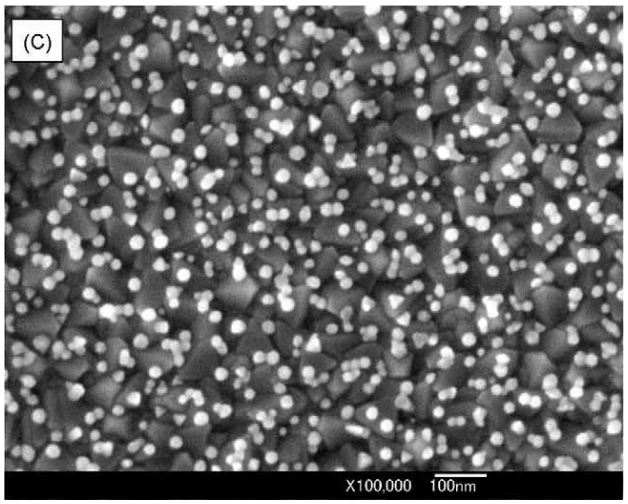

Fig. 16 SEM image of AuNPs deposited on ITO by Zhang and Oyama (source: [170])

The electrochemical method of choice was cyclic voltammetry. The most important feature of this method is that one scanning cycle is equivalent to one seeding-growing event. By changing the number of cycles of the deposition it is possible to control the number of seeding-growing events. Additional advantages are:

- possible tuning of the time of deposition by changing the potential scan rate
- control over the time of diffusion of metal ions from the bulk to the surface of the working electrode by elongating the potential range.

The substrate of choice was glass covered with indium-tin oxide (ITO). This electrode has a broad potential window where it is stable. It is chemically resistant and transparent to the light in near-UV and visible region. Moreover, the microscopic structure of the ITO surface has a high roughness factor. It assures a lot of possible nucleation sites.

In this part of the dissertation it will be shown how the morphology of the submicrostructures is influenced by the factors listed below:

- potential range,
- potential scan rate,
- number of scans,
- concentration of the reducing agent,
- type of reducing agent,
- concentration of the metal precursor,
- stirring.

To evaluate the obtained substrates the scanning electron microscopy, UV-Vis spectroscopy and/or surface enhanced Raman spectroscopy were used. Preferred platforms should exhibit uniform distribution of microstructures. Moreover, the platforms should reveal a single, well-developed absorption peak in the UV-Vis range (exhibiting the full width at half maximum, FWHM < 70 nm) with good refractive index sensitivity (RIS > 100 nm RIU^{-1}) and/or SERS enhancement factor above 10^5 for 4-ATP as a probe molecule.

3.1 Reduction with citrate ions

3.1.1 Optimalization of electrodeposition conditions

The initial electrodeposition bath contained equimolar (0.25 mM) aqueous solution of $AgNO_3$ and trisodium citrate and was deoxygenated with N_2 for 15 minutes. The reaction proceeded without a supporting electrolyte to reduce the number of used compounds to minimum (to obtain as clean NPs as possible). The composition of the bath was as follows: 1.15×10^{-6} mole (115 µL of 10 mM solution) of $AgNO_3$ and 1.15×10^{-6} mole (115 µL of 10 mM solution) of trisodium citrate in total volume of 4.5 mL of deionized water.

In the first step the best range of potentials for cyclic voltammetry was estimated. The size and shape of obtained particles as well as the surface coverage were taken as preliminary evaluation factors. In *Fig. 17* a typical CV from the extended scan range is shown with two reduction peaks: the Ag-deposition peak at -0.1 V and a peak at -0.7 V originating from reduction of oxygen residues from the solution. Peaks at potentials above 0 V come from oxidation of deposited silver.

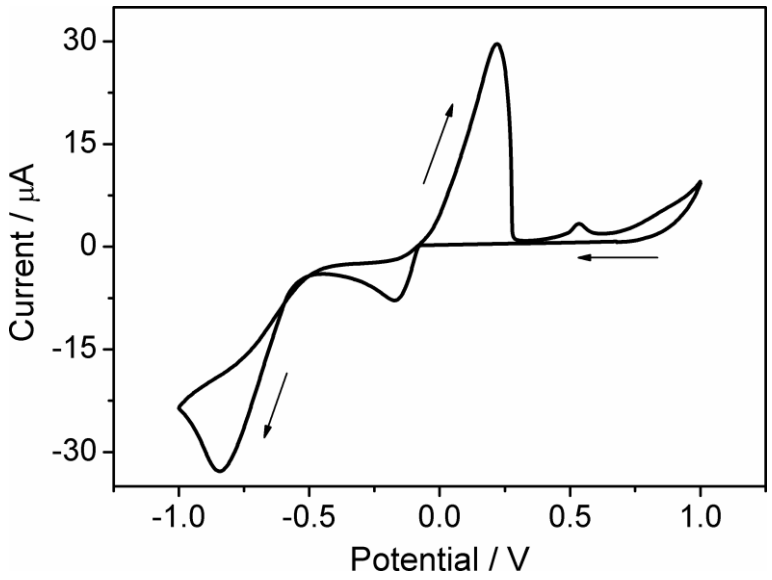

Fig. 17 Cyclic voltammetry in broad potential range; 0.25 mM of $AgNO_3$ and 0.25 mM of trisodium citrate in total volume of 4.5 mL of deionized water; potential scan rate: 10 mV s^{-1}. Arrows indicate the direction of the scan.

In *Fig. 18* the differences between structures obtained from equimolar aqueous solution of $AgNO_3$ and sodium citrate in different ranges of potentials (0 – -0.4 V, 0 – -0.8 V and 0 – -1 V) are presented. Every scan starts from 0 V and is directed towards more negative potential. If the scan direction is reversed at potential a little lower than the reduction of silver (-0.4 V) a dense cover of particles is formed on the electrode. However, the size and morphology of the particles are very diverse, from small crystallites to large star-shaped structures. When the scan range was extended to -0.8 V a uniform

and dense coverage was achieved. In the range 0 – -1 V, dendritic structures appeared.

For further experiments the potential range 0 – -0.8 V was chosen.

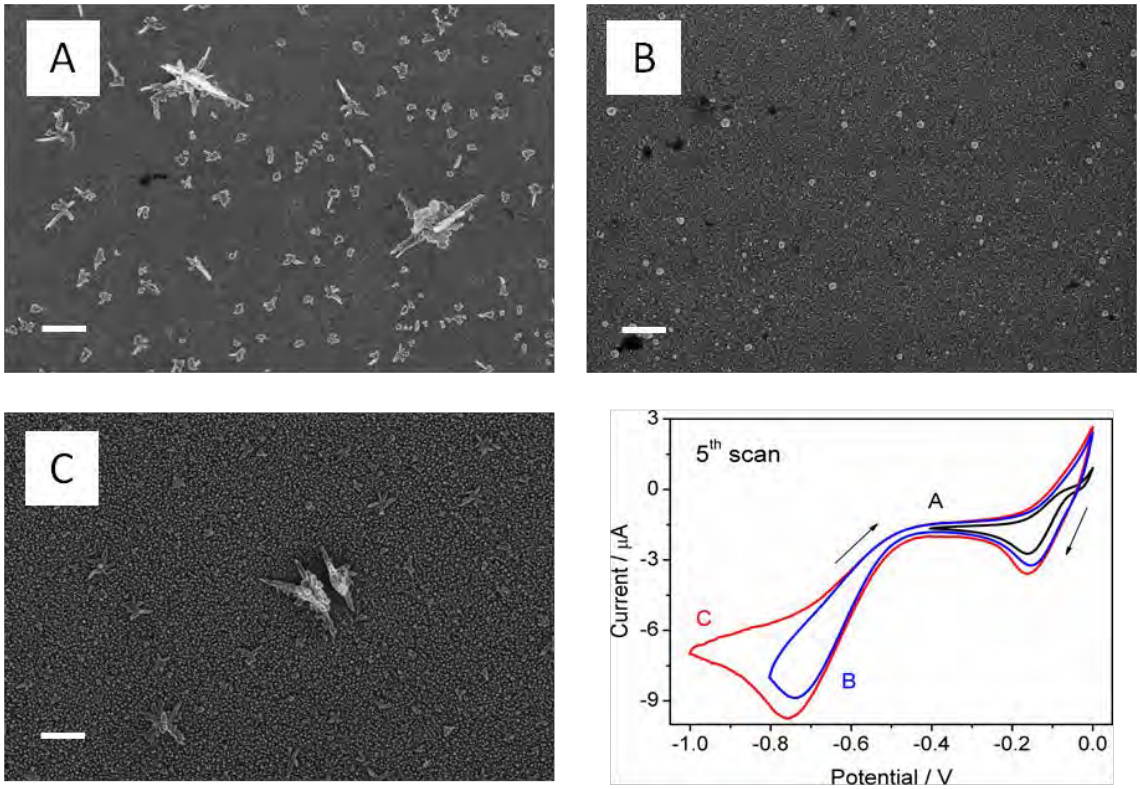

Fig. 18 SEM images (scale bar: 1 µm) of AgNPs structures obtained after 5 scans of electrodeposition at 10 mV s^{-1} in range of potentials: (A) 0 – -0.4 V, (B) 0 – -0.8 V and (C) 0 – -1 V; along with voltammograms showing the 5th scan of the electrodeposition of respective structures.

To be sure that the peak at -0.7 V comes from an oxygen reduction process, experiments with oxygenated (15 min) and deoxygenated (with nitrogen, for 15 min) solutions were performed (see *Fig. 19*). As expected the peak current magnitude was sixteen times higher for oxygenated than for deoxygenated solution.

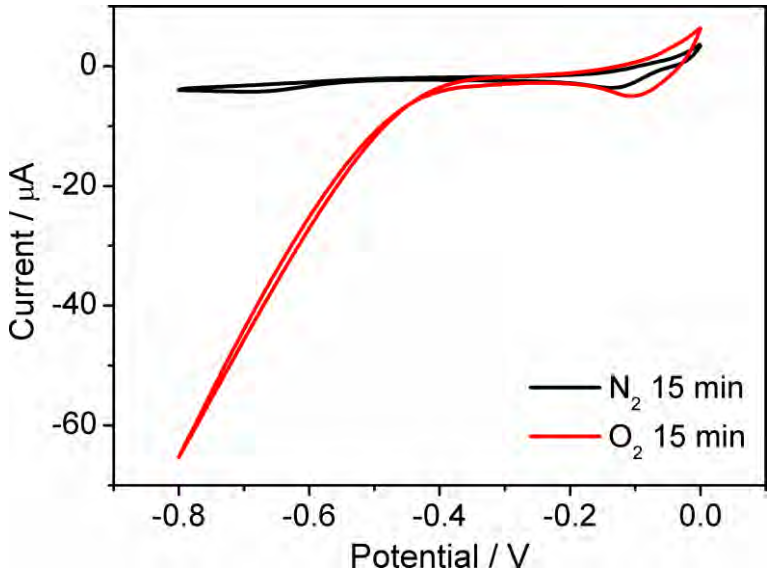

Fig. 19 Voltammograms showing the 5th scan of electrodeposition from oxygenated (red curve) and deoxygenated (black curve) solution (potential scan rate: 10 mV s^{-1}).

Next step was to check how the number of scans and the scan rate affect the structure and properties of deposits. The set of experiments for 5, 10, 20, 35 and 50 scans with the potential scan rate of 5, 10, 50 or 100 mV s^{-1} were performed. Because of a very long time of 50 scans at 5 mV s^{-1} this experiment was skipped. Exemplary voltammograms together with SEM pictures are shown in *Fig. 20* (differences resulting from the scan rate) and in *Fig. 21* (differences resulting from the number of scans). One can easily note the influence of the scan rate on the particles size. The average radius decreases together with increasing scan rate and is in the range between about 45 – 60 nm at 5 mV s^{-1}, 35 – 50 nm at 10 mV s^{-1}, 20 – 50 nm at 50 mV s^{-1} and 20 – 35 nm at 100 mV s^{-1}. When the scan rate is increased to 100 mV s^{-1}, the particle deposit is quite sparse – about 10 – 15% density of the surface coverage, while for 5 mV s^{-1} it is about 20 – 40% (see *Fig. 20 E* and *B*, respectively). The most probable cause is that faster potential scan rate induces new seeding events in a short period of time and growing events are very short. The slower potential scan rate, the longer time a growing particle has to grow.

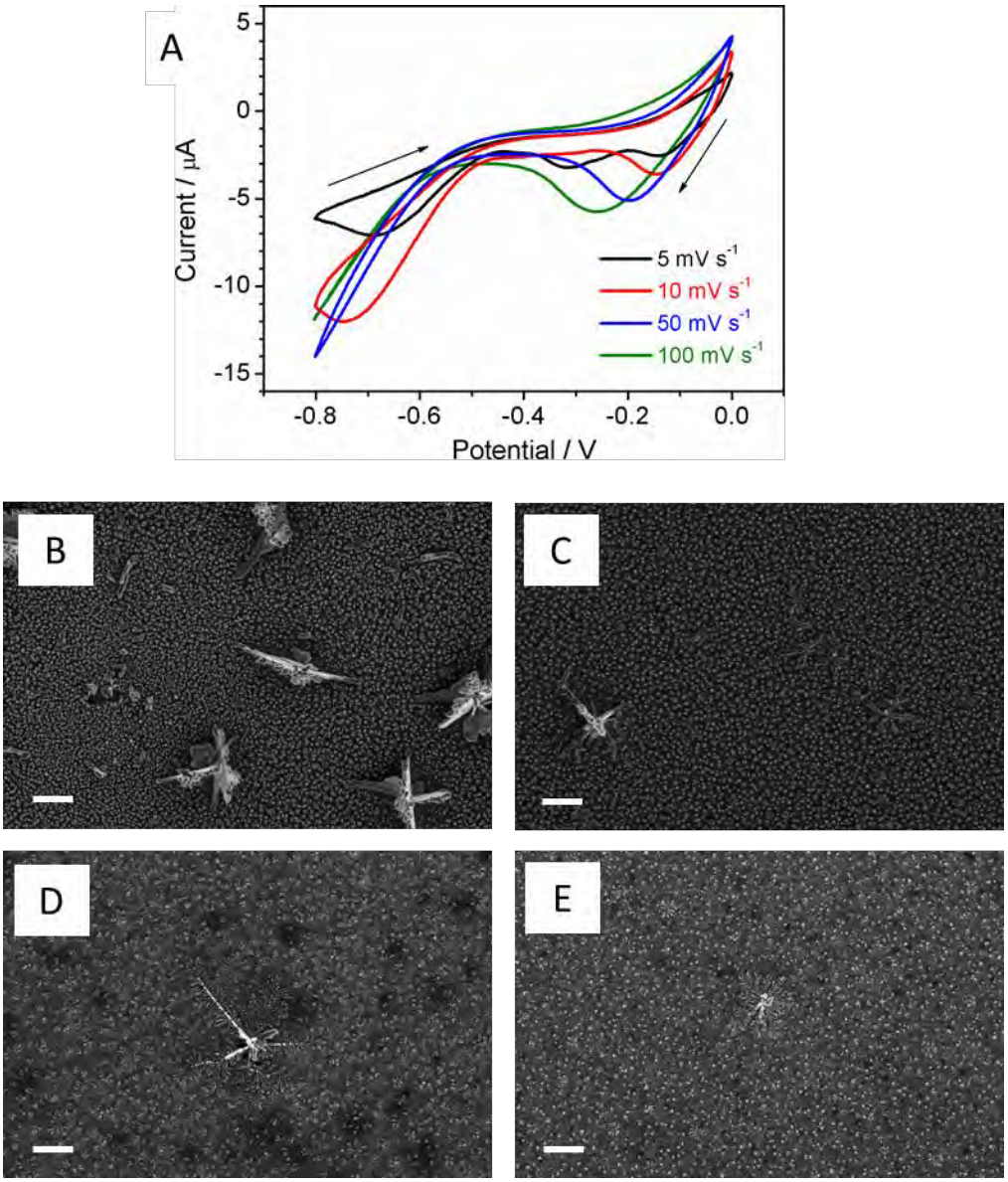

Fig. 20 Voltammograms of 10th scans obtained at different scan rates (A) together with SEM images of resulting Ag structures obtained at 5 mV s^{-1} (B), 10 mV s^{-1} (C), 50 mV s^{-1} (D) and 100 mV s^{-1} (E). Scale bar is 1 µm.

Increase of the number of applied scans causes simultaneous increase of both, particles' sizes and surface coverage densities. Also magnitude of current at -0.8 V increases with increase of the number of applied scans. This suggests that the surface of created structures is more developed thus more oxygen can be reduced. 35 scans results in formation of big dendritic structures (*Fig. 21D*). As can be seen in *Fig. 21E* application of 50 scans results in surface with

smaller number of dendritic structures than obtained for lower number of scans. It can be caused by spontaneous falling apart of dendrites parts during growth. [2]

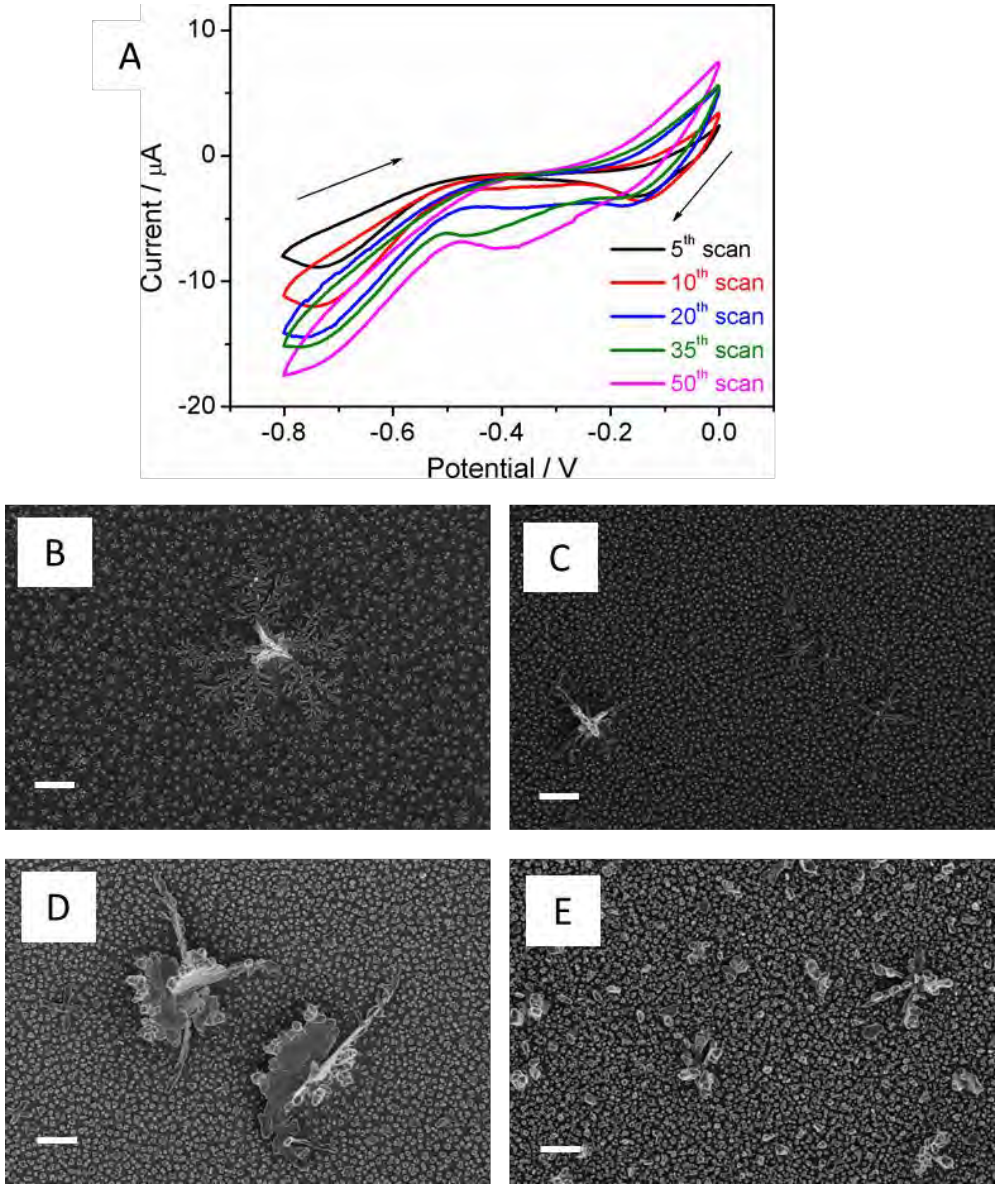

Fig. 21 Voltammograms obtained at 10 mV s^{-1} for 5, 10, 20, 35 and 50 scans (A) together with SEM images of resulting Ag structures obtained after 5 (B), 10 (C), 35 (D) and 50 scans (E). Scale bar is 1 μm.

The mean sizes of obtained particles and the mean surface coverage calculated for 5 different SEM pictures of each sample are summarized in *Fig. 22 A* and *B*, respectively.

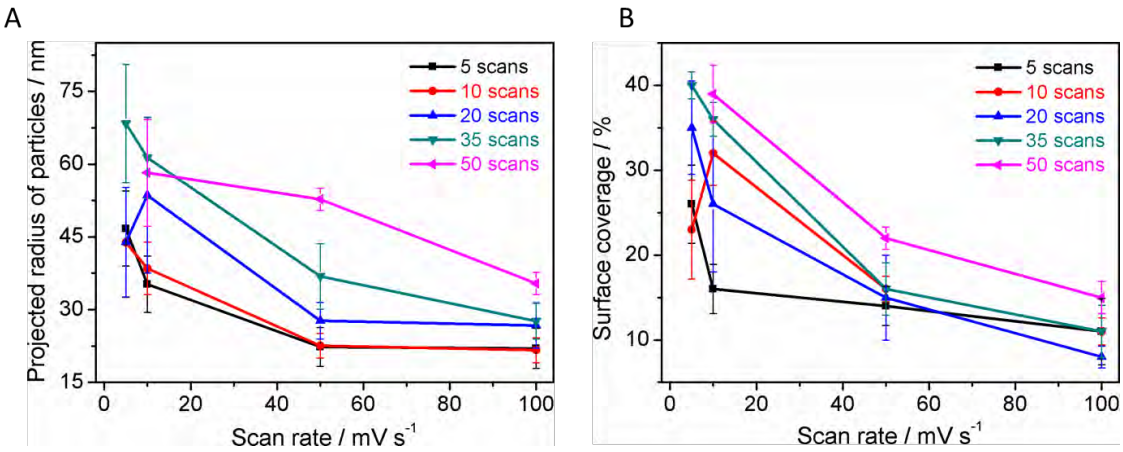

Fig. 22 Graphs depicting changes of size of obtained particles (A) and changes of surface coverage (B) with increasing number of scans for different potential scan rates.

Next the UV-Vis and SERS spectra were recorded. Respective EFs were calculated according to the procedure described in *Section 2.3.2.3* and summarized in *Table 2*. Samples obtained in some conditions revealed no SERS activity and it was impossible to calculate the EF value ("nd" in *Table 2*). There is no correspondence between obtained EF and used electrochemical parameters.

Representative examples of correlation of the morphology with the spectra are shown in *Fig. 23*. The highest and narrowest UV-Vis peak (FWHM = 43 nm) as well as the highest EF were obtained for the sample electrodeposited with 50 scans at 10 mV s^{-1}.

Table 2. Enhancement factors calculated for 4-ATP for respective AgNPs samples (nd = impossible to calculate/no data)

	5 scans	10 scans	20 scans	35 scans	50 scans
5 mV s^{-1}	10	10^2	10^3	nd	nd
10 mV s^{-1}	10	1.5×10^2	10^3	10^5	3×10^8
50 mV s^{-1}	30	nd	30	10^3	10^4
100 mV s^{-1}	nd	nd	nd	80	10^2

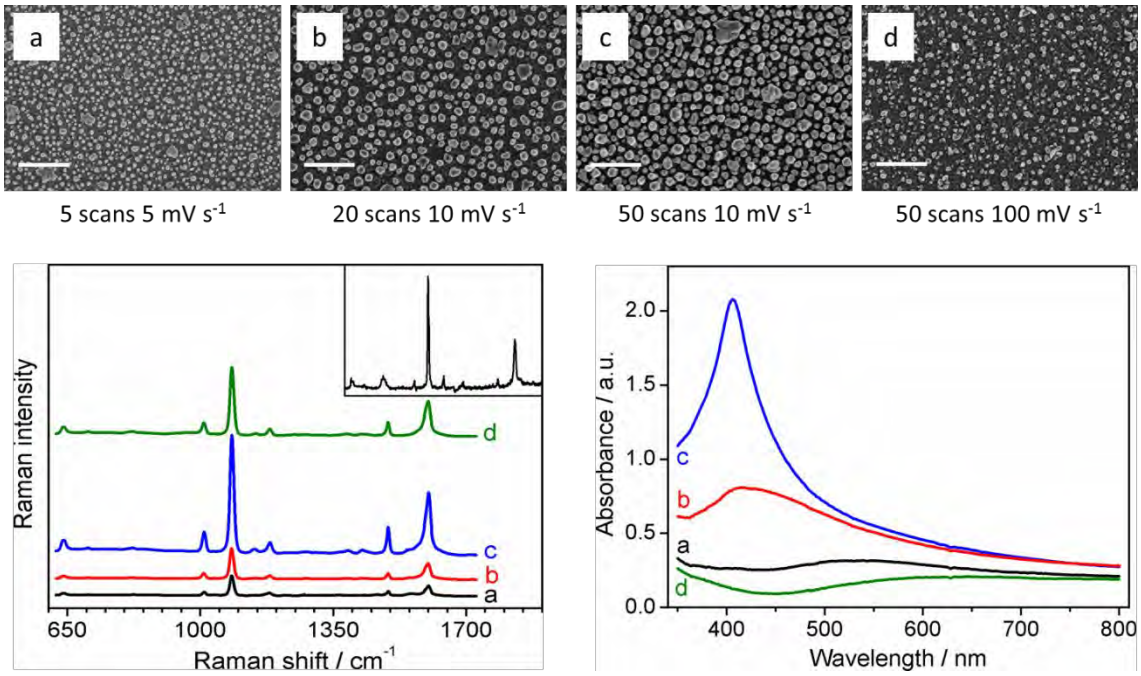

Fig. 23 Correlation of the SERS and UV-Vis spectrum with the morphology of the AgNPs – top: SEM images of selected samples (each scale bar represents 500 nm); bottom left: SERS spectra of 4-ATP obtained for respective AgNPs samples depicted at the top (laser wavelength: 632.8 nm, power: 5 mW, integration time: 10 s; inset shows the normal Raman spectrum of solid 4-ATP, laser wavelength: 632.8 nm, power: 60 mW, integration time: 60 s); bottom right: UV-Vis spectra of respective AgNPs samples measured in water.

Additionally it was checked *in-situ* how the UV-Vis spectrum was changing during the electrodeposition process. In order to do that the electrodeposition setup was placed inside the spectrophotometer and a spectrum was taken every 10 min during the process (50 scans at 10 mV s^{-1}). As can be seen in *Fig. 24A* the background level rises during the experiment suggesting increase of the AgNPs surface coverage density. The initial position of the absorption peak is around 430 – 450 nm. After 30 min of reaction (around 8th cycle) this peak starts to diminish and disappears. At the same time the peak at 400 nm appears and grows till the end of the experiment. This suggests that at the beginning of the process mostly big aggregates (~150 nm of diameter) are formed accompanied with lots of very small particles (what can be concluded from the increase of the absorbance in the range 350 – 450 nm). It is worth mentioning that the absorbance level for measured samples exceeds the value allowed by the Lambert-Beer law. The main reason for such behavior is the inhomogeneity of obtained samples. Metallic nanostructures are well known for their ability to scatter and reflect light. As can be seen in *Fig. 24A* a similar shape of the spectrum (with lower absorbance) to the one obtained for 50 scans can be obtained after 35 cycles only.

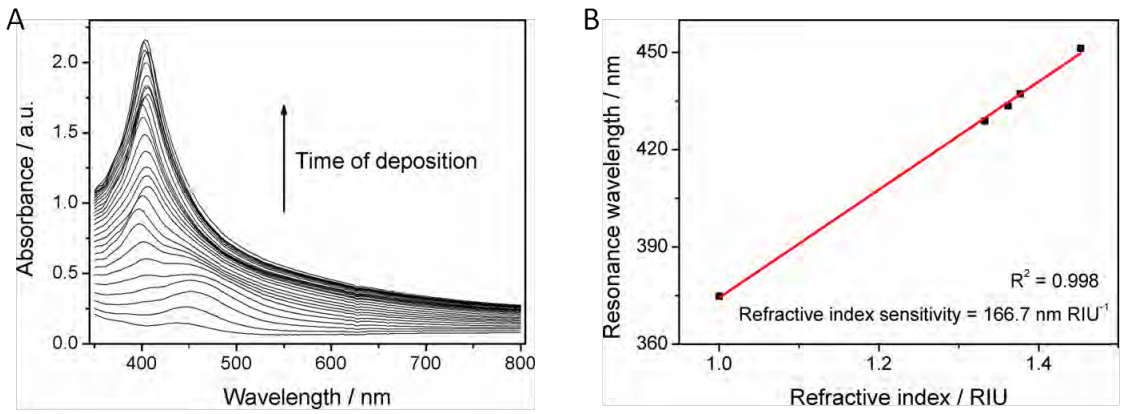

Fig. 24 A – The change of the UV-Vis spectrum of deposited Ag structures. Spectra were taken every 10 min during electrodeposition through 50 cycles at 10 mV s^{-1} in potential range 0 – -0.8 V; B - refractive index sensitivity of the same sample.

The refractive index sensitivity of the sample obtained at 10 mV s^{-1} after 50 cycles was calculated according to the procedure described in *Section 2.3.2.2* to be 166.7 nm RIU^{-1} (see *Fig. 24B*).

The influence of the amount of the reducing agent on the deposits morphology was also checked. Three separate baths were prepared containing 0, 0.25 and 2.5 mM solution of trisodium citrate (with concentration of the silver salt set at 0.25 mM). The best electrochemical conditions obtained in a previous section were used – 50 cycles at 10 mV s^{-1} in potential range 0 – -0.8 V. The as-obtained deposits morphology is shown in the top panel of *Fig. 25*.

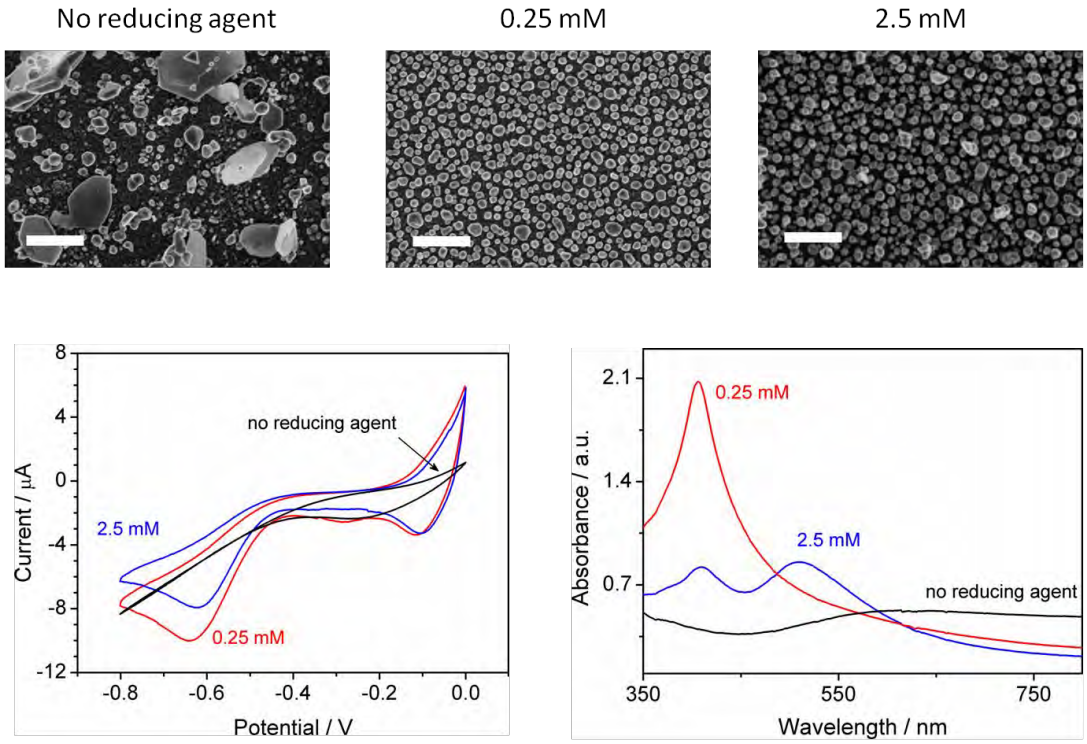

Fig. 25 Top: SEM images of deposits obtained with different amounts of trisodium citrate (scale bars represent 500 nm); bottom: corresponding voltammograms (left) and UV-Vis spectra (right, measured in water) of respective deposits.

Particles fabricated without a reducing agent are irregular and polydisperse. Addition of citrate ions caused creation of more regular (spherical) particles. Surface coverage density increased along with the increase of citrate ions concentration. In the voltammogram (left bottom of *Fig. 25*) it can be seen that increasing the concentration of trisodium citrate caused a minor shift of the silver reduction peak towards more positive potentials. It can be caused by polymerization of citrates at the surface of the working electrode. [171] At the UV-Vis spectrum (right bottom of *Fig. 25*) there is no distinct peak for the sample prepared without a reducing agent.

The sample fabricated with 0.25 mM solution of trisodium citrate shows well-developed peak with FWHM of 42 nm. Sample obtained from 2.5 mM solution of citrate exhibits two separate peaks. Furthermore the SERS measurements were performed and EF for each sample was calculated (according to the procedure described in *Section 2.3.2.3*). Despite the two UV-Vis peaks the sample fabricated with 2.5 mM solution of citrate showed the highest EF value: 6×10^8. For the one containing 0.25 mM solution of trisodium citrate EF value was 3×10^8. For the sample fabricated without trisodium citrate EF value was 10^4.

To check the influence of the amount of silver on the deposits' morphology the comparison between two types of baths was made. The amount of silver was increased 3 times (from 0.25 mM to 0.75 mM) and the amount of trisodium citrate was kept at 0.25 mM level. The deposition was conducted for 10 scans at 10 mV s^{-1}, 20 scans at 5 and 10 mV s^{-1} and 35 scans at 5 and 10 mV s^{-1}.

The analysis of SEM images revealed a good surface coverage density (see *Table 3*). Unfortunately, for the increased concentration of silver salt there was a tendency to create dendritic deposits as can be seen in *Fig. 26*.

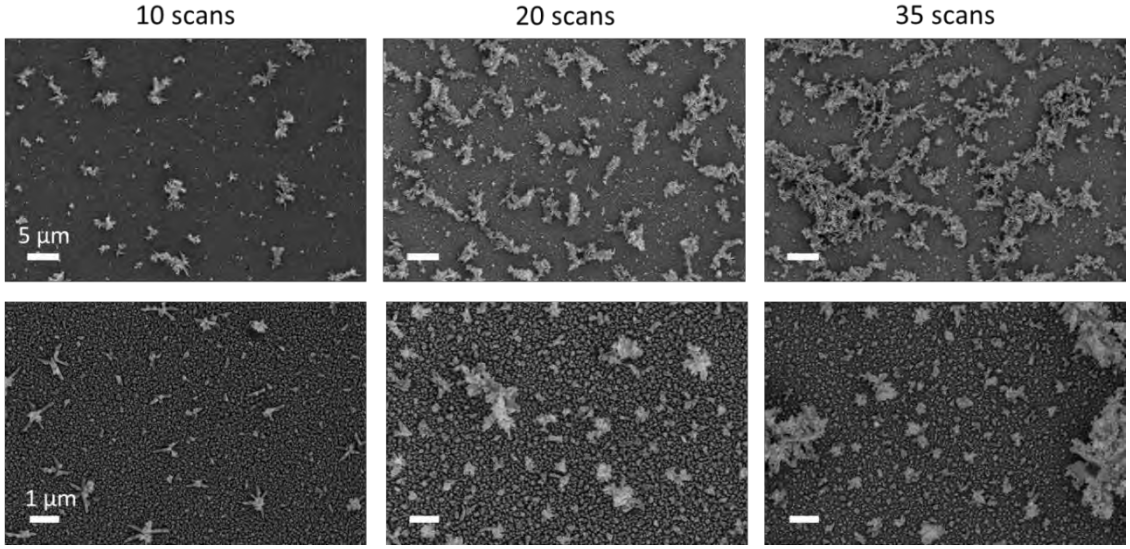

Fig. 26 SEM images presenting morphology of deposits obtained at potential scan rate of 10 mV s^{-1} with different number of scans. The plating bath contained 0.75 mM of silver nitrate and 0.25 mM of trisodium citrate. Bottom row shows enlarged fragments of pictures from the top row. Scale bars represent 5 µm for the top row and 1 µm for the bottom row.

Table 3. Summary of the surface coverage densities obtained for different electrochemical parameters using solutions: 0.75 mM of silver nitrate and 0.25 mM of trisodium citrate.

electrochemical parameters	10 scans 10 mV s^{-1}	20 scans 5 mV s^{-1}	20 scans 10 mV s^{-1}	35 scans 5 mV s^{-1}	35 scans 10 mV s^{-1}
surface coverage [%]	42.43 ± 1.59	45.82 ± 0.75	49.68 ± 0.75	41.95 ± 2.24	48.27 ± 1.30

As last the influence of stirring on the deposits' morphology was tested. The electrochemical setup was placed on the magnetic stirrer. The batch of samples was prepared from the same stock solution (0.25 mM of $AgNO_3$, 0.25 mM of trisodium citrate in total volume of 4.5 mL of water) and in the same electrochemical conditions (CV from 0 to -0.8 V, 50 scans at 10 mV s^{-1}) as

the "basic" samples. As-deposited samples were tested with UV-Vis spectrophotometry and compared to the sample prepared without stirring (*Fig. 27*). As can be seen the absorbance for "stirred" sample is high in majority of the tested range. It can be caused by the formation of flat, large structures, as presented in *Fig. 27*.

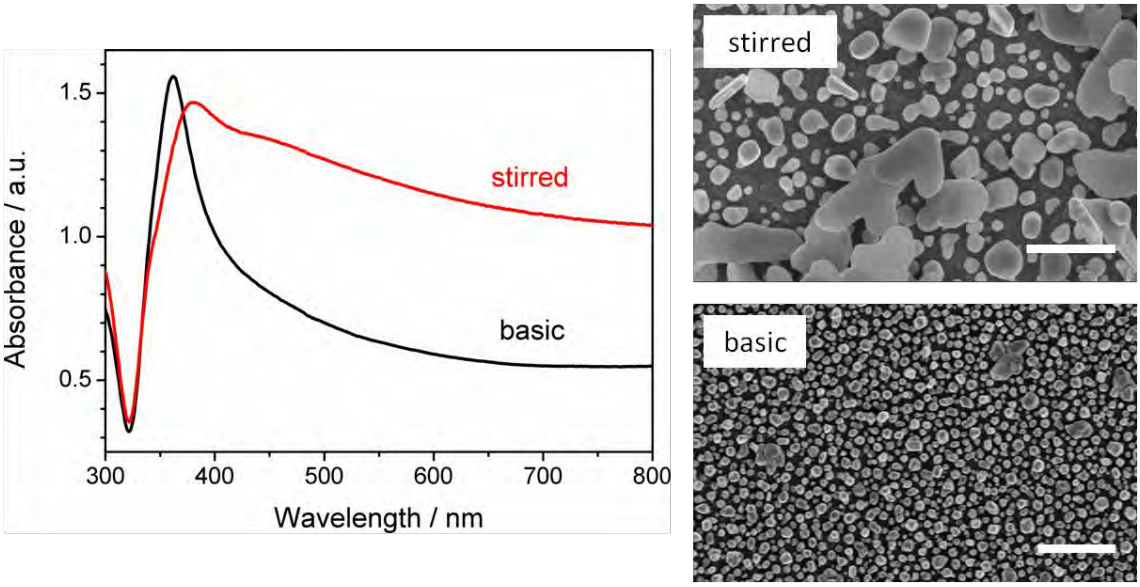

Fig. 27 UV-Vis spectra of samples prepared with and without stirring along with SEM images of respective samples: basic – without stiring, stirred – 600 rpm (scale bars represent 500 nm).

3.1.2 Mechanism of reduction of silver ions with citrate ions

The general mechanism, as it was described earlier in *Section 1.3.2*, includes oxidation and decomposition of citrate ions as well as coordination of both Ag^+ ions and Ag_2^+ dimers at the early stages of nucleation. It has been demonstrated [172] that the morphology of obtained structures depends on the pH of the reaction bath (since the reaction rate changes with pH). In low pH the reaction is long and results in formation of polygonal particles, while in high pH the reaction rate increases resulting in a mixture of spherical and rod-like particles. Thus the size and shape control (at least partially) depends on

the protonation level of the citrate ions. In our case the OH^- ions are produced directly at the surface of the electrode changing locally the pH of the solution, thus changing protonation level of the molecules in the vicinity of the electrode. Deprotonated citrate ion can bind strongly to the Ag^+ ions and Ag_x^+ aggregates. Those can further aggregate or undergo coalescense or recrystallization (resulting in a high-quality product with small amount of aggregates). [19, 22] Furthermore, citrate ions by binding and polymerizing on the ITO surface [171], ensure strong adhesion of created AgNPs to the surface of the electrode.

3.2 Other reducing agents

The suitability and efficiency of three other reducing agents were tested. The following compounds were chosen (structures are presented in *Fig. 28*): formic acid [173], ascorbic acid [174] and glucose. [175-180].

Formic acid is the simplest carboxylic acid. It was chosen because of its similarity to citrate ion.

Ascorbic acid is used as a weak reducing and stabilizing agent during formation of Au and Ag nanoparticles in the seed-mediated method. [170] It was proposed as a stabilizing agent to stimulate the growth of nuclei created on the surface by electrochemical reduction.

Glucose is known as a reducing agent used e.g. in production of silver mirrors. [181]

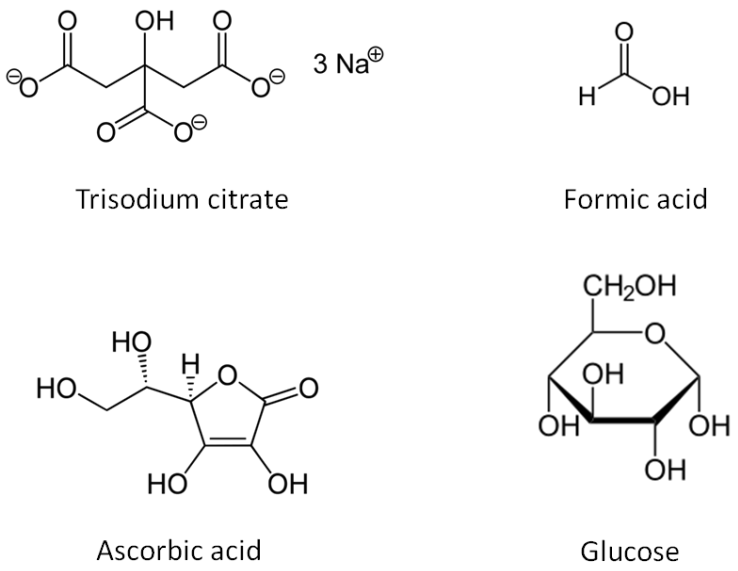

Fig. 28 Structures of tested reducing agents.

3.2.1 Formic acid

The effectiveness of the formic acid as a reducing agent was tested for 0.25 mM of silver nitrate. Since trisodium citrate solution was replaced with formic acid the deficiency of conducting Na^+ ions should have been compensated. That is why the solution of potassium nitrate was used as a supporting electrolyte. Examined baths contained 0.25 mM solution of silver nitrate and 0.25 or 2.5 mM solution of formic acid in total volume of 4.5 mL of 0.1 M potassium nitrate. As can be seen in *Fig. 29* there is no silver reduction visible for 0.25 mM solution of formic acid. However, for 2.5 mM solution the silver reduction peak appears at -0.55 V.

Subsequent experiments were performed in solution containing 2.5 mM of formic acid. Electrodeposition proceeded for 10, 20 and 50 scans at potential scan rate of 10 mV s^{-1}. In *Fig. 30* representative examples of the morphology of obtained deposits are presented, along with respective surface coverage density values (S.C.).

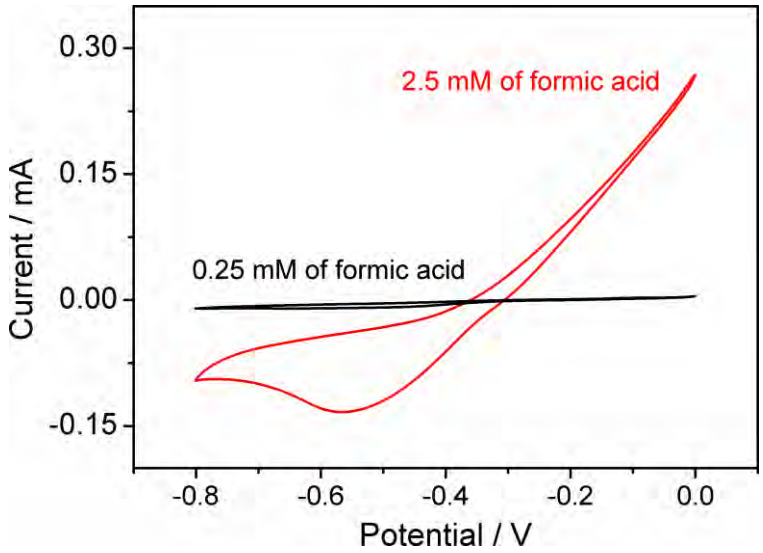

Fig. 29 Cyclic voltammograms for 10th scan at potential scan rate of 10 mV s^{-1} obtained in solution containing 0.25 mM of $AgNO_3$ and 0.25 or 2.5 mM of formic acid in total volume of 4.5 mL of 0.1 M KNO_3.

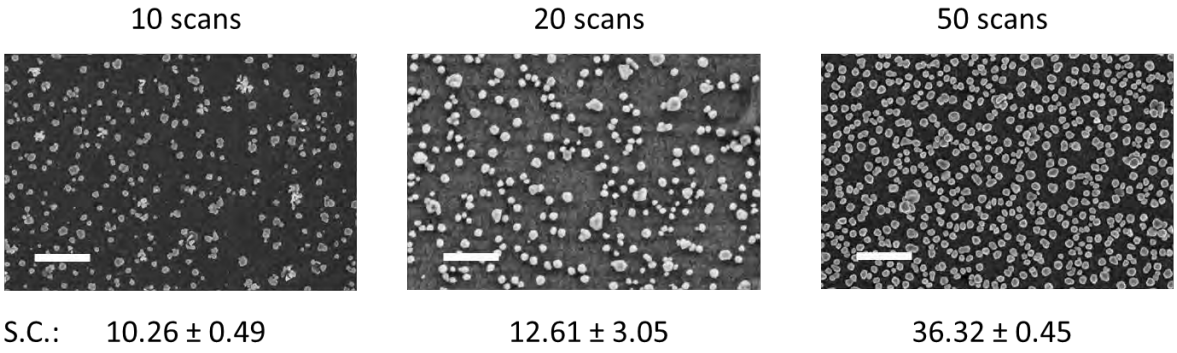

Fig. 30 SEM images depicting the morphology of deposits obtained from bath containing 0.25 mM $AgNO_3$ and 2.5 mM of formic acid in total volume of 4.5 mL of 0.1 M KNO_3; potential scan rate was 10 mV s^{-1}; scale bars represent 1 µm; S.C. refers to surface coverage and is specified in percent.

Generally, obtained deposits were less dense (surface coverage from 10 to 36%) and more disperse than those obtained with trisodium citrate and shown no required plasmonic properties (nor in LSPR nor in SERS). Increasing the

concentration of silver to 0.75 mM caused an increase of the surface coverage to around 32% for 10 scans at 10 mV s^{-1}. No consequent improvement of the optical properties of deposits was observed.

3.2.2 Ascorbic acid

In the case of the ascorbic acid it was expected that, despite its weak reducing properties, the electrochemical reduction itself will be sufficient to create Ag nuclei at the surface of the ITO. However, voltammograms showed no reduction peaks (data not shown) and no silver structures were deposited.

3.2.3 Glucose

3.1.3.1 Optimization of electrodeposition conditions

The last reducing agent to be tested was glucose. The electrodeposition solution consisted of solutions of $AgNO_3$ and glucose in total volume of 4.5 mL of 0.1 M of KNO_3. Cyclic voltammetry was done in a potential range from 0 to -0.8 V with different potential scan rates of 5, 10 or 100 mV s^{-1} and different numbers of scans: 5, 10 and 35.

A typical voltammogram is presented in *Fig. 31*. The onset potential of the silver reduction is -0.05 V and the current magnitude depends on the concentration of silver. A reduction peak below -0.7 V corresponds to reduction of residual oxygen on the deposited particles as it was in case of citrate-based reduction.

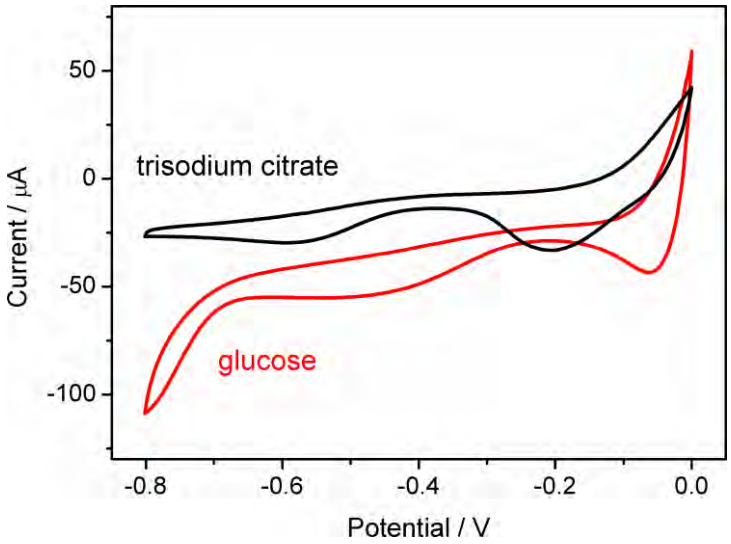

Fig. 31 A comparison of voltammograms obtained for 0.75 mM solution of silver nitrate with 0.25 mM solution of different reducing agents – glucose (in 0.1 M KNO_3) or trisodium citrate (in water).

As can be seen the peak of the silver reduction shifted towards more positive potential values than for citrate-mediated electroreduction. This phenomenon can be explained with adsorption and polymerization of citrate ions on the surface of the ITO as was described by Berkh *et al.* [171]

The effect of solution composition was investigated by UV-Vis spectrophotometry and SEM microscopy. Concentrations of silver salt and glucose were tuned. Electrochemical parameters were set at 35 scans at 10 mV s^{-1} in the range of potentials 0 – -0.8 V. *Fig. 32* presents samples fabricated with concentration of silver salt set at 0.25 mM and different concentrations of glucose.

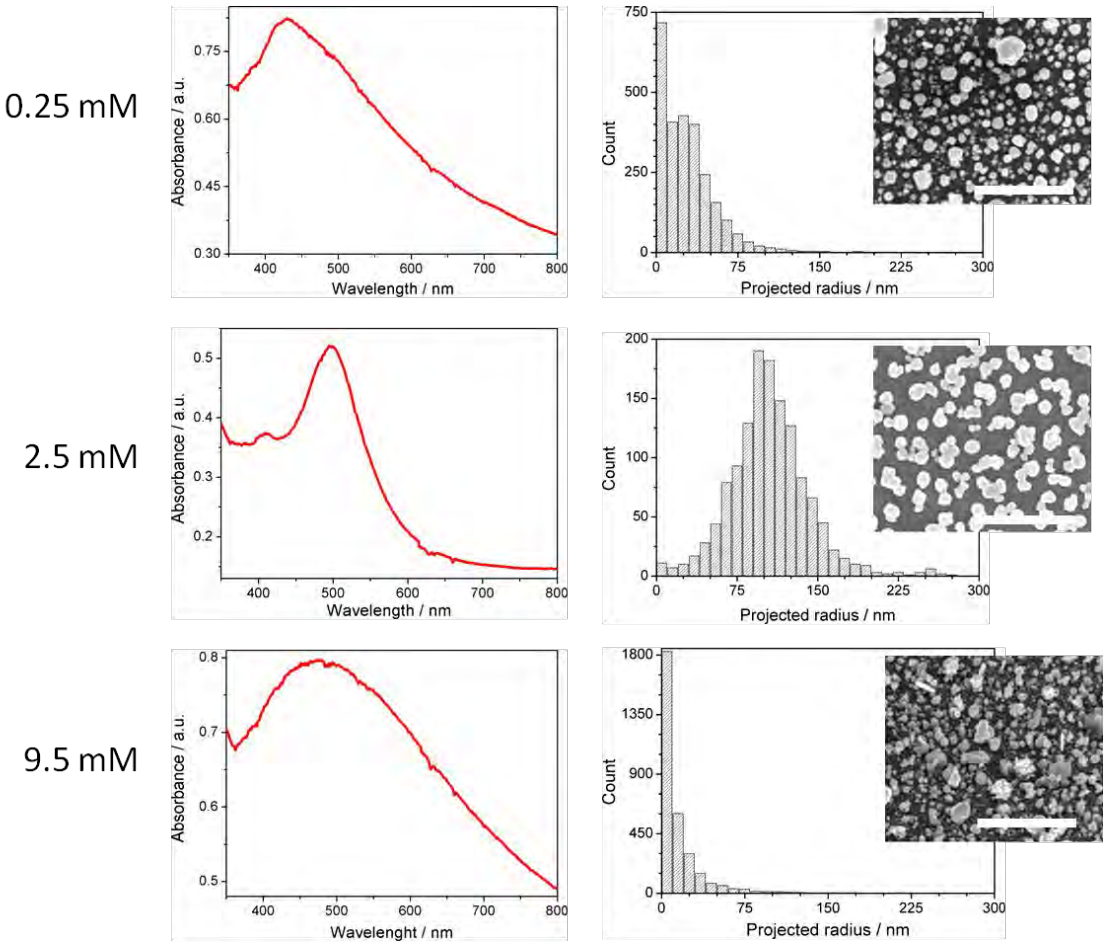

Fig. 32 UV-Vis spectra and SEM images of samples obtained from solution of 0.25 mM of silver nitrate and different concentrations of glucose in total volume of 4.5 mL of 0.1 M KNO_3. Scale bars represent 500 nm.

Fig. 33 presents results for 0.75 mM solution of silver salt with other parameters the same as described above. As can be seen the highest and the narrowest single absorption peak (FWHM = 66 nm) was obtained for 0.75 mM solution of silver salt and 0.25 mM solution of glucose in total volume of 4.5 mL of 0.1 KNO_3.

Sample prepared from solution of 0.25 mM silver ions and 2.5 mM of glucose exhibits two peaks. One of them, at 500 nm, has FWHM = 62 nm. The second, at 405 nm, is very small (height of 0.02 units, FWHM *ca.* 15 nm). As can be seen in SEM images in *Fig. 32*, for this sample NPs are mostly relatively big what corresponds with both, position and width of the absorption peak at 500 nm.

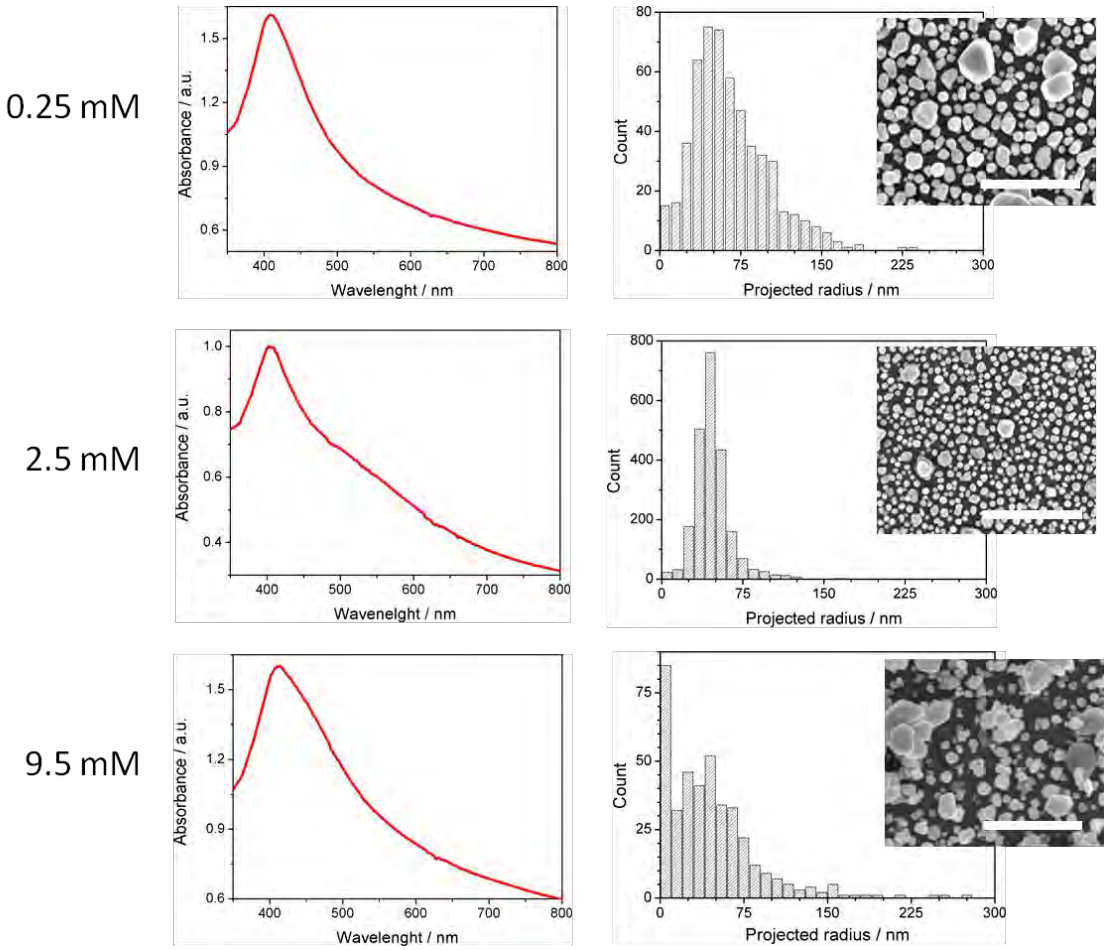

Fig. 33 UV-Vis spectra and SEM images of samples obtained from solution of 0.75 mM of silver nitrate and different concentrations of glucose in total volume of 4.5 mL of 0.1 M KNO_3. Scale bars represent 500 nm.

Low number of separate small particles results in a peak at 405 nm. Also the surface coverage is low what explains low background level of the UV-Vis spectrum (absorbance value for $\lambda = 800$ nm of about 0.15 units for 2.5 mM solution of glucose versus 0.5 units for 9.5 mM solution of glucose).

Subsequently, the behavior of the system in different pH values was tested. *Fig. 34* shows the UV-Vis spectra and morphology of deposits obtained from baths consisting of 0.75 mM of silver nitrate and 0.25 mM of glucose in 0.1 M KNO_3 at various pH values. pH was tuned using different amounts of

0.5 M H_2SO_4 (0 µL, 7 µL or 25 µL to obtain pH 7, pH 5 or pH 2, respectively) or 25% ammonium hydroxide solution (25 µL resulting in pH 10). As it was predicted, samples obtained in basic conditions showed a broad resonance peak caused by branched morphology of the deposits (*Fig. 34*). According to the literature [26] creation of $[Ag(NH_3)_2]^+$ ions should lead to branched crystallites with reduced size. The resonance peak obtained at pH 7 has FWHM of 55 nm and it was the best result among other pH values.

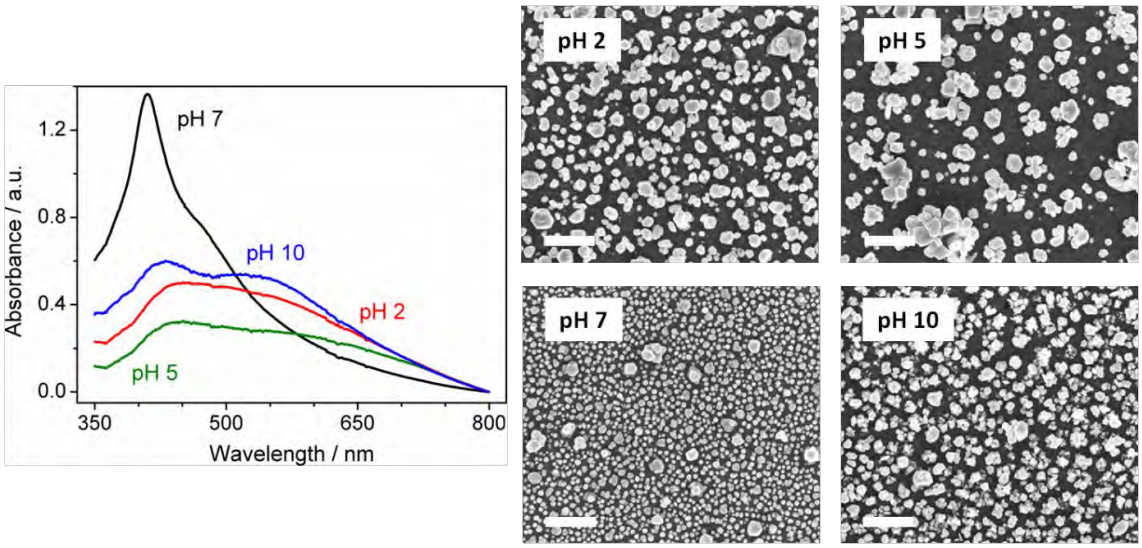

Fig. 34 UV-Vis spectra (measured in air) and SEM images obtained for samples prepared from 0.75 mM $AgNO_3$ and 2.5 mM glucose in 0.1 M KNO_3 in various pH; 35 scans at 10 mV s^{-1}. Scale bars represent 1 µm.

The size and surface coverage density dependence on number of scans and scan rate were studied using SEM images. Results are summarized in *Table 4*.

One can easily note the influence of the potential scan rate on the particles size. As in case of preparation of silver particles, the average projected radius (r) decreases with the increase of the potential scan rate (from about 50 nm at 5 mV s^{-1} to 25 nm at 100 mV s^{-1}). When the scan rate is increased to 100 mV s^{-1}, the particle deposit is quite sparse – about 26% while for 5 mV s^{-1} it is about

39%. Increase of the number of scans applied causes increase of the surface coverage density values.

Table 4 Average projected radiuses and surface coverages of the AgNPs electrodeposited in different conditions from solution of 0.75 mM $AgNO_3$ and 0.25 mM glucose in 0.1 M KNO_3, pH 7.

	5 scans	10 scans	35 scans
5 mV s^{-1}		r = 52.12 ± 31.17 nm 39.1 ± 1.25 %	
10 mV s^{-1}	r = 113.76 ± 46.69 nm 26.13 ± 1.33 %	r = 47.22 ± 17.7 nm 36.9 ± 0.78 %	r = 66.46 ± 38.75 nm 46.53 ± 5.68 %
100 mV s^{-1}		r = 27.53 ± 18.31 nm 26.3 ± 2.21 %	

Typical UV-Vis spectra of samples prepared in different experimental conditions and corresponding SEM images are presented in *Fig. 35* and *Fig. 36*.

Low density of the surface coverage causes low background level in the UV-Vis spectrum (compare SEM image and UV-Vis spectrum for 5 scans in *Fig. 35*). Polydispersity induce broadening of the peak or even formation of an additional peak in the UV-Vis spectrum as for the sample prepared with 10 scans an 10 mV s^{-1} (*Fig. 35* and *36*).

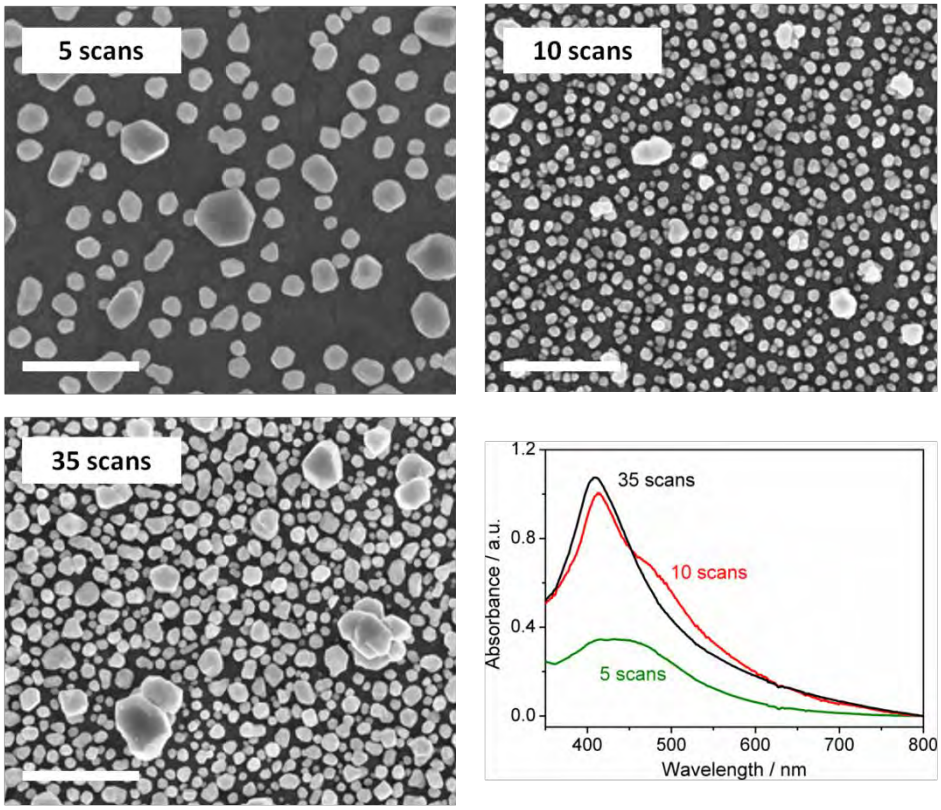

Fig. 35 Dependence of UV-Vis spectra (measured in air) on number of scans applied during electrodeposition (at potential scan rate set at 10 mV s^{-1}) from 0.75 mM $AgNO_3$ and 0.25 mM glucose in 0.1 M KNO_3 along with SEM images of adequate samples (scale bars represent 1 μm).

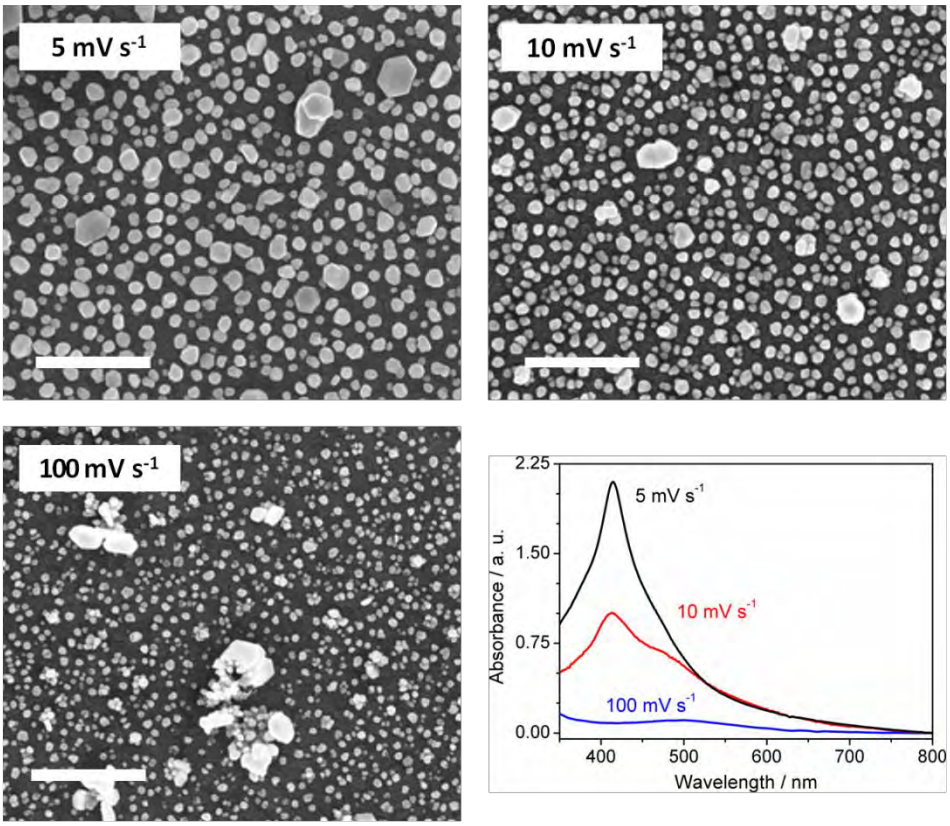

Fig. 36 Dependence of UV-Vis spectra (measured in air) on potential scan rate applied during electrodeposition (for 10 scans) from 0.75 mM $AgNO_3$ and 0.25 mM glucose in 0.1 M KNO_3. Next to them are presented SEM images of adequate samples (scale bars represent 1 µm).

On the basis of earlier experiments the optimal composition of the solution was chosen. The narrowest resonance peak was obtained after 10 scans of CV at potential scan rate of 5 mV s^{-1} from solution of 0.75 mM $AgNO_3$ and 0.25 mM glucose in 0.1 M KNO_3, pH 7. Its refractive index sensitivity was established to be 128.8 nm RIU^{-1} (according to the protocol described in *Section 2.3.2.2*).

3.1.2.1 Proposed mechanism of reduction of silver ions with glucose

In the literature one can find two proposed paths of silver reduction with glucose. [176] Both are based on the presence of hydroxyl ions in solution. According to the first one the OH^- reacts with glucose resulting in gluconate ions which reduce silver ions to the atomic form. Second one describes generation of silver atoms *via* reduction of Ag_2O with glucose. The path of the reaction strongly depends on the pH of the solution – with the increase of the pH, the second mechanism becomes prevailing. Proposed mechanisms assume that in water solution one can find two forms of glucose – cyclic and open-chain – which are transforming into each another *via* mutarotation. [182] The mutarotation occurs most effectively when both, acidic and basic catalysts are present in solution. Our basic catalyst, OH^-, is produced near the electrode surface during electrode process while silver ions can be regarded as acidic catalyst. The electron flow ensures that silver remains in the atomic form. Schematic representation of proposed mechanism is presented in *Fig. 37* below.

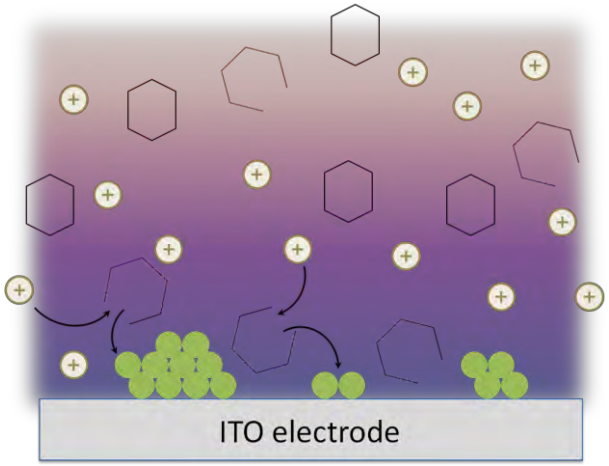

Fig. 37 A schematic representation of mechanism of glucose-assisted reduction of silver ions. Hexagons represent cyclic glucose, open hexagons represent open-chain form of glucose, circles with "+" signs represent silver ions and green circles represent reduced Ag atoms.

3.1.2.2 PVP addition

In order to enhance the AgNPs geometry the poly(vinyl pirrolidone) (PVP) was used. PVP binds more strongly to the <100> than <111> facets of Ag crystals and can thereby reduce the growth rate along the <100> direction, resulting in the formation of nanocubes/nanobars capped by <100> facets. [172, 183] Polyhedral silver nanocrystals are reported to alter plasmonic properties (thanks to distinct light scattering properties) thus resulting in higher enhancement factors in SERS and higher sensitivity for refractive index in LSPR. [184]

To find optimal conditions 35 µL of freshly made PVP solutions of different concentrations were added to the bath containing 0.75 mM $AgNO_3$ and 0.25 mM glucose in total volume of 4.5 mL of 0.1 M KNO_3. Changes in UV-Vis spectra between samples obtained with 0.25%, 0.5%, 0.75% and 1% wt. solution of PVP in water were compared (*Fig. 38*).

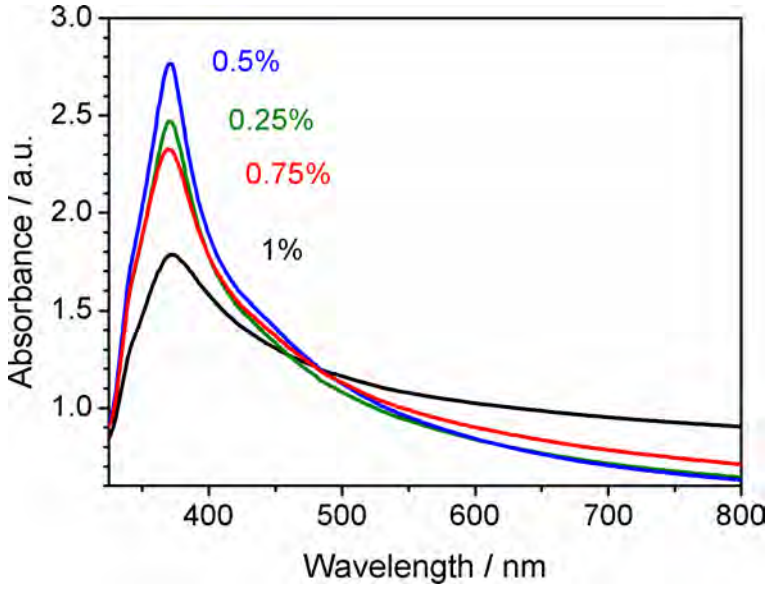

Fig. 38 UV-Vis spectra of platforms obtained with different concentrations of PVP (measured in air).

As can be seen the full width at half maximum (FWHM) value does not depend linearly on the PVP concentration. For the sample obtained with 0.5% of PVP the RIS value was calculated according to the procedure described in *Section 2.3.2.2* to be 233.7 nm RIU^{-1}. However the fabrication process was irreproducible. A probable cause is that PVP in such experimental conditions exists in solution in form of random coils which can entangle between each other. [185] This phenomenon is very difficult (if possible) to control.

3.3 Summary and conclusions

This chapter of the dissertation was dedicated to the use of cyclic voltammetry to obtain silver-based plasmonic platforms. To evaluate obtained substrates the scanning electron microscopy, UV-Vis spectroscopy and/or surface enhanced Raman spectroscopy were used.

The experiments showed that the range of potentials used influences the morphology of obtained deposits. The projected radii of particles as well as the surface coverage decrease with the increase of the potential scan rate. Also they increase with the increase of the number of performed scans of the CV.

For the electrodeposition of AgNPs four different reducing agents were tested: trisodium citrate, formic acid, ascorbic acid and glucose. Only two of them were suitable for obtaining desired platforms – trisodium citrate and glucose. Formic acid showed reducing properties towards silver but obtained deposits were less dense than those obtained with trisodium citrate. Moreover, they did not show desired plasmonic properties – nor in LSPR nor in SERS. In case of ascorbic acid pure electrochemical reduction was not enough to form nucleation seeds. Thus, no deposits were obtained. For trisodium citrate and for glucose it was tested how the morphology of the deposit is influenced by: electrochemical parameters, concentration of the reducing agent and the ratio

between reducing agent and silver salt. Moreover, the effect of addition of polyvinylpyrrolidone (PVP) to the glucose-based plating bath was examined and rejected because of very low reproducibility of the process.

The *in situ* UV-Vis experiment disclosed changes in sizes of the electrodeposited Ag structures during the course of the process. It can be related to the recrystallization of growing particles as was shown by Ustarroz *et al.* [18] The shape of resulting UV-Vis spectra depend on the morphology of the deposits – size of particles, their dispersity and distribution on the surface. In case of the AgNPs the best plasmonic peaks were obtained for particles having a projected diameter of ~120 nm. The high and narrow resonance peak results in high refractive index sensitivity of the substrate. There are grounds to believe a relationship between RIS and SERS enhancement factor exists (see *Fig. 23* in *Section 3.1.1*). It is planned to be examined in the near future.

As a result, two types of platforms which exhibited desired plasmonic properties were obtained. The first one, called from now on AgCitNPs, was prepared using equimolar (0.25 mM) solutions of silver nitrate and trisodium citrate in water. The electrodeposition was performed in the range of potentials 0 – -0.8 V for 50 scans at potential scan rate of 10 mV s^{-1}. It exhibited high SERS enhancement factor – 3×10^8 and good refractive index sensitivity of 166.7 nm RIU^{-1}. The second procedure resulting in good plasmonic properties of deposits was electrodeposition of silver particles from glucose-containing bath (AgGluNPs). The potential range was 0 – -0.8 V. The best resonance peak was obtained for 10 scans at 5 mV s^{-1} of electrodeposition from the solution of 0.75 mM of $AgNO_3$ and 0.25 mM of glucose in 0.1 M KNO_3. The platform exhibited RIS of 128.8 nm RIU^{-1}.

Chapter 4

Electrodeposition of gold submicrostructures

4.1 Reduction with citrate ions

The initial solution used for electrodeposition of gold submicrostructures contained equimolar (0.25 mM) aqueous solutions of $HAuCl_4$ and trisodium citrate. In the first step the range of potentials for CV was established. As can be seen in *Fig. 39* reduction of gold ions occurs at 0.35 V and -0.55 V.

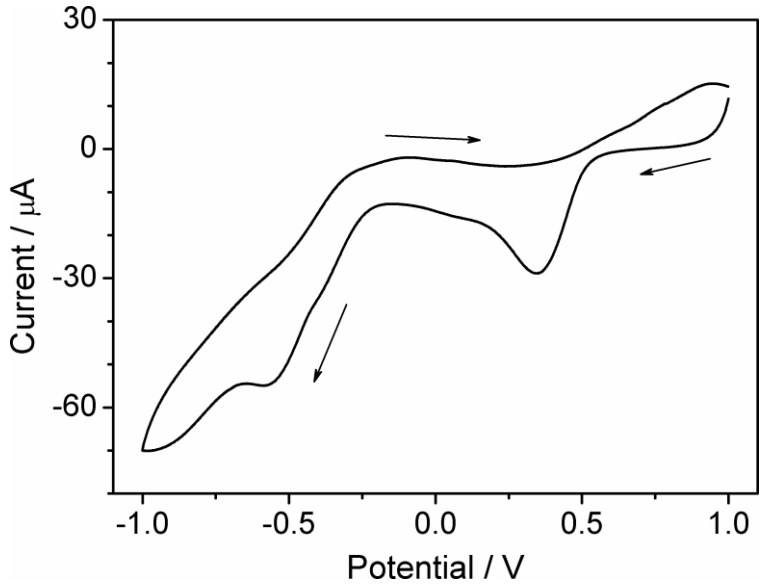

Fig. 39 Cyclic voltammetry in a broad potential range recorded in solution: 0.25 mM of $HAuCl_4$ and 0.25 mM of trisodium citrate in the total volume of 6 mL of deionized water; potential scan rate: 10 mV s^{-1}. Arrows indicate the direction of the scan.

The most probable mechanism is a multistep reduction of gold ions. At first, citrate ions are oxidized donating electrons to reduce Au^{3+} to Au^{+} according to following equations [113]:

$$[Au^{3+}(Cl^{-})_2(OH^{-})_2]^{-} + [C_6H_5O_7]^{3-} \longrightarrow [Au^{3+}Cl^{-}(OH^{-})_2(C_6H_5O_7)^{3-}]^{3-} + Cl^{-} \quad (11)$$

$$[Au^{3+}Cl^{-}(OH^{-})_2(C_6H_5O_7)^{3-}]^{3-} \longrightarrow CO_2 + 2Cl^{-} + [Au^{+}(OH^{-})]^{-} + [C_5H_5O_5]^{-} \quad (12)$$

Next, the reduction of Au^{+} to Au^{0} occurs at the surface of the working electrode causing deposition of gold atoms. Similar as in the case of silver electrodeposition, the oxygen reduction onset potential is around -0.65 V. For further experiments the potential range 0.5 – -0.8 V was chosen to assure reduction of residual oxygen on the surface of deposited NPs.

First parameters taken into consideration were the applied number of scans and potential scan rate. The relation between sizes of particles and surface coverage with applied electrochemical parameters is shown in *Fig. 40*. It can be seen that both, size and coverage density are generally increasing with decrease of the potential scan rate and with increase of the number of scans applied. Big error bars indicate polydispersion of obtained particles.

The enhancement factor of resulting structures was calculated according to the procedure described in *Section 2.3.2.3* and summarized in *Table 5*. Generally EF decreases with an increase of the scan rate. The highest EF was obtained for AuNPs deposited within 5 scans at potential scan rate of 5 mV s^{-1}. One order of magnitude lower values were obtained for samples fabricated at 5 – 10 mV s^{-1} for 10 – 35 scans.

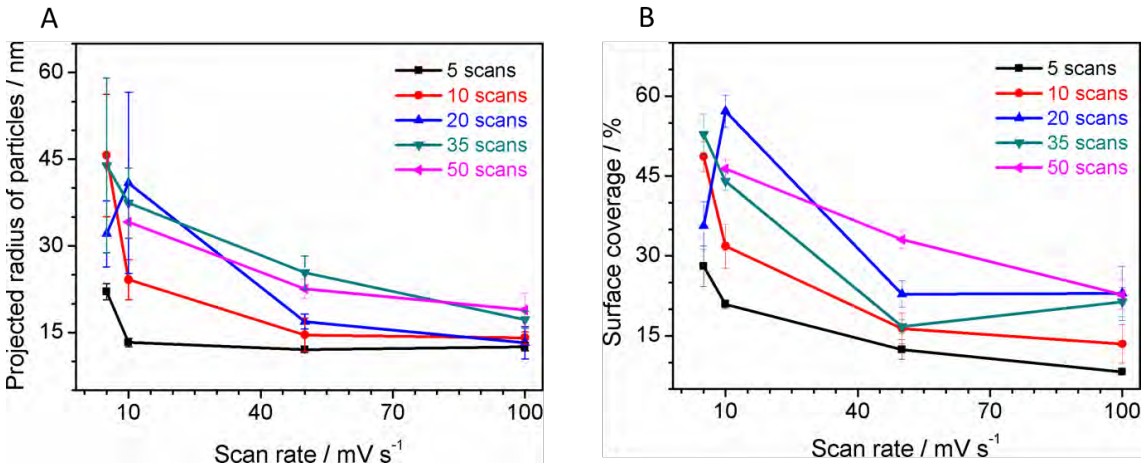

Fig. 40 Graphs depicting changes of size of obtained particles (A) and changes of surface coverage (B) with increasing number of scans.

Table 5. SERS enhancement factors obtained for 4-ATP on platforms obtained in different electrochemical conditions from 0.25 mM solutions of chloroauric acid and trisodium citrate in total volume of 6 mL of water.

	5 scans	10 scans	20 scans	35 scans	50 scans
5 mV s^{-1}	10^6	10^5	10^5	10^5	nd
10 mV s^{-1}	10^2	10^5	10^5	10^5	10^4
50 mV s^{-1}	10^2	10^3	50	10^2	10^4
100 mV s^{-1}	nd	10^2	nd	10^3	3×10^2

None of tested parameters resulted in intended UV-Vis spectrum. The representative example of obtained spectra is depicted in *Fig. 41* together with SEM images of respective structures.

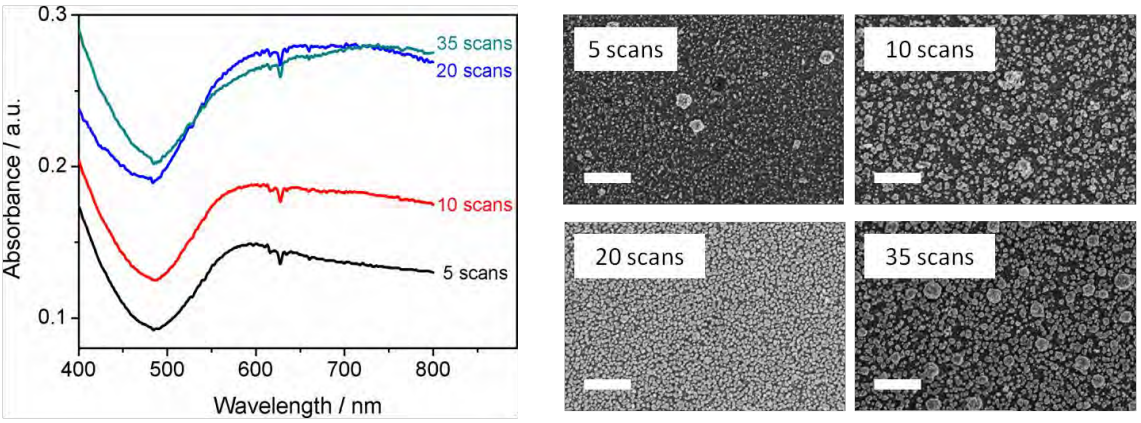

Fig. 41 UV-Vis spectra recorded in air for samples obtained with different numbers of scans at potential scan rate set at 10 mV s^{-1} along with SEM images of respective structures (scale bars represent 500 nm).

Because of unsatisfactory results other compositions of the solution were examined.

First of all the influence of the amount of gold salt and of reducing agent were tested. An increase of forty fold of the concentration of the reducing agent in the solution (from 0.25 mM to 10 mM) resulted in apperance of the peak around 550 nm in the UV-Vis spectrum of the obtained deposit. An additional change of the concentration of the gold salt (from 0.25 mM to 0.75 mM) caused almost two fold growth of the intensity of this peak and a small red-shift of the peak maximum (see *Fig. 42*).

Changing the concentrations of used chemicals changed also the conductivity of the solution. To check whether the change of the ionic strength of the bath will improve the properties of deposits the water was replaced with 0.1 M KNO_3. The screening was made for 5 scans at 10 mV s^{-1} and 50 scans at 100 mV s^{-1}. Tested compositions are listed in *Table 6*.

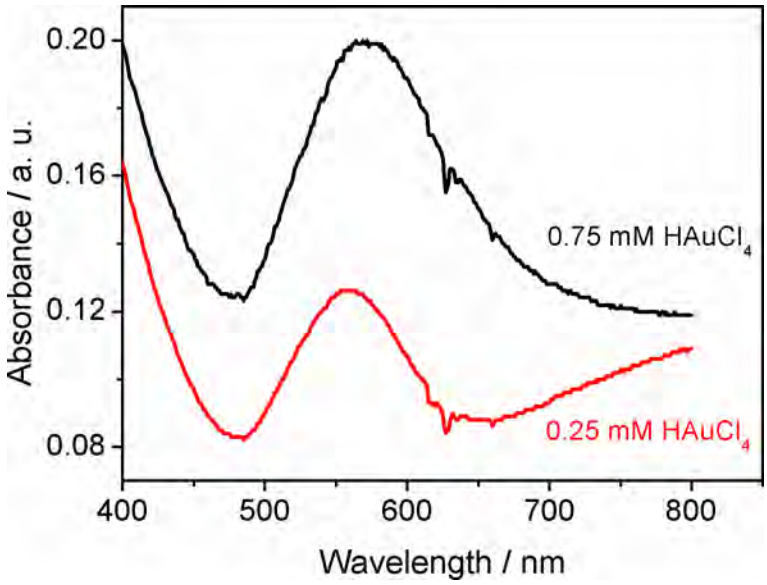

Fig. 42 Comparison of UV-Vis spectra (measured in air) of samples obtained with 0.25 and 0.75 mM solutions of $HAuCl_4$ with 10 mM solution of trisodium citrate (35 scans at 50 mV s^{-1}).

Comparing UV-Vis spectra of samples electrodeposited from solutions without (*Fig. 41*) or with KNO_3 (*Table 6*) it is clearly visible that the increase of the solution ionic strength improved the process. Even when 0.25 mM solutions of both, reducing agent and gold precursor were used, it was possible to obtain samples exhibiting distinguishable absorption peaks at the UV-Vis spectrum. FWHM value was still not satisfactory (the lowest is 88 nm for sample electrodeposited for 5 scans at 10 mV s^{-1} from 0.25 mM $HAuCl_4$ and 0.25 mM trisodium citrate) and escalated with the increase of citrate ions concentration. Increment of amount of gold caused an increase of height of the absorbance peak in the UV-Vis spectrum.

Table 6. Comparison of UV-Vis spectra of platforms obtained from different solutions in 0.1 M KNO_3 (measured in air)

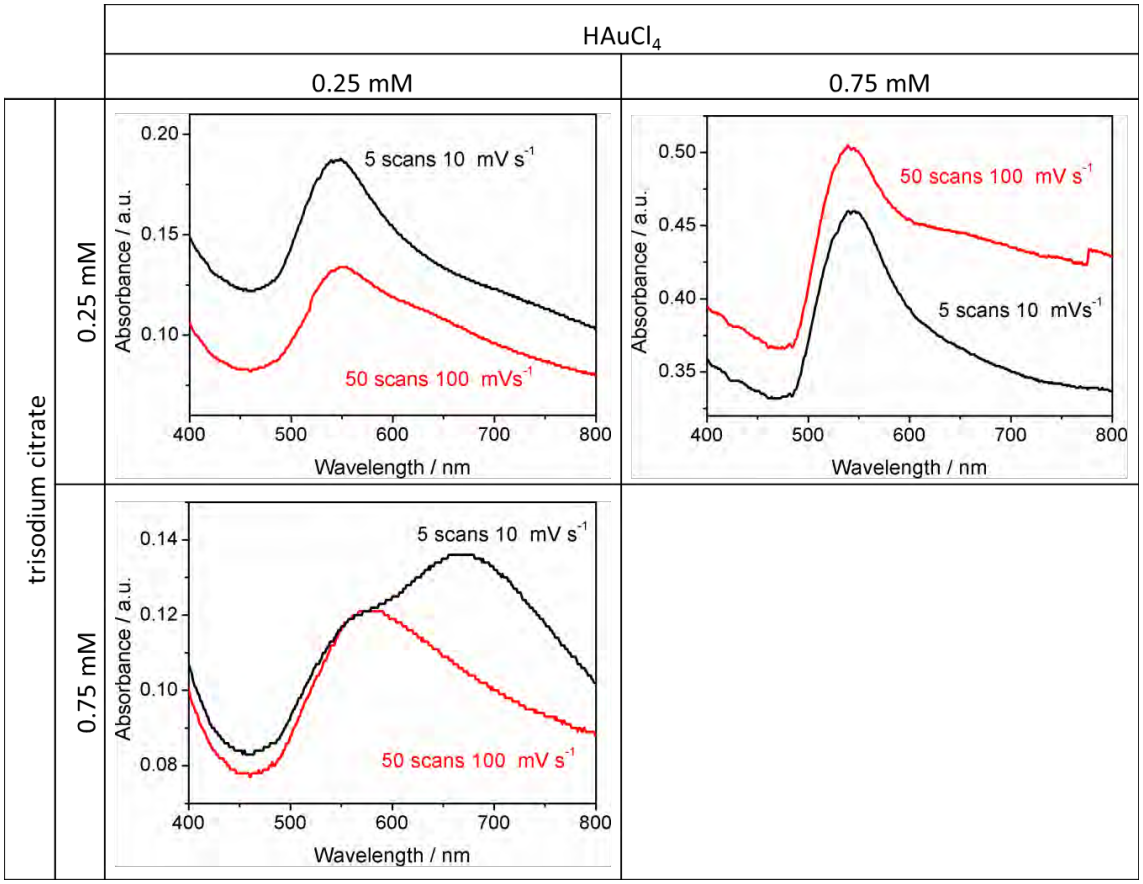

In the next step the proportion between the concentration of gold ions and the reducing agent was changed to 3:1. The composition of the resulting solution was 0.27 mM $HAuCl_4$, 0.09 mM trisodium citrate in total volume of 6.2 mL of 0.1 M KNO_3. The efficiency of the electrodeposition was measured with UV-Vis spectrophotometry for 5 scans at 5 mV s^{-1} and 10 or 25 scans at 10 mV s^{-1} (*Fig. 43*). The best spectrum was obtained for 25 scans at 10 mV s^{-1} although the FWHM value was very high – 95 nm. High background level suggests desired, high surface coverage density of the AuNPs.

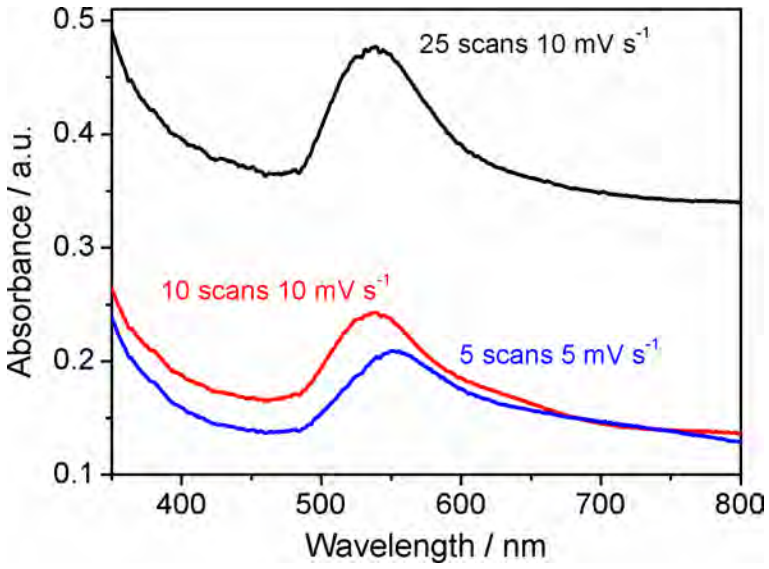

Fig. 43 A comparison of UV-Vis spectra (measured in air) of platforms obtained at different electrochemical conditions with 3:1 ratio between gold salt and trisodium citrate as a reducing agent.

For three samples prepared the same way (25 scans 10 mV s^{-1}, 0.27 mM $HAuCl_4$, 0.09 mM trisodium citrate in 0.1 M KNO_3) the UV-Vis spectra were recorded and the SERS experiment with 4-ATP was performed (according to the procedure described in *Section 2.3.2.3*). *Fig. 44A* depicts how the UV-Vis spectra changed from one sample to another. The reproducibility of the spectra is very low. On *Fig. 44B* three SERS spectra of 4-ATP taken at three different samples are presented. As can be seen for SERS the reproducibility between samples is very good. The calculated value of EF was 5×10^7.

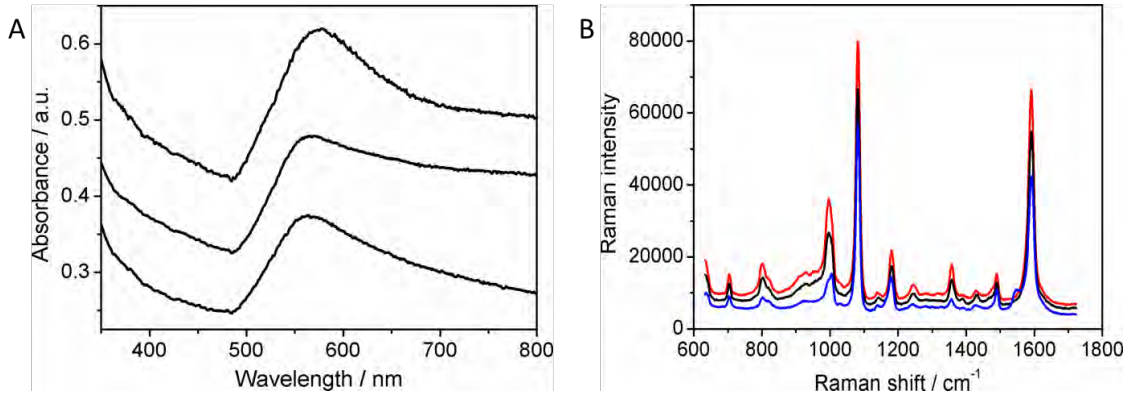

Fig. 44 A – Comparison of UV-Vis spectra of three different platforms electrodeposited with 25 scans at 10 mV s^{-1} with trisodium citrate as a reducing agent (measured in air); B – SERS spectra of 4-ATP recorded on the same samples (laser wavelength: 785 nm, power: 2 mW, integration time: 10 seconds).

4.2 Reduction with glucose

Subsequently the efficiency of glucose as a reducing agent was tested. The same composition of the solution was used: 0.27 mM of $HAuCl_4$ and 0.09 mM of glucose in 0.1 M KNO_3. Exemplary UV-Vis spectra recorded on three different platforms are shown in *Fig. 45A* together with the SERS spectra for 4-ATP recorded on the same samples (*Fig. 45B*). It is worth to notice that despite not ideal shape and poor reproducibility of UV-Vis spectra, the SERS spectra are very reproducible (including almost the same background level). Possibly the difference in the size of a measured spot is the cause – in the UV-Vis experiment the signal is collected from the area of 20 mm^2 while in the SERS experiment the beam area is 20 μm^2 and the signal is averaged from 25 separate points. Comparing to the aforementioned platforms obtained using trisodium citrate, platforms produced with glucose have higher reproducibility between samples (in case of both, UV-Vis and SERS experiments). For this type of platforms the calculated value of EF was 1×10^7.

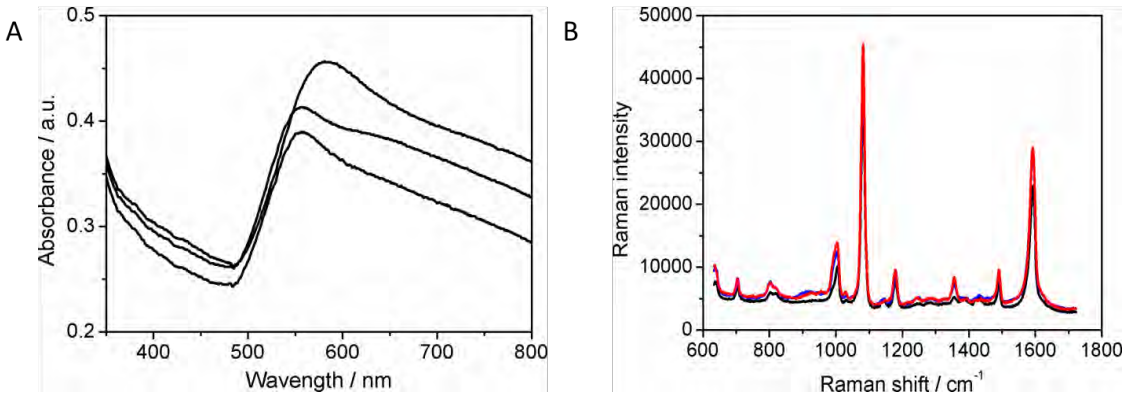

Fig. 45 A – UV-Vis spectra of 3 different platforms electrodeposited for 25 scans at 10 mV s^{-1} with glucose as a reducing agent (measured in air); B – SERS spectra of 4-ATP recorded on the same samples (laser wavelength: 785 nm, power: 2 mW, integration time: 10 seconds).

For comparison, electrodeposition of gold structures without use of any reducing agent was performed. The solution consisted of 0.27 mM of gold salt in total volume of 6.2 mL of 0.1 M KNO_3. As previously, the cyclic voltammetry proceeded for 25 scans at the potential scan rate of 10 mV s^{-1}. Like in previous two cases, the UV-Vis spectra are different between all three platforms (*Fig. 46A*). However SERS spectra (*Fig. 46B*) are very similar. The calculated EF value was 4×10^7.

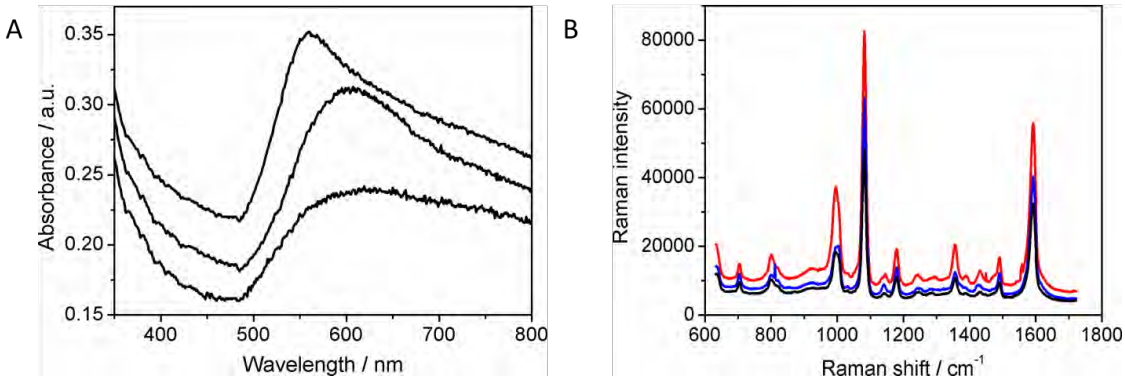

Fig. 46 A – UV-Vis spectra of 3 different platforms electrodeposited for 25 scans at 10 mV s^{-1} without a reducing agent (measured in air); B – SERS spectra of 4-ATP recorded on the same samples (laser wavelength: 785 nm, power: 2 mW, integration time: 10 seconds).

A comparison of morphologies resulting from the use of different solutions is presented in *Fig. 47*. Reduction with citrate ions (*Fig. 47A*) resulted in dense surface coverage with round-shaped particles. In case of reduction with glucose (Fig. *47B*) the number of protrusions ("bumpy" structures of aggregates) is reduced in comparison to citrate-mediated reduction. Moreover, the particles obtained with glucose show more sharp edges and corners (see *Fig. 47B2*). For the platforms obtained without any reducing agent (Fig. *47C*) the deposit is quite sparse and particles are polydisperse with irregular shapes.

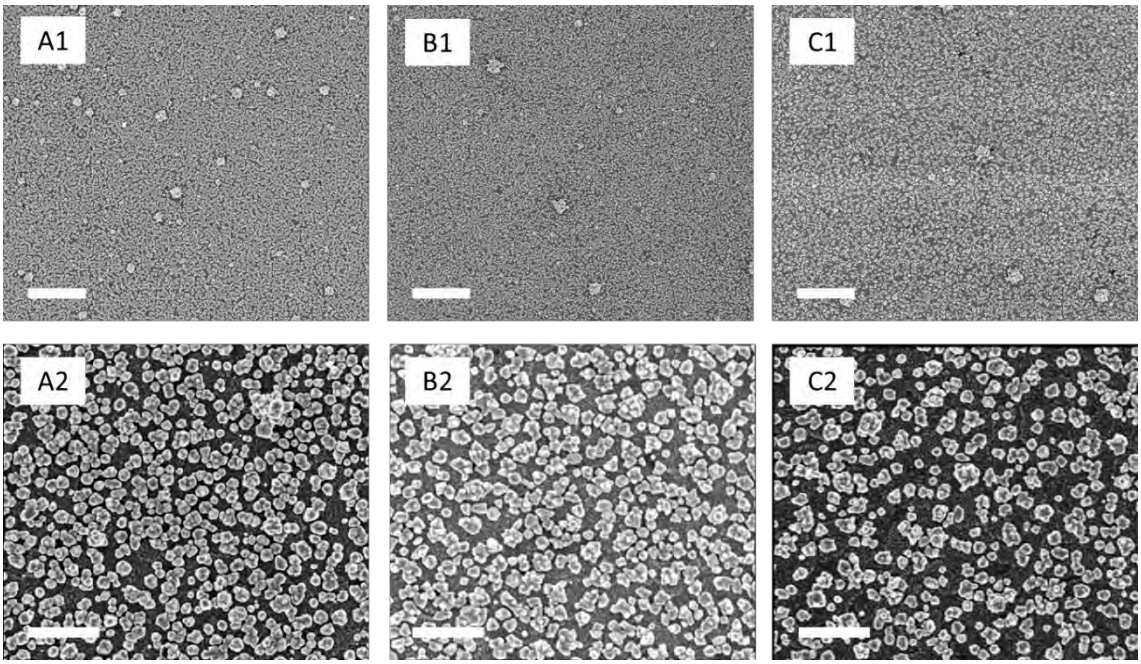

Fig. 47 Comparison of gold morphologies obtained with trisodium citrate (A), glucose (B) or without any reducing agent (C); scale bars for panel 1 (top) represent 2 µm, for panel 2 (bottom) – 500 nm.

4.2.1 PVP addition

As in the case of silver nanoparticles deposition attempts were made to improve the UV-Vis spectra of gold-based substrates fabricated with glucose by adding a freshly made PVP solution. Three different PVP solutions were tested:

0.25%, 0.5% and 0.75% wt. in amounts of 35, 70 and 140 µL. The evaluation was done for 50 scans at 50 mV s^{-1}. The narrowest peak (FWHM = 195 nm) was obtained with 140 µL of 0.5% PVP solution (see *Fig. 48* for comparison). Unfortunately those substrates exhibited relatively low sensitivity towards changes of refractive index (99.5 nm RIU^{-1}) and no SERS activity. Moreover, the procedure has very low reproducibility (see *Fig. 48D* for UV-Vis spectra obtained for 5 different samples). The cause is probably the same as previously – the uncontrolled self-entanglement of PVP molecules.

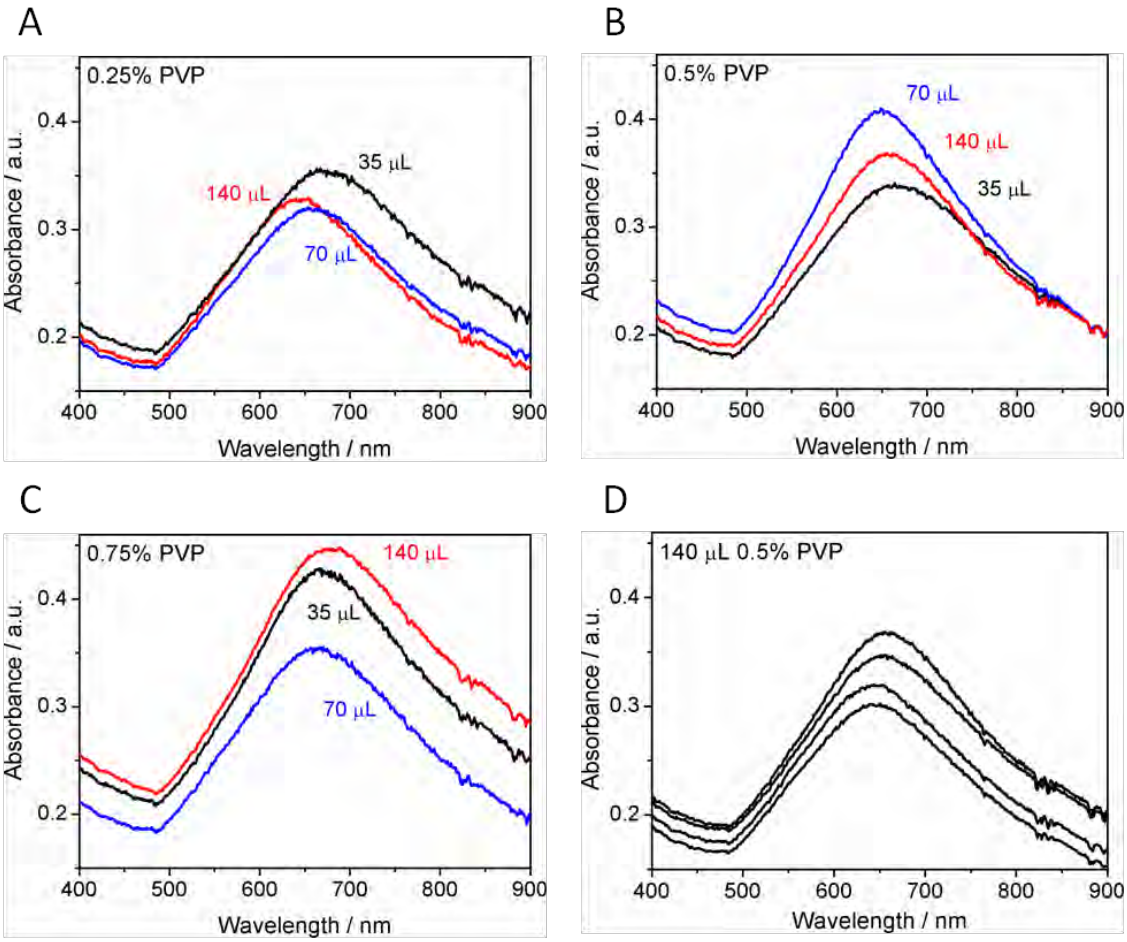

Fig. 48 Comparison of UV-Vis spectra of platforms obtained with 0.27 mM of gold salt, 0.09 mM of glucose in total volume of 6.2 mL of 0.1 M KNO_3 with addition of different amounts of freshly prepared solution of PVP: 0.25% (A), 0.5% (B), 0.75% (C) (electrodeposited for 50 scans at 50 mV s^{-1}, spectra recorded in air) along with reproducibility of UV-Vis spectra for samples obtained with addition of 140 µL of 0.5% PVP (D).

4.3 Reduction with iodide ions

The last attempt to obtain well-formed peaks at the UV-Vis spectra was inspired by the publication of El-Deab *et al.* [98] Authors added some iodide ions to the solution to obtain more homogeneous deposit. In our setup iodide ions were used as a reducing agent. Since the pK_a of the potassium iodide is very low also the pH of the solution was adjusted by adding 10 µL of 3 M HNO_3. The first step of the experiment was to fit the needed amount of iodide. In order to do that, three different amounts of KI solution were added to the initial solution (0.27 mM of $HAuCl_4$ in 0.1 M KNO_3 with addition of 10 µL of 3 M HNO_3). Final concentrations of iodide ions were 0.01 mM, 0.09 mM and 0.18 mM. Electrodeposition proceeded for 10 scans at potential scan rate of 10 mV s^{-1}. In *Fig. 49* voltammograms of 10th scan obtained for different amounts of iodide ions in the solution are presented. It is clearly visible that the onset potential of the gold reduction peak is shifted from about 0 V for 0.09 mM solution of KI to 0.27 V for 0.18 mM solution of KI. For 0.01 mM no reduction peak is visible in this region. Inset in *Fig. 49* shows UV-Vis spectra of respective samples. The narrowest peak (FWHM = 93 nm) was obtained for 0.18 mM solution of potassium iodide.

Next the proper electrochemical conditions were chosen from among 10 scans at 10 mV s^{-1}, 25 scans at 10 mV s^{-1} and 50 scans at 50 mV s^{-1}. The most appropriate substrate was obtained using 0.18 mM KI and 0.27 mM $HAuCl_4$ in total volume of 6.2 mL of 0.1 KNO_3 with addition of 10 µL of 3 M HNO_3. It was electrodeposited for 50 scans at 50 mV s^{-1}.

Resulting morphology of the deposit along with the UV-Vis spectra are depicted in *Fig. 50*. The performed RIS test resulted in a very low value – 41 nm RIU^{-1}. No SERS activity was observed.

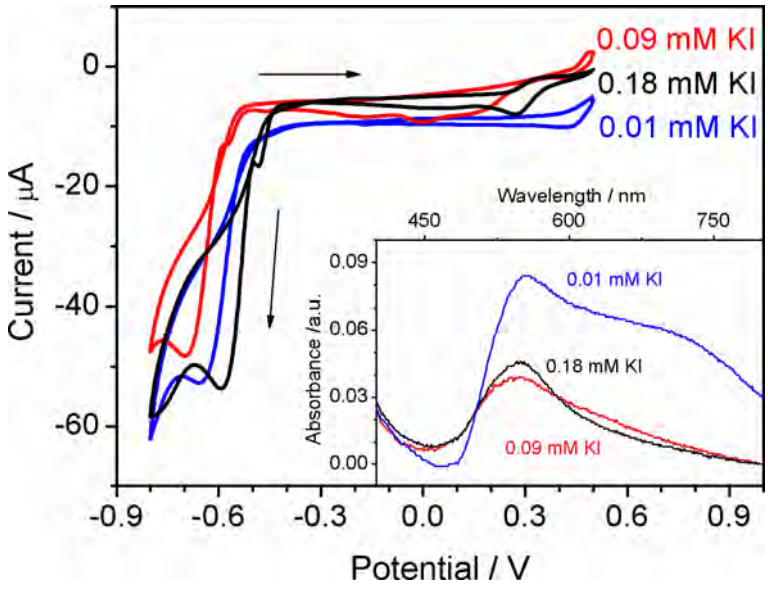

Fig. 49 10th scans of CV at potential scan rate of 10 mV s^{-1} performed from solutions containing 0.27 mM solution of HAuCl4 in 0.1 M KNO3 with addition of 10 µL of 3 M HNO3 and different concentrations of KI – 0.01 mM, 0.09 mM and 0.18 mM; inset shows UV-Vis spectra of respective samples measured in air.

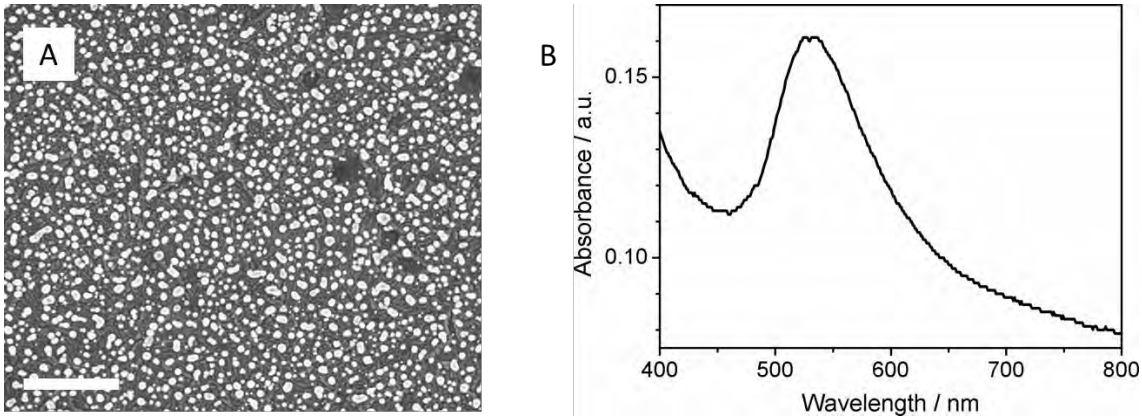

Fig. 50 Morphology (A) and UV-Vis spectrum (B) of platform fabricated using 0.18 mM KI, 0.27 mM $HAuCl_4$, 10 µL of 3 M HNO_3 in total volume of 6.2 mL of 0.1 KNO_3, electrodeposited for 50 scans at 50 mV s^{-1} (scale bar on SEM image represents 500 nm, UV-Vis spectrum recorded in air).

4.4 Summary and conclusions

This chapter of the dissertation was dedicated to the use of cyclic voltammetry to obtain gold-based plasmonic platforms. To evaluate obtained substrates scanning electron microscopy, UV-Vis spectroscopy and/or surface enhanced Raman spectroscopy were used.

The experiments showed that the range of potentials used influences the morphology of obtained deposits. The projected radii of particles as well as the surface coverage decrease with the increase of the potential scan rate. Also they increase with the increase of the number of performed scans of the CV.

In case of the AuNPs electrodeposition three bath compositions resulted in platforms with promising plasmonic properties. AuCitNPs platform was fabricated in the range of potentials 0.5 – -0.8 V for 25 scans at 10 mV s^{-1}. The solution contained 0.27 mM of chloroauric acid and 0.09 mM of trisodium citrate in total volume of 6.2 mL of 0.1 M KNO_3. Calculated SERS enhancement factor value was 5×10^7. AuGluNPs platform was electrodeposited at the same electrochemical conditions from the solution containing 0.27 mM of $HAuCl_4$ and 0.09 mM of glucose in total volume of 6.2 mL of 0.1 M KNO_3. Calculated SERS enhancement factor was 1×10^7. For both aforementioned platforms it was impossible to establish refractive index sensitivity because of a very broad and irreproducible resonance peaks on the UV-Vis spectrum. Opposite situation occurred for the AuINPs electrodeposited (50 scans at 50 mV s^{-1}) from 0.27 mM solution of $HAuCl_4$ and 0.18 mM solution of KI with the addition of 10 µL of 3 M HNO_3 in total volume of 6.2 mL of 0.1 M KNO_3. The AuINPs platforms were inactive in SERS experiments, but well established plasmon resonance peak allowed to measure refractive index sensitivity which was 41 nm RIU^{-1}.

Chapter 5

Applications of obtained plasmonic-active platforms

Previous two chapters of the dissertation were dedicated to the preparation process of plasmonic-active platforms. This part will present possible applications of obtained platforms.

To show the applicability for surface enhanced Raman spectroscopy, two platforms were chosen – AgCitNPs and AuCitNPs. They were used to detect neurotransmitters.

For use in LSPR AgCitNPs were chosen. They were suitable to study the dielectric properties of bacteria, binding of lectins to sugars and detection of bacteriophages using specific antibodies attached to the platform.

4.1 Surface Enhanced Raman Spectroscopy (SERS)

4.1.1 SERS of neurotransmitters

Neurotransmitters are chemical moieties responsible for signaling between cells of the nervous system, muscles and glands. They convert chemical signals into electrical ones. When the membrane of the nervous cell is depolarized,

molecules of the neurotransmitter are released and can diffuse to the neighboring cell. There they are binding to the specific receptors thus changing the polarization of the cell membrane. If the depolarization is strong enough (so the number of attached neurotransmitters is sufficient), the signal is propagated along the cell to its other end.

Neurotransmitters were discovered in 1921 by Otto Loevi, who showed that neurons are communicating by releasing chemicals (1936 Nobel Prize in Physiology or Medicine [186]). The main division of neurotransmitters includes amino acids (e.g. glutamate, D-serine, γ-aminobutyric acid (GABA), glycine), peptides (e.g. somatostatine, opioid peptides), monoamines (e.g. dopamine, epinephrine (adrenaline), serotonin), gasotransmitters (e.g. nitric oxide, carbon monoxide), ions (e.g. zinc ion) and others (e.g. acetylcholine, adenosine). Disturbed levels of neurotransmitters are connected with many disorders, like Alzheimer's [187] or Parkinson's disease [188], depression [189], insomnia [190], addictions [191] and others. [192]

For detection of neurotransmitters at a physiological level, SERS was considered a well suited method. To date their spectra have been recorded on colloidal silver nanoparticles [193], rough silver electrodes [194] and polymer-coated silver electrodes. [195]

In this study detection of dopamine, epinephrine, acetylcholine and choline (precursor of acetylcholine) was shown. Moreover, comparison between fabricated AgCitNPs platform and commercially available Klarite™ platform was done.

AgCitNPs platforms were electrodeposited accordingly to the description in *Section 3.3*. SERS measurements were carried out on dried samples using a Renishaw inVia Raman system described in *Section 2.1.4*. The normal Raman spectra were acquired for 20 min. For SERS experiments the spectra were acquired for 90 s with the laser emitting at 785 nm. The power measured at the sample was 5 mW for experiments with 4-ATP and 10 mW for

neurotransmitters and choline. When presenting the results, the spectra have been normalized by the laser power and the collection times. Neurotransmitters (all purchased in Sigma Aldrich) were adsorbed on the surface of AgCitNPs for 8 hours from respective solutions: 7×10^{-4} M for epinephrine, 4×10^{-6} M for acetylcholine, 2×10^{-6} M for choline and 1×10^{-7} M for dopamine. Accumulation time was 90 s. Physiologically relevant concentrations are in the same range for acetylcholine [196], dopamine [197] and choline. [198] Adsorption of choline on Klarite™ platform proceeded for 8 hours from 1 M solution (the lowest concentration possible to measure) and the accumulation time was 15 min.

In the first step the comparison between AgCitNPs platform and Klarite™ platform was performed. For that purpose 4-ATP was adsorbed on both platforms from 10^{-6} M solution (8 hours). Recorded spectra are presented in *Fig. 51*.

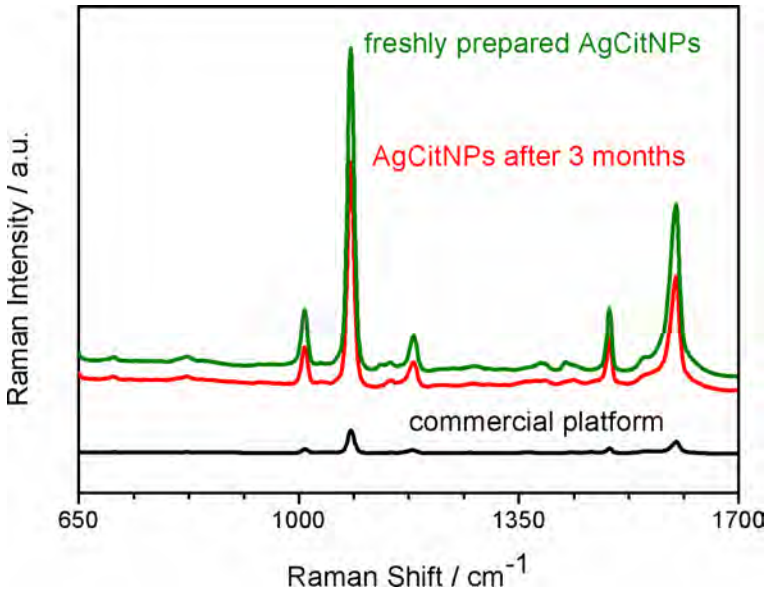

Fig. 51 Comparison of SERS spectra obtained from 10^{-6} M solution of 4-ATP on commercial platform (Klarite™, black spectrum) and on AgCitNPs both, freshly prepared (green spectrum) and after 3 months of storage (red spectrum).

It was calculated that Klarite™ provides three orders of magnitude lower signal than AgCitNPs. Moreover, its stability decreases rapidly within hours (results not shown) while AgCitNPs platforms lose about 15% of signal after 3 months of storage on shelf under ambient conditions (red spectrum in *Fig. 51*).

Since for SERS platforms reproducibility and repeatability are crucial factors, the correlation coefficient was calculated. In order to do that spectra of 4-ATP were recorded on 25 different spots of a single AgCitNPs platform. 25 different platforms were used (5 batches, 5 different platforms from each). At first, the background subtraction, the Savitzky-Golay smoothing (window size of 39 date points with second order polynomial) and the normalization of all spectra was done. Next, correlation coefficients between all nonidentical spectral pairs (i≠j) in the same data set were determined from the equation 13:

$$P_{i,j} = \frac{\sum_{k=1}^{W}(I_i(k)-\bar{I}_i)(I_j(k)-\bar{I}_j)}{\sigma_i \sigma_j}, \qquad (13)$$

where i, j is the index of the spectra in the data matrix, k is the wave number index of the individual spectra, I is the spectral intensity, W is the spectral range, and σ_i is the standard deviation of the spectrum. Once the correlation coefficients $P_{i,j}$ are calculated, the average of the off-diagonal correlation coefficients (Γ) can be determined:

$$\Gamma \equiv \frac{2\sum_{i=1}^{N}\sum_{j=1}^{N} P_{i,j}}{N(N-1)} \qquad (14)$$

Γ defined that way is a very useful parameter for quantitative assessment of spectral reproducibility. Γ varies between 0 and 1, where 1 is the case of identical spectra and 0 the case of completely uncorrelated spectra. In case of AgCitNPs platforms the cross-correlation coefficient Γ was as high as 0.96 (the same protocol used for Klarite™ platforms resulted in Γ in a range of 0.85 – 0.9). Exemplary SERS spectra of p-ATP from four different measurements on the same platform are presented in *Fig. 52a*. In each tested region, the same modes appear with very high reproducibility with only a slight variation in amplitude for some of the higher wavenumber modes. *Fig. 52b* shows the normalized second derivatives of the spectra. The almost

complete overlap in features observed in the second derivative spectra indicates that the differences in the SERS spectra are mainly due to baseline variations and not due to variations in peak positions or in relative peak intensities.

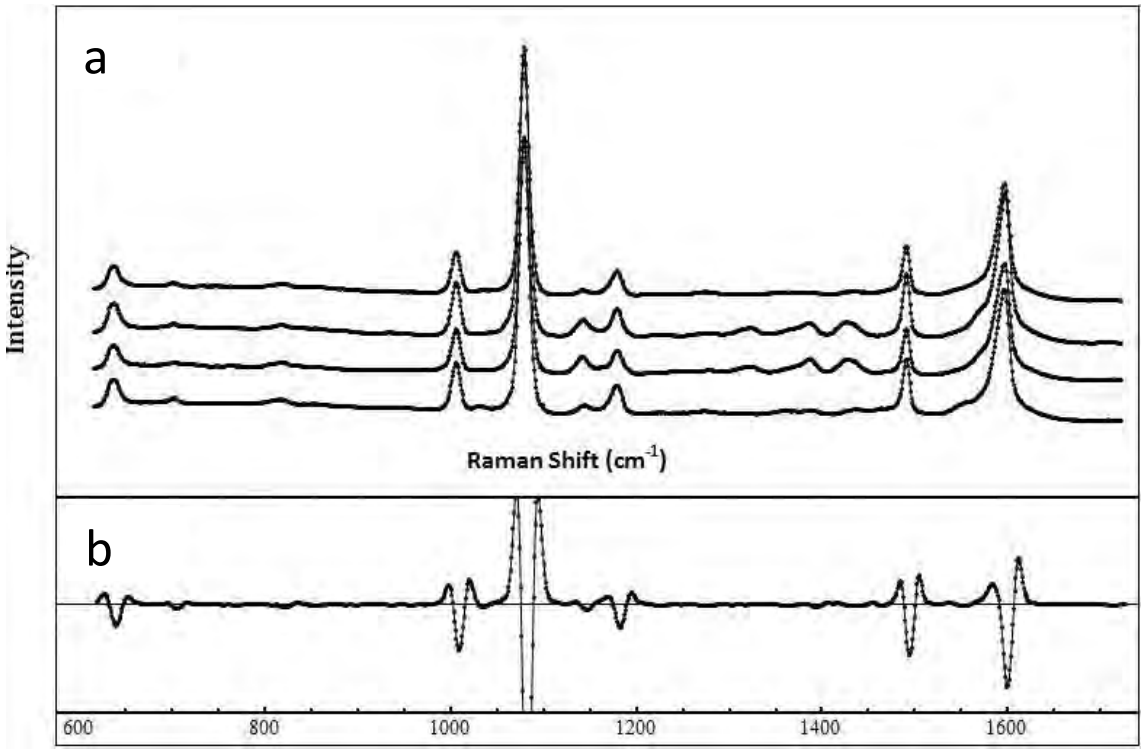

Fig. 52 SERS spectra of p-ATP from four different measurements on the same AgCitNPs platform (a). (b) second derivative of SERS spectra with calculated cross-correlation coefficient of 0.96.

Detection of neurotransmitters on Klarite™ platforms was impossible even after adsorption from 1 M solution with 15 min of accumulation of the signal. Unlike AgCitNPs, where the signal is strong and bands are well developed after accumulation time as short as 90 s (*Fig. 53b*). Spectrum "*a*" in *Fig. 53* shows the normal Raman spectrum obtained for 10^{-3} M solution of choline. Spectrum "*b*" was obtained after adsorption from 2×10^{-6} M solution of choline. The most characteristic bands can be found at 714 cm^{-1} and 764 cm^{-1} (symmetric stretching vibrations of the four C-N bonds of the quaternary ammonium group for the gauche and trans conformations of the O-C-C-N^+ backbone,

respectively) and at 954 cm^{-1} (asymmetric stretching vibrations of the C-N bonds). [199]

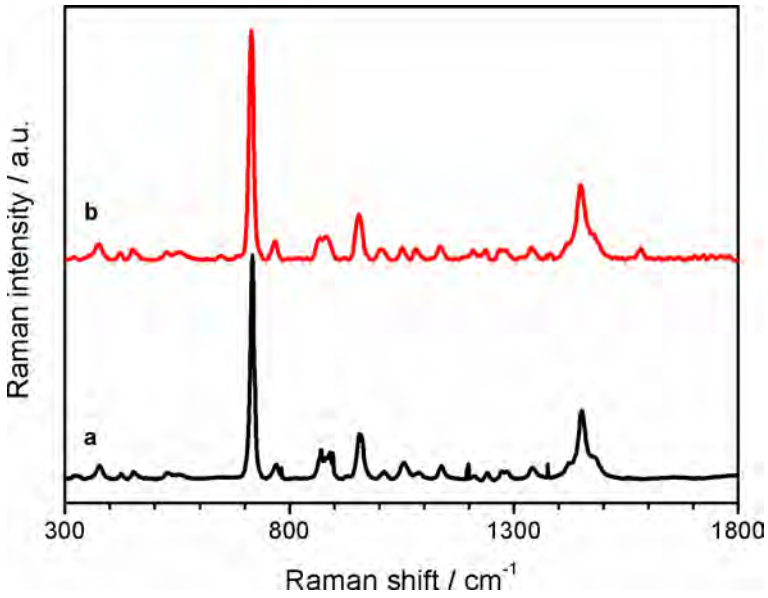

Fig. 53 a – normal Raman spectrum of 10^{-3} M solution of choline; b – SERS spectrum of 10^{-6} M solution of choline recorded on AgCitNPs.

Furthermore, SERS spectra of epinephrine, acetylcholine and dopamine in physiologically relevant concentrations were recorded on AgCitNPs platforms. All spectra are presented in *Fig. 54 a*, *b* and *c*, respectively.

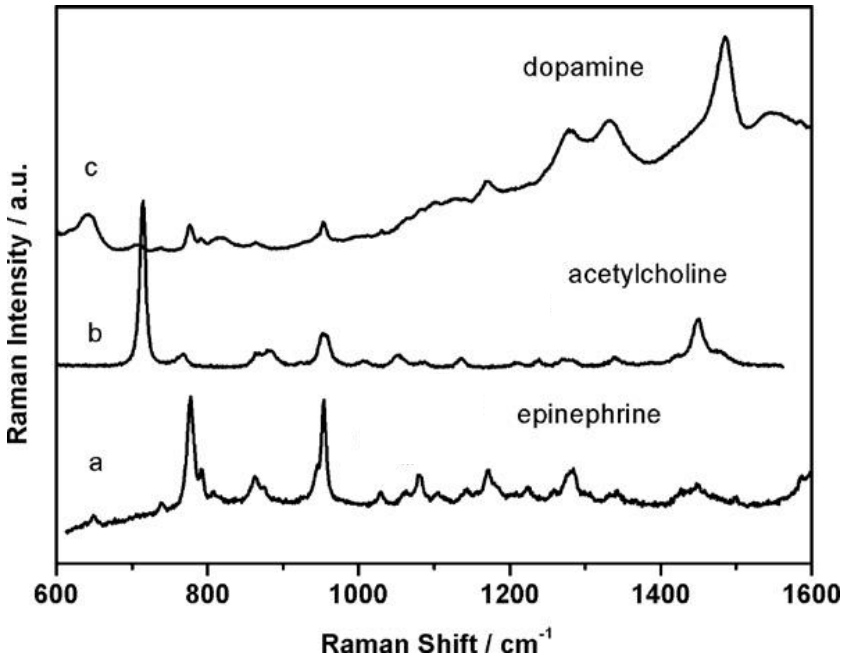

Fig. 54 SERS spectra of (a) epinephrine adsorbed onto AgCitNPs surface from 7×10^{-4} M aqueous solution, (b) acetylcholine adsorbed onto AgCitNPs surface from 4×10^{-6} M aqueous solution, (c) dopamine adsorbed onto AgCitNPs surface from its 1×10^{-7} M aqueous solution.

To summarize, AgCitNPs platforms are better than commercially available ones (Klarite™) in terms of enhancement of the signal, reproducibility or stability. Well developed, distinct spectra of neurotransmitters at physiologically relevant levels were recorded.

4.1.2 Detection of choline-like particles in a blood serum

The choline (*Fig. 55*) fits the original definition of a *vitamine* – an amine which can be synthesized in human organisms only in small amounts and has to be consumed in the diet. [200] In the body choline plays many roles – as a part of structural (e.g. glycerophosphorylcholine) or signaling membrane phospholipids (e.g. sphingomyelin), as a precursor for betaine (which is the donor of methyl groups for consecutive processes) and acetylcholine (the

neurotransmitter). It was proven on animals that choline nutrition is crucial since the fetal life and has life-long consequences, e.g. can affect cognitive and memory functions [200] and influence the work of the liver, kidneys, heart. [201] Nowadays the choline level in the whole blood and in plasma has been proposed as a biomarker for acute coronary syndromes. [202] Furthermore, the level of total choline-containing compounds is used as a biomarker for tumours, especially for breast and prostate cancer. [203, 204]

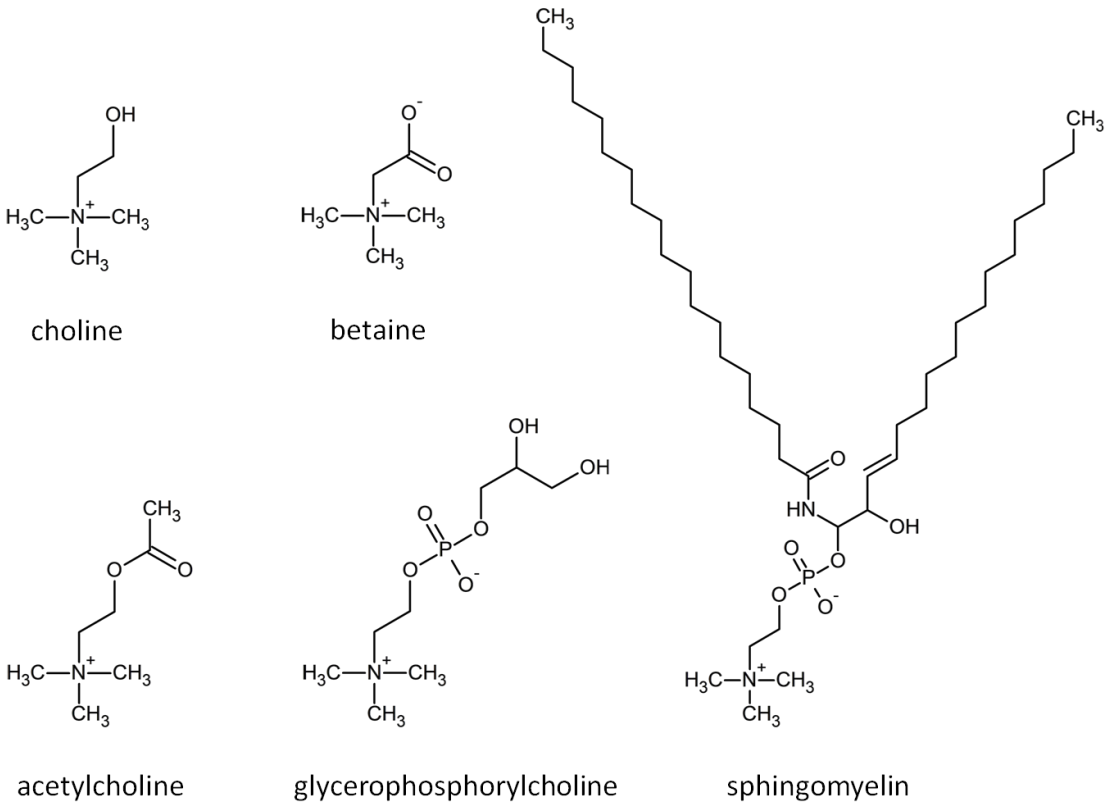

Fig. 55 Structures of choline and choline-like molecules.

Since its discovery in 1862, choline was the subject of intense research. [201] The first Raman spectrum of free choline was published in 1943 by Edsall. [205] It is known that usually choline adsorbs to the negatively charged surface with its positively charged head. Surprisingly, even though the role of choline in living organisms is quite well established, there are not so many reports about experiments with choline involving Raman spectroscopy. Possibly, it is because the preparation of samples containing choline and choline-like

compounds is very fastidious. To establish the real level of free choline in e.g., whole blood or plasma samples, it is necessary to inactivate all enzymes which could turn choline metabolites into free choline (e.g. with special kit [206] or acetonitrile [207]). It was shown that in blood serum incubated in room temperature the level of choline increased sevenfold within 72 h. [207]

Examples of measuring levels of choline in natural samples using surface enhanced Raman spectroscopy (SERS) are described e.g. by Yan and Reinhard [208] and Huang *et al.* [209]

The study presented in this dissertation attempts to determine the level of choline and choline-like compounds in human plasma using SERS on AuCitNPs platform.

AuCitNPs were electrodeposited accordingly to the description in *Section 3.3*. SERS measurements were carried out on wet samples using a Renishaw inVia Raman system equipped with a 300 mW diode laser emitting at 785 nm (described in *Section 2.1.4*). The normal Raman spectrum of choline was acquired for 20 min. For SERS experiments the spectra were acquired for 90 s with the laser power measured at the sample being 10 mW. Prior to SERS measurements AuCitNPs platforms were immersed into adequate solutions for 8 hours. The calibration curve for choline (Sigma Aldrich) was prepared in the range of concentrations from 10^{-6} M to 10^{-3} M. All solutions were made in 0.9% NaCl. Each calibration point was measured 3 times. The whole blood sample from a healthy patient was provided by Regional Center of Blood Donoring. The blood was centrifuged within an hour after collection in 3 kDa filter tube at 3000 rpm for 15 minutes. Next, it was heated to 70°C for 30 min to inhibit the enzymes, cooled and stored in fridge prior to use.

Fig. 56 shows normal Raman spectrum of choline powder. The highest band, at around 720 cm^{-1} (marked with a star), is assigned to $N\text{-}C_4$ tetrahedrally symmetric stretching vibration. [57] The intensity of this band was taken as an indicator of the level of choline and choline-like compounds in the sample.

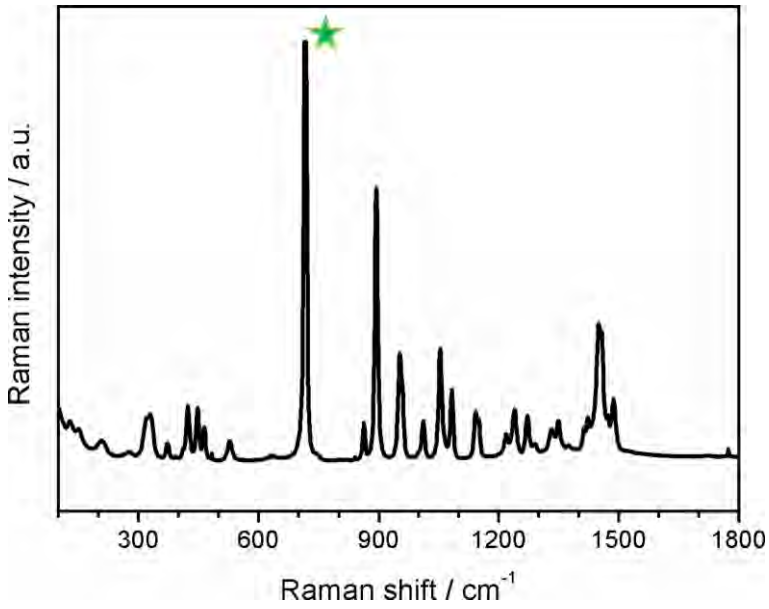

Fig. 56 Normal Raman spectrum of choline powder

Calibration was performed for four concentrations of choline – 10^{-6}, 5×10^{-5}, 10^{-4} and 10^{-3} M. For the lowest level no distinguishable band was observed around 715 – 720 cm^{-1}. *Fig. 57* depicts an exemplary SERS spectrum obtained at AuCitNPs platform from 10^{-3} and 5×10^{-5} M solutions. The choline band was marked with a star. The inset shows calibration curve calculated for the integrated area of the N-C_4 band.

In the next step it was checked whether it is possible to obtain SERS spectrum of blood plasma on AuCitNPs and whether the 715 cm^{-1} choline band is visible. Resulting spectrum is shown on *Fig. 58*. As can be seen many bands are distinguishable and even though the background level is quite high (spectra are shown without background subtraction). The band around 715 cm^{-1} is also visible but it is hard to conclude if it is a single peak or not. Additionally, during the calibration it was impossible to obtain choline spectrum at physiological concentration (in the range of 10^{-6} M [198]). Consequently, one can conclude that the detectable N-C_4 band comes not only from choline but also from choline-like compounds like betaine or acetylcholine.

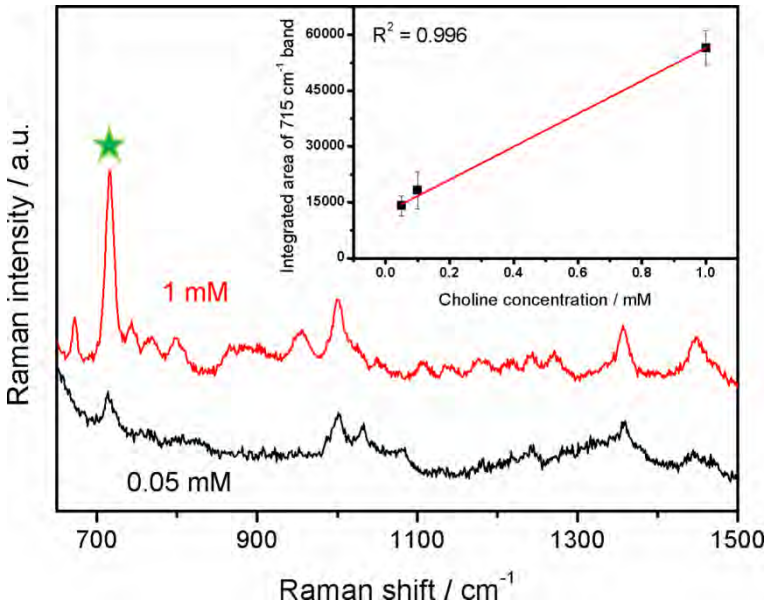

Fig. 57 Examples of SERS spectra obtained for 10^{-3} M and 5×10^{-5} M solutions of choline on AuCitNPs platforms; inset shows calibration curve obtained for the integrated area of the 715 cm^{-1} band.

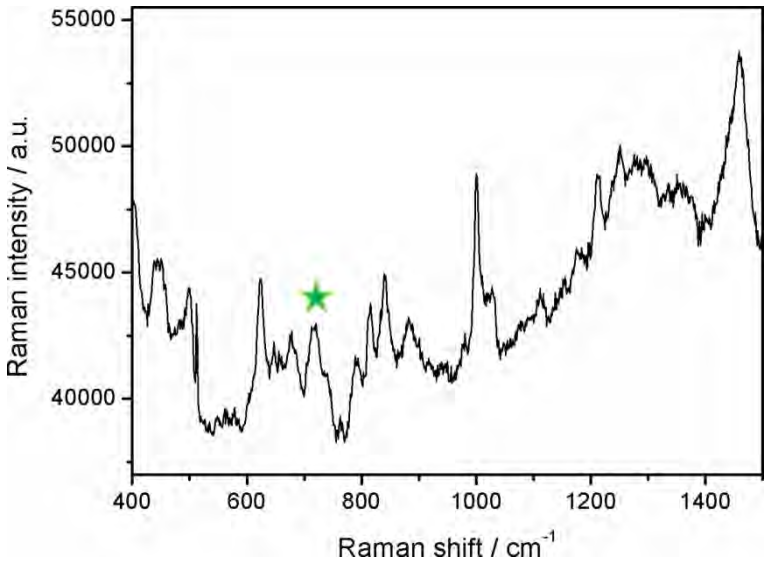

Fig. 58 SERS spectrum of human blood plasma obtained on AuCitNPs; the star indicates the 715 cm^{-1} band of choline.

In order to check whether the star-marked band on *Fig. 58* is from N-C_4 vibration, 1 mmole of choline was added to the diluted blood plasma (1:10 with 0.9% NaCl). The dilution was made to decrease the background level and diminish the input from choline-like molecules. Next the area of obtained 715 cm^{-1} band (marked with a star in *Fig. 59*) was integrated and compared with the calibration curve presented in inset of *Fig. 57*. Resulting level was estimated to be 0.6 mM. This underestimation shows that AuCitNPs are not suitable for quantitative measurements of the level of choline in blood samples.

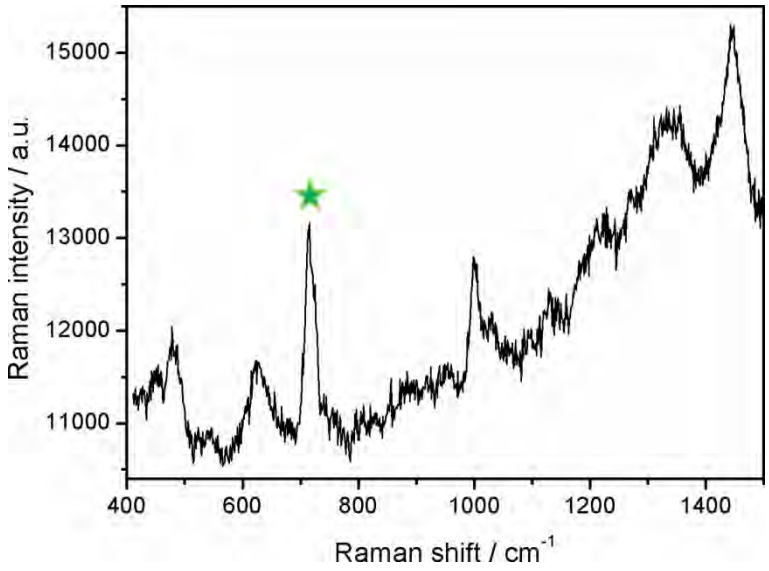

Fig. 59 SERS spectrum of diluted blood plasma with 1 mmole of choline added; star indicates the choline band at 715 cm^{-1}.

SERS spectrum of natural human blood plasma was recorded on AuCitNPs platform. It was possible to distinguish the N-C_4 tetrahedrally symmetric stretching vibration band characteristic for choline and choline-like compounds. Unfortunately it was impossible to measure quantitatively the concentration of choline in the sample.

4.2 Localized Surface Plasmon Resonance (LSPR)

4.2.1 Activity of platforms towards changing concentration of Bovine Serum Albumin

Bovine Serum Albumin (BSA) is a model protein used in biochemistry and molecular biology. It is used in immunoassays to prevent non-specific adsorption of analytes [210], in stabilization of enzymes [211], in cells and microbial cultures. [212] It is neutral and does not exhibit its own enzymatic activity. In standard procedures it is used as a negative control for biosensors. For the purpose of this study BSA was used as a standard biomolecule which accumulation on the surface of the sensing platform was monitored.

AgCitNPs were electrodeposited as it was described previously in *Section 3.3*. The UV-Vis measurements of dried samples were performed. The 100 µL droplets of water solutions of BSA (Sigma Aldrich) were applied on the surface of AgNPs platform, left for 30 min and dried with a stream of nitrogen. After a measurement a droplet of more concentrated solution was applied on the same platform and the procedure was repeated. The range of tested concentrations was from 10^{-12} M to 10^{-6} M.

Fig. 60 shows the peak of interest of native AgCitNPs sample and after applying 10^{-10} M, 10^{-8} M and 10^{-6} M solutions of BSA. In *Fig. 61* it can be seen how the maximum of the resonance peak shifts upon applying additional amount of the analyte. It is in agreement with the intuition that for very small amounts of the analyte the signal is not changing. Also, when the sensing surface is “saturated”, the resonance wavelength does not change and the system reaches the second plateau. This can be clearly seen with the fitting line on the *Fig. 61A* (fitted with the Hill function with the $R^2 = 0.998$). *Fig. 61 B* shows more precisely the inflection point.

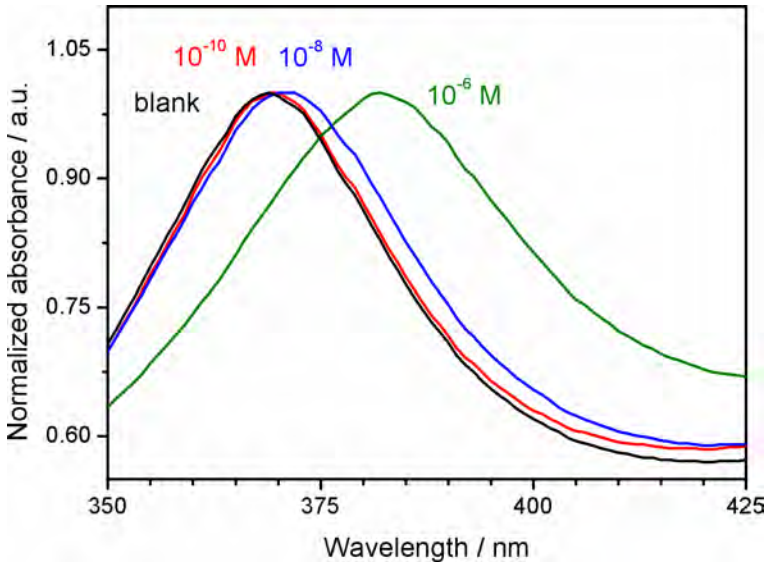

Fig. 60 UV-Vis spectra of AgCitNPs obtained after applying 10^{-6} M, 10^{-8} M and 10^{-10} M solutions of BSA (curves green, blue and red, respectively) with respect to the native AgCitNPs platform (black curve) measured in air.

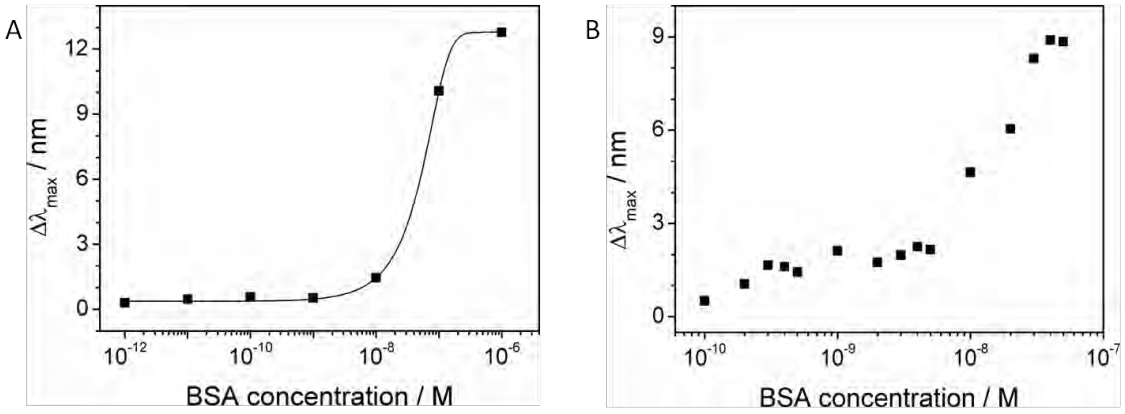

Fig. 61 Shift of the resonance wavelength upon increased BSA concentration applied onto the surface of the AgCitNPs platform; A – concentrations range from 10^{-12} M to 10^{-6} M with the line of trend; B – concentrations range from 10^{-10} M to 10^{-7} M to show the inflection point

The accumulation of BSA on the surface of the AgCitNPs platform was monitored. The observed trend fits the Hill function which is a classical concentration-response curve. [213] These results can be seen as a proof of concept that the AgCitNPs LSPR platform can be used for biomolecular detection.

4.2.2 Detection of binding between lectins and sugars

Lectins are highly specific carbohydrate-binding proteins. They are present in all living organisms – viruses, plants and animals. [214] They are responsible for a broad range of biological processes – from fertility and interactions of cells in the immune systems, through handling and removing of glycoproteins from the system to agglutination of red blood cells. [215] Their role in cell recognition, especially influence on adhesion of the infectious agents to host cells, has to be emphasized. [216] First described lectin was ricin, isolated from castor plant by Peter H. Stillmark in 1888. [217] Concavalin A (ConA) was the first lectin purified and commercialized. It is isolated from a jack bean and nowadays is widely used as a model lectin.

Lectins and carbohydrates form a non-covalent, reversible and very specific bond. The binding site is usually a shallow pocket with numerous hydroxyl groups creating a network of weak hydrogen bonds between lectin and bound molecule (see *Fig. 62A*). [214] The main criterion in the lectins classification is the monosaccharide ligand toward which they exhibit the highest affinity. Five classes are distinguished: mannose-, N-acetylglucosamine-, fucose-, galactose/N-acetylgalactosamine- and N-acetylneuraminic acid-specific lectins. All these sugars (except fucose) have the D-configuration.

In the literature one can find several reports about studying lectin-carbohydrates interaction using plasmonic techniques. SPR and LSPR experiments are performed mostly on gold-based substrates. [218-222] Only the group of van Duyne compared results of binding of ConA to mannose obtained in SPR and LSPR experiments, where LSPR was performed on AgNPs

fabricated by a nanosphere litography. [223] Nevertheless, all used systems are quite complicated, e.g. Ogiso *et al.* used dendrimer-coated colloidal gold (where carbohydrates are bound to dendrimers) [222] and Endo *et al.* created a developed surface by covering silica particles with a layer of gold. [220] Work of Bhattarai *et al.* [219] and Bellapadrona *et al.* [218] required synthesis of modified carbohydrates which would bind to the surface of the sensor.

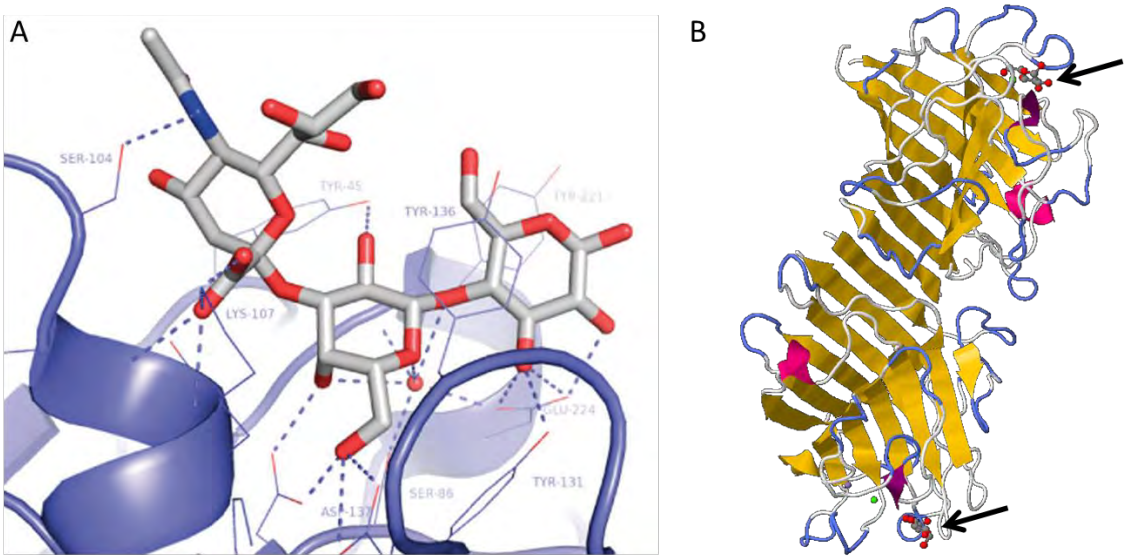

Fig. 62 A – The binding site of *Maackia amurensis* lectin complexed with sialyllactose; occurring interactions are shown with dashed lines (source: [214]); B – structure of *Lens culinaris* lectin in complex with alpha-D-glucopyranose (bound carbohydrate molecules are indicated with black arrows; source: [224] available from RCSB Protein Data Bank)

In this study carbohydrates were immobilized in graphene-based layers applied on top of AgCitNPs. Graphene oxide (GO) or reduced graphene oxide (rGO) were applied via spin-coating. Carbohydrates were immobilized during simple soaking in the proper water solution of the sugar. The binding between *Lens culinaris* (LC) and *Maackia amurensis* (MA) lectins with adsorbed carbohydrates was examined via LSPR. LC lectin is obtained from lentil seeds. It is a glucose binding protein (has also smaller affinity to mannose). It exhibits the isoelectric point (pI) at pH of 7.6 – 8.4. Its molecular weight is 50 kDa. [181]

The structure of LC lectin is presented in Fig. 62 B. MA lectin is obtained from Amur tree. It binds to N-acetylneuraminic acid (sialic acid) and galactose residues. Its molecular weight is 130 kDa and it exhibits a pI at pH of 4.7. [181]

The AgCitNPs platforms were electrodeposited according to the protocol described in *Section 3.3*. Graphene oxide was obtained in modified Hummer's method according to the procedure described by Das *et al.* [225] Half milligram (0.5 mg) of the synthesized GO was dispersed in 1 mL of acetonitrile and exfoliated through ultrasonication for 3 h. This suspension of GO was used as a stock suspension in subsequent experiments. Reduced graphene oxide (rGO) was obtained by refluxing GO in hydrazine hydrate according to the procedure described by Yang *et al.* [226] Half milligram (0.5 mg) of the synthesized rGO was dispersed in 1 mL of acetonitrile and exfoliated through ultrasonication for 3 h. This suspension of rGO was used as a stock suspension in subsequent experiments.

To assure good adhesion of carbohydrates the layer of GO or rGO was applied onto the AgCitNPs via spin-coating (2000 rpm for 30 sec). 25 µL of the proper stock solution was used to obtain one layer. In the next step carbohydrate was adsorbed from 100 mM water solution for 4 hours. Afterwards, platforms were rinsed carefully with deionized water and used immediately.

In order to observe binding of lectins to sugars a droplet (30 µL) of given solution of lectin was applied onto the prepared surface and left for 90 minutes, washed gently with an appropriate buffer solution and measured in the same buffer. 0.1 M phosphate buffer of pH 6.8 or 7.2 was used for LC and MA, respectively (according to recommendation of lectins` producer – Sigma Aldrich).

In the first step the AgCitNPs platforms were covered with different number of GO layers. The uniformity of applied layers was checked with SERS measurements. As it was predicted, the intensity of GO characteristic band at

1600 cm^{-1} (*Fig. 63A*) was proportional to the number of applied layers (*Fig. 63B*).

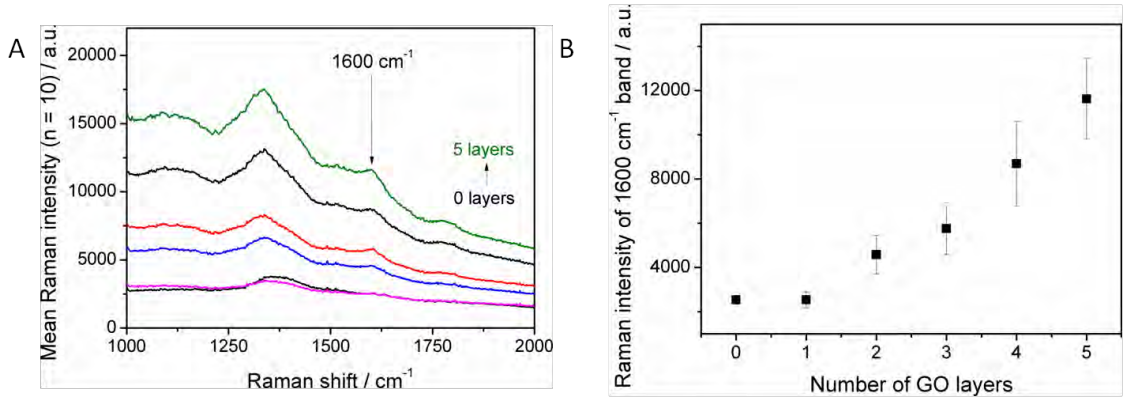

Fig. 63 A – SERS spectra obtained for different number of GO layers on AgCitNPs platform (laser wavelength: 785 nm, acquisition time: 5 sec, laser power: 10 mW); B – correlation between the intensity of the 1600 cm^{-1} band of GO and the number of layers applied

In the next step of the experiment the comparison between binding of LC and MA to the carbohydrates was done. As it was described before, LC is a glucose and mannose binding lectin while MA should not bind to those carbohydrates and should act as a negative control. For that purpose comparison of changes in the resonance wavelength shifts was made depending on the adsorption of lectins on bare GO and GO with sugar. Results are presented in *Fig. 64*. In both systems (with glucose (glu) and with mannose (man)) the responses coming from different lectins were very similar. In case of LC lectin addition of sugar to the system caused an increase of obtained resonance shift. Interestingly, for MA lectin addition of sugar caused a decrease of the shift so the specificity of the binding was improved. However, the shift obtained for MA lectin adsorbed on bare GO is quite big. It can be caused by interactions between hydroxyl and carboxylic groups of GO with the protein.

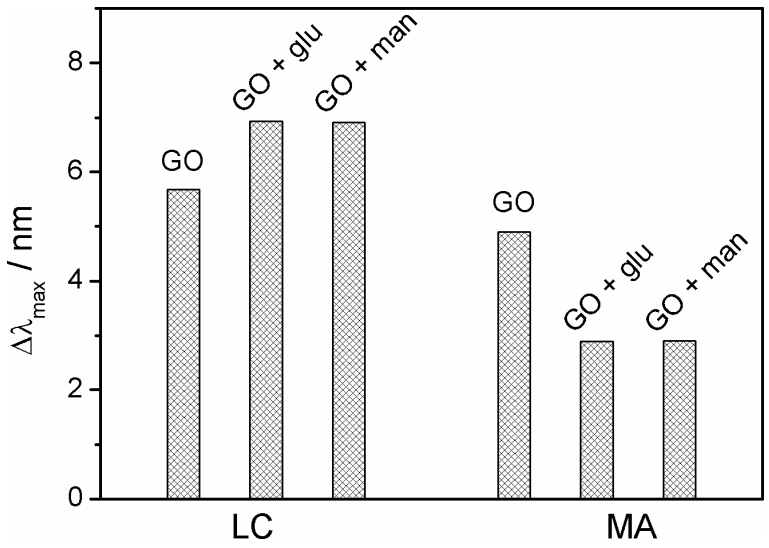

Fig. 64 Differences in obtained shifts of the resonance wavelength after adsorption of LC or MA lectins on the platforms covered with GO (bare or with adsorbed glucose (glu) or mannose (man)).

Since the binding between LC lectin and adsorbed sugars was confirmed, the response of the system upon change of the concentration of the lectin was tested (*Fig. 65A*). Different concentrations of LC lectin (from 1 µg mL^{-1} to 1000 µg mL^{-1}, which corresponds to range from 20 nM to 20 µM) were adsorbed on the GO-covered platforms with adsorbed glucose (100 mM). The profile of the shift of resonance wavelength fits the one presented in *Fig. 60* for model molecule of BSA. The amount of the analyte determines how big shift is observed. Also, the influence of the amount of carbohydrate (glucose or mannose) was examined by immersing platforms covered with GO in different solutions of the adequate sugar. Concentrations varied from 1 to 100 mM (the zero point was measured after immersion into deionised water). After 4 hours of sugar adsorption platforms were washed gently with deionised water and used to bind LC lectin (500 µg mL^{-1} solution). A significant shift obtained for system without any sugar suggests strong interactions between GO and LC lectin. Larger shifts obtained for glucose (red bars in *Fig. 65B*) indicates the creation of stronger bonds between LC and glucose than between LC and mannose. As a result the highest resonance wavelength shift was obtained when 500 µg mL^{-1} LC lectin was adsorbed on GO-covered AgCitNPs platform with 100 mM glucose adsorbed.

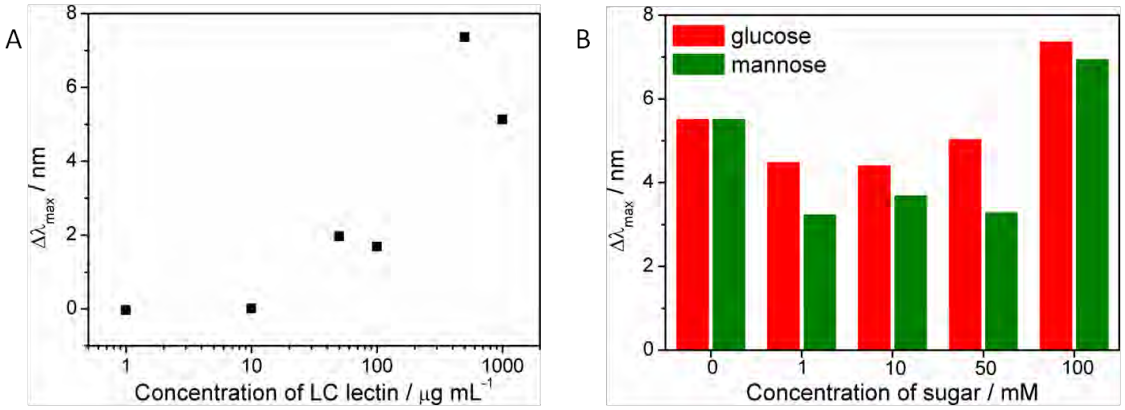

Fig. 65 A – Shift of the resonance wavelength upon changes of concentration of LC lectin adsorbed on the AgCitNPs platform covered with GO and 100 mM of glucose; B – Comparison of shifts of the resonance wavelength obtained for 500 μg mL^{-1} solution of LC lectin adsorbed on the AgCitNPs platform covered with GO and different amounts of sugars.

To eliminate strong interactions between GO and lectins the system was changed. Instead of GO, the reduced GO (rGO) was used. In the first step interactions between lectins and above-mentioned types of graphene used were compared (*Fig. 66*). As can be seen reduction of GO eliminated almost completely nonspecific interactions between graphene-based coverage and lectins.

Subsequently tests with binding of 500 μg mL^{-1} LC lectin to different adsorbed sugars were performed. Additionally the 3rd sugar was added to the comparison – a disaccharide, lactose, which should not interact specifically with either of the lectins (second negative control). On the basis of the results presented in *Fig 67A* one can conclude that the non-specific interactions (LC-lactose) cause approximately a 3 nm shift in the resonant wavelength.

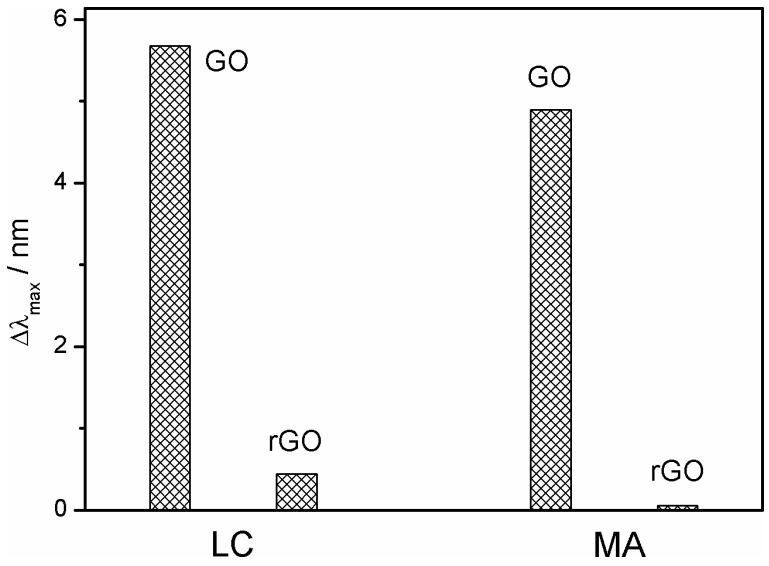

Fig. 66 Comparison of shifts of the resonance wavelength of AgCit(T)NPs obtained as a result of interactions between LC and MA lectins with GO and rGO.

The strongest effect is observed for the adsorption of LC lectin on 100 mM glucose. As a confirmation, additional experiment was carried out. The binding of LC and MA lectins (both in concentration 500 μg mL^{-1}) to 100 mM sugars adsorbed on rGO was compared, as shown in *Fig 67B*. The most specific response comes from binding of LC with glucose. Surprisingly, there is no clear dependence between amount of adsorbed glucose and the height of the resonance shift. Probably it is caused by interactions occurring between rGO and the carbohydrate. This phenomenon can also be the cause of some non-specific interactions of MA lectin with glucose and mannose. Interactions of both lectins with lactose result in very similar shift of ~3 nm suggesting lack of specific binding.

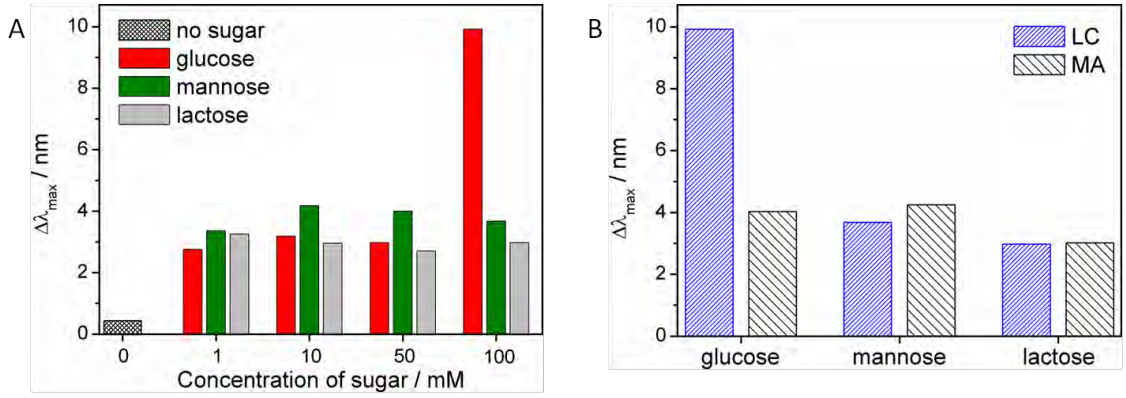

Fig. 67 Comparison of binding of 500 µg mL^{-1} lectins to different sugars adsorbed on rGO layer at AgCit(T)NPs: A – differences in binding of LC lectin resulting from different concentrations of adsorbed sugars, B – differences between LC and MA lectins adsorbed on 100 mM sugars.

The last experiment illustrates the shifts of the resonance wavelength as a function of the LC concentration (*Fig. 68*). For that purpose, the rGO-covered AgCitNPs with adsorbed glucose were used as a sensing platform. The trend observed is the same as in the case of GO-covered AgCitNPs – the signal starts to grow significantly above 100 µg mL^{-1} of LC lectin, reaches peak at 500 µg mL^{-1} and drops at the highest concentration. The reason of dropping is unknown. Probably it is caused by damping the plasmon resonance by thick layer of lectins.

In this section the specific and nonspecific interactions between lectins and sugars were investigated using the prepared AgCitNPs platforms. Silver nanoparticles were covered with graphene-based material in oxidized or reduced form acting as a matrix for sugar adsorption. On GO the non-specific binding between GO and lectins caused a large shift in the resonance peak, which made these platforms unsuitable for studies of lectin-sugar binding.

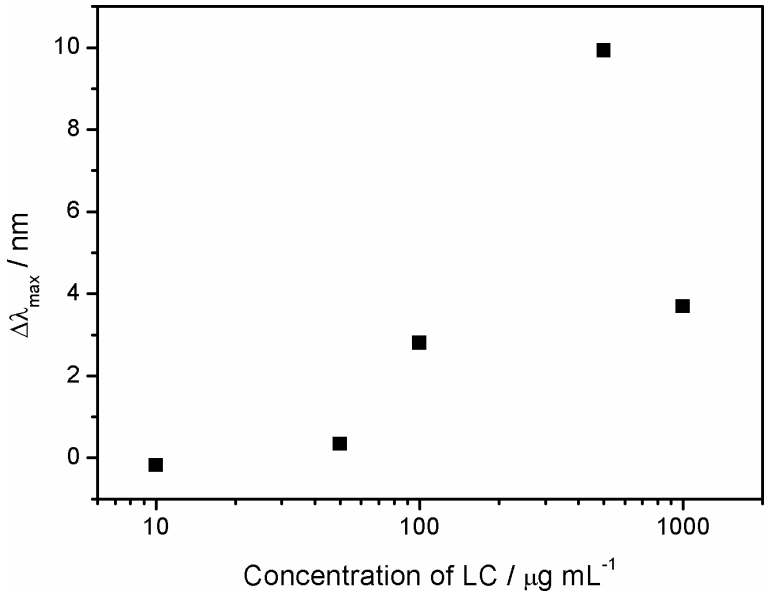

Fig. 68 Shift of the resonance wavelength upon change of concentration of the LC lectin measured for platform with 100 mM glucose adsorbed on rGO.

It was shown that use of reduced graphene oxide diminished nonspecific interactions between the substrate and lectins. It was visible that LC lectin preferentially binds to glucose but relatively large amount of sugar was needed to cause a significant shift in the resonance wavelength. Random, nonspecific interactions exhibited shifts of the resonance wavelength in a range of 3 nm. A similar shift was found for binding of mannose, showing that the interaction between both lectins and mannose is largely non-specific.

4.2.3 LSPR study of dielectric properties of bacteria

The main classification of bacteria types is based on the differences in the structure of the cell wall. The cell wall of Gram-positive bacteria (G+) is thick and consists of inner membrane and many layers of peptidoglycan and teichoic acids. The cell wall of Gram-negative (G-) bacteria is relatively thin and contains only a few layers of peptidoglycan. Beside inner membrane also outer membrane is present in G- bacteria, with lipoproteins and lipopolysaccharides

in its structure. Standard method of distinguishing G+ and G- bacteria is the Gram staining. Problems with this protocol (e.g. false-positive or false-negative results, vulnerability to operators' errors) lead to development of alternative or complementary methods like KOH string test or fluorescent staining. [227-229]

There are situations e.g., in food or pharmaceutical industry, when it is very useful to distinguish bacteria due to their viability. Aside from being alive or dead, bacteria could also exist as viable but non-culturable cells (VBNC). [230] Bacteria enter VBNC state as a response to the external stress, e.g. starvation. This is a state of low metabolic activity in which cells demonstrate reduced nutrient transport, rate of respiration and synthesis of macromolecules. It is generally accepted that VBNC cells are alive but incapable of undergoing the cell division necessary to grow and to form colonies on growth media. [231] If VBNC cells are present, the total number of viable bacteria will be underestimated by classical colony count method. Ultimately, the sample might give false negative result, if all bacteria are in VBNC state. The risk emerges from the ability of VBNC cells to resuscitate into culturable cells under suitable conditions. [112] Therefore, the detection of bacteria in VBNC state is of importance for medical diagnostics, food industry and maintenance of water distribution systems to name only a few.

From differences in the morphology of the bacterial cell wall (size, proteins amount, etc.) or in viability arise also differences in electric properties. [232, 233] In living cells the membrane potential is caused by the accumulation of mobile electric charge carriers at the membrane surfaces which move under oscillating electric field. [234] For instance, it was experimentally established that the effective dielectric constant is higher for G+ bacteria than for G- bacteria. [235] Also the state of the bacteria influences the electric properties of the cells. Beside differences in metabolism, gene expression, resistance and virulence potential also the cellular morphology, cell wall and/or membrane composition and adhesion properties distinguish live and VBNC cells. [236] Upon the cell death the membrane potential drastically changes. [234, 237, 238] Such effects were measured by techniques sensitive to the changes in electrical properties (as dielectric spectroscopy [239] or electrostatic force microscopy [235]) and explained by mathematical models. [234] Therefore, the electric properties of the G+, G-, live, VBNC and dead cell should be

pronounced. Moreover, plasmonic sensors – sensitive to the dielectric properties of the sample, were used to monitor the growth of the bacterial colony [240, 241] and cell distinguishing. [242] Majority of such experiments was based on detection of mass adsorbed at the surface through the specific recognition elements (e.g. antibodies). Such measurements gave almost no information on properties of bacteria themselves.

In this part of the dissertation dielectric properties of Gram-positive and Gram-negative bacteria were studied by measuring the shift in localized surface plasmon resonance wavelength.

The AgCitNPs platforms were electrodeposited according to the protocol described in *Section 3.3*. Bacteria were cultured according to standard protocols. *Escherichia coli* BL21 (G-), *Serratia marcescens* PCM 549 (G-), *Enterobacter aerogenes* PCM 1832 (G-), *Corynebacterium glutamicum* PCM 1945 (G+) and *Staphylococcus epidermidis* wild type (G+) were cultured in lysogeny broth (LB) medium, and *Lactobacillus casei* PCM 476 (G+) in MRS medium. The media in the form of instant mixes were purchased from Carl-Roth (Germany). First, the single colony from agar plate was inoculated into the proper medium for overnight culturing (28˚C in case of *S. marcescens* and 37˚C in case of other strains, 200 rpm). Then the bacteria suspensions were centrifuged at 3000 rpm for 4 minutes and resuspended in sterile 0.1 M phosphate buffer of pH equal to 7.5. The centrifugation – resuspension cycle was repeated two times before further experiments. The colony count method after seeding the bacteria onto agar plate was used for determination of concentration of bacteria within the samples. Colony forming units (CFU) can be directly correlated with the number of bacteria within the specific volume of the suspension.

To evaluate the effect of AgCitNPs and light beam on the studied bacteria the number of bacteria (expressed in CFU per mL) was controlled after the experiment with AgCitNPs and after the control experiment without AgCitNPs. Again colony count method was used and 25 µL was spread onto the agar

plates. The agar plates were incubated in 37˚C for 24 hours and number of colonies on each plate was analyzed.

The viable but non-culturable (VBNC) state of the *E. coli* cells was induced according to the protocol described by Arana *et al.* [243] Shortly, the 250 mL of overnight bacteria culture in LB medium was centrifuged at 3000 rpm for 4 minutes and resuspended in 250 mL of sterile seawater. Then the suspension was centrifuged and resuspended again in 250 mL of sterile seawater. Afterwards such sample was placed in incubator (37˚C, 200 rpm) for 20 days. Such protocol results in roughly constant overall number of viable bacteria in the span of the experiment, small number of dead bacteria and the ratio between viable and culturable and viable but non-culturable cells around 1 to 1000. Samples were analyzed using SEM according to criterion of morphological changes of VNBC bacteria.

To deactivate the bacteria without destroying their integrity we utilized UV irradiation. [244] The small volume of bacteria suspension (the same batch as used for experiment with native bacteria) in 0.1 M phosphate buffer of pH = 7.5 was placed in sterile petri dish and irradiated for 30 minutes. Roth-H468.1 (Germany) UV lamp of total power of 16 W and two irradiation wavelengths (254 nm and 366 nm) was used.

A second portion of bacteria (from the same batch as used for experiment with native bacteria) were disrupted to form lysates with the use of ultrasonic homogenizer Sonics Vibra-cell VCX130 (US). The bacteria suspensions were sonicated for 2 minutes at 100 W.

The portions of the stock suspension of bacteria (G+ or G-; native, UV-treated or lysate – specified in proper section) were subsequently added to the cuvette containing the AgCitNPs substrate and 1.5 mL of phosphate buffer (0.1 M, pH 7.5), mixed gently and left for 15 min. After that time the UV-Vis spectrum was recorded. The ultimate result was obtained after the subtraction of the spectrum of the same bacteria concentrations but without AgCitNPs substrate. This was done to assure that the change of the optical density of bacterial suspension itself was not changing the LSPR signal. All measurements were performed independently on three separate AgCitNPs substrates.

At first, it was confirmed that prepared AgCitNPs substrates showed very low antibacterial activity in the time span of the experiment. The number of *E. coli* cells in the suspension exposed to AgNPs substrates did not differ significantly from the control, i.e. suspension cultured in absence of any substrate (see *Fig. 69*). As the contact between bacteria and studied AgNPs substrates was restricted by geometry it had negligible effect on the tested bacteria.

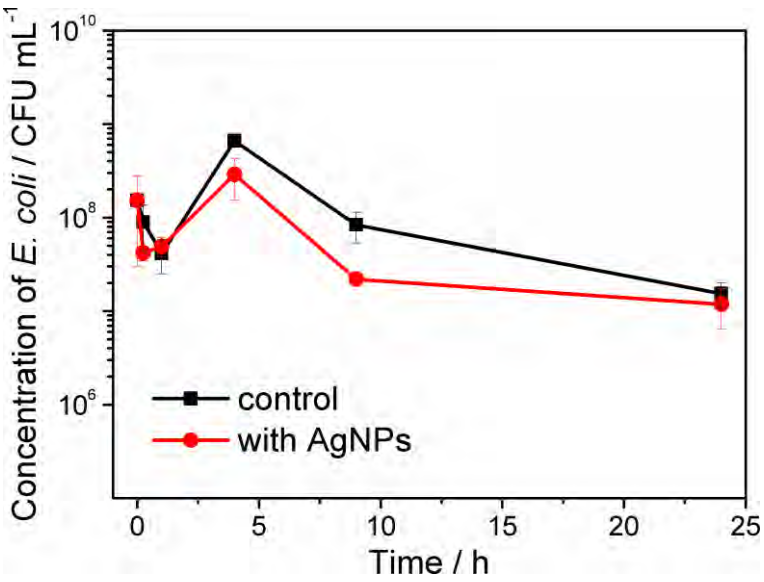

Fig. 69 Change of *E. coli* number upon contact with AgNPs platform within 24 hours (initial concentration: 1.5×10^8 CFU mL^{-1}).

Next step was to evaluate how our system is responding in time to the presence of bacteria. The AgCitNPs substrate was immersed into 5.6×10^5 CFU mL^{-1} of *E. coli* for 24 hours and changes in UV-Vis spectra were recorded. The result shown in Fig. 70 shows that the resonance wavelength exhibits the fastest shift within first 15 minutes (see inset in *Fig. 70*) and slows down significantly after 4 hours of the measurement.

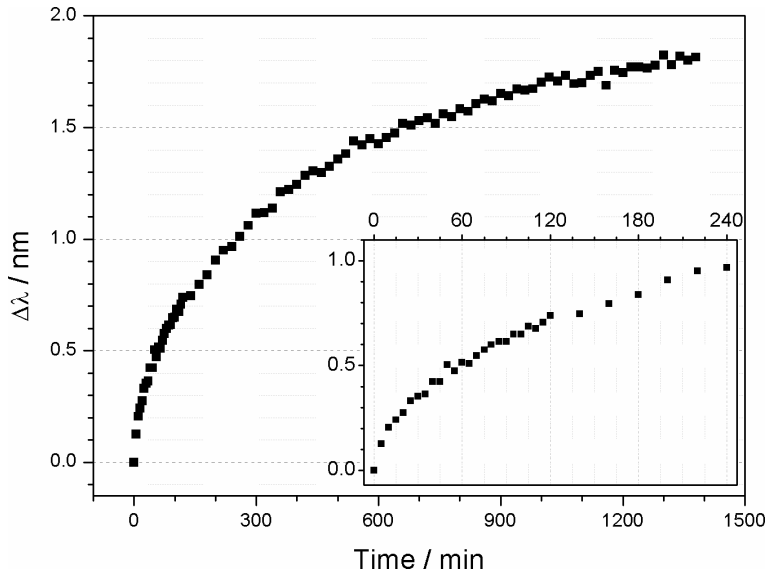

Fig. 70 The shift of the resonance wavelength after immersion of the AgCit(T)NPs substrate into 5.6×10^5 CFU mL^{-1} solution of *E. coli* for 24 hours.

To check whether or not tested substrates are responding to the change of bacteria concentration the shift of AgCitNPs resonance wavelength was monitored upon immersion into different concentrations of *E. coli* for 2 hours. From obtained spectra (examples shown on inset of *Fig. 71*) the positions of λ_{max} were determined and plotted against bacteria concentration (*Fig. 71*). The observed resonance wavelength was independent on the concentration of bacteria below 10^5 CFU mL^{-1}. In the range from 10^5 to 10^7 CFU mL^{-1} significant increases in resonance shift were observed with increasing concentration of bacteria. Thus this regime was used in further experiments. Because of the high turbidity of the suspension causing big errors 10^7 CFU mL^{-1} was considered as the maximum concentration.

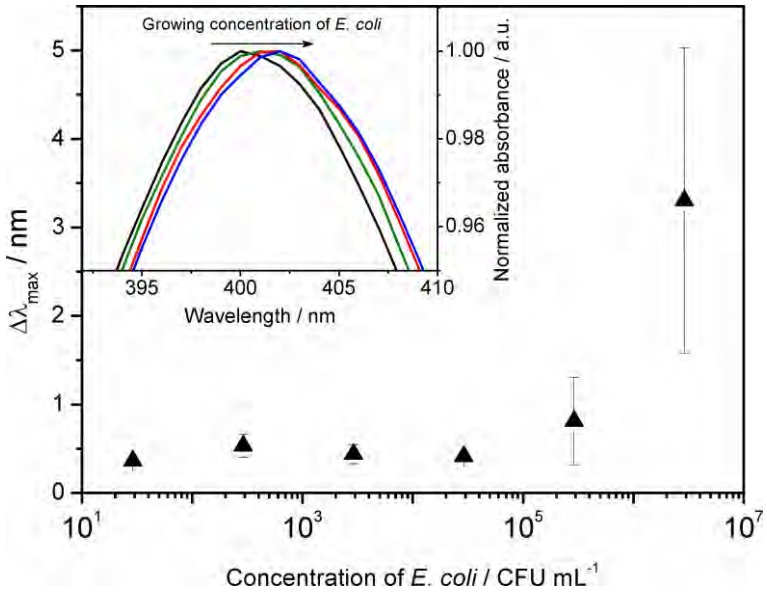

Fig. 71 Relation between the shift of resonance wavelength and concentration of *E. coli* used; inset presents exemplary UV-Vis spectra showing shifts of the resonance wavelength of AgCitNPs substrates upon change of concentration of *E. coli* (100, 3×10^4, 3×10^5, 3×10^6 CFU mL^{-1}, respectively).

Several strains of G+ and G- bacteria of different shape and size were chosen to test if there will be any difference in obtained plasmonic responses of AgCitNPs platform. SEM observations were utilized to quantitatively describe the geometry of studied bacteria. Calculated mean dimensions of different strains are summarized in *Table 7*.

Since the evanescent field of LSPR is in a range of 50 - 100 nm, it was only possible to record the AgCitNPs plasmonic response from the bacterial cell wall. It was expected that the response will be influenced by three factors: area occupied by single bacteria, chemical composition of the cell wall (its thickness) and bacteria viability (since the dielectric coefficient differs depending on whether the bacteria is alive or dead [239]). Because the platform used was conductive it could be excluded that shifts observed come from the direct charge of bacterial cells. To confirm this assumption a series of experiments was performed.

Table 7 Summary of the sizes of the measured bacterial strains ("surface area" means the area of the whole cell wall and "area occupied" means the area of the bacterial cross-section parallel to the surface). $n = 50$ cells

	E. coli BL21 (G-)	E. aerogenes (G-)	S. marcescens (G-)	S. epidermidis (G+)	L. casei (G+)	C. glutamicum (G+)
Length [µm]	2.83 ± 0.53	1.50 ± 0.32	0.88 ± 0.16	0.78 ± 0.11	1.56 ± 0.42	1.27 ± 0.25
Width [µm]	1.03 ± 0.14	0.75 ± 0.18	0.59 ± 0.09	0.73 ± 0.09	0.49 ± 0.06	0.86 ± 0.11
Ratio L/W	2.80 ± 0.70	2.07 ± 0.50	1.51 ± 0.26	1.08 ± 0.11	3.28 ± 1.19	1.49 ± 0.32
Volume [µm^3]	1.58 ± 0.53	0.44 ± 0.24	0.16 ± 0.05	0.23 ± 0.09	0.20 ± 0.07	0.50 ± 0.16
Surface area [µm^2]	7.58 ± 1.92	3.02 ± 1.25	1.46 ± 0.49	1.79 ± 0.49	1.96 ± 0.55	3.10 ± 1.09
Area occupied [µm^2]	2.29 ± 0.53	0.88 ± 0.29	0.41 ± 0.10	0.45 ± 0.12	0.60 ± 0.18	0.86 ± 0.20

First, two pairs of G+ and G- strains of similar shapes were compared (*Fig. 72*). *E. coli* (G-) was compared with *L. casei* (G+) (more elongated shape), and *E. aerogenes* (G-) with *C. glutamicum* (G+) (more rounded shape). The observed courses of all curves presented in *Fig. 72* were consistent with the changes of the refractive index of growing layer of bacteria. [241] However, in both cases the maximum shift of the resonance frequency was higher for G+ than for G- bacteria. Obtained results were consistent with the literature data showing that the composition of cell wall has big influence on the dielectric properties of bacteria. The corresponding data was published by Esteban-Ferrer *et al.* [235] The authors utilized Electrostatic Force Microscopy to prove that the effective dielectric constant for Gram-positive bacteria is higher in comparison to Gram-negative strains. Moreover, in case of studied pairs the G+ cells were smaller than G- (see dimensions of cells in *Table 7* and schematic representations on respective graphs). Probably this was also a cause of higher resonance

wavelength shifts for G+ bacteria – a greater number of smaller bacteria can be placed on the same surface unit in comparison to bigger bacteria.

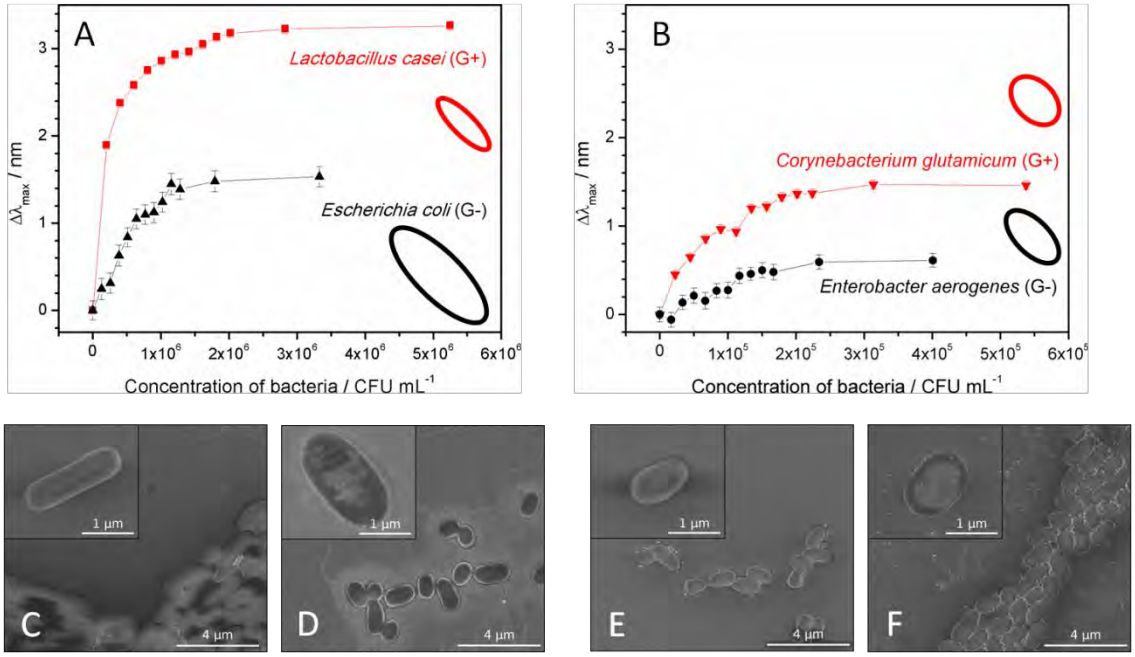

Fig. 72 Plots of the shift of resonance wavelength peak position ($\Delta\lambda_{max}$) vs. concentration of bacteria showing pairs of G+ and G- bacteria with schematic representation of their respective shapes and sizes on scale (A and B). SEM images of respective bacterial strains with insets showing size and shape of a single bacterial cell: *L. casei* (C), *E. coli* (D), *C. glutamicum* (E) and *E. aerogenes* (F).

The influence of the size of bacteria cells was further examined. In *Fig. 73A* and *Fig. 73B* are presented the graphs for different G+ and G- strains, together with schematic representations of their sizes and shapes (adequate SEM images can be seen in *Fig. 72C - 72F* and *Fig. 73C - 73D*). The general rule was complied, e.g. larger shifts of the resonance wavelength were obtained for a greater mass adsorbed on the active surface. For *S. epidermidis* and *S. marcescens* their small size enabled adsorption of larger number of cells per surface unit than in the case of bigger cells. Surprisingly, the change of the resonance wavelength caused by *S. marcescens* (G-) was larger than change for similar in size *S. epidermidis* (G+). The most probable explanation is that only

very long flagella of *S. marcescens* can be seen due to small evanescent field (50 – 100 nm). This result shows a great significance of the features of the bacterial cell wall on the changes of the recorded signals. All other differences between signals obtained for G+ and G- strains could be explained with differences in the dielectric coefficient of those types.

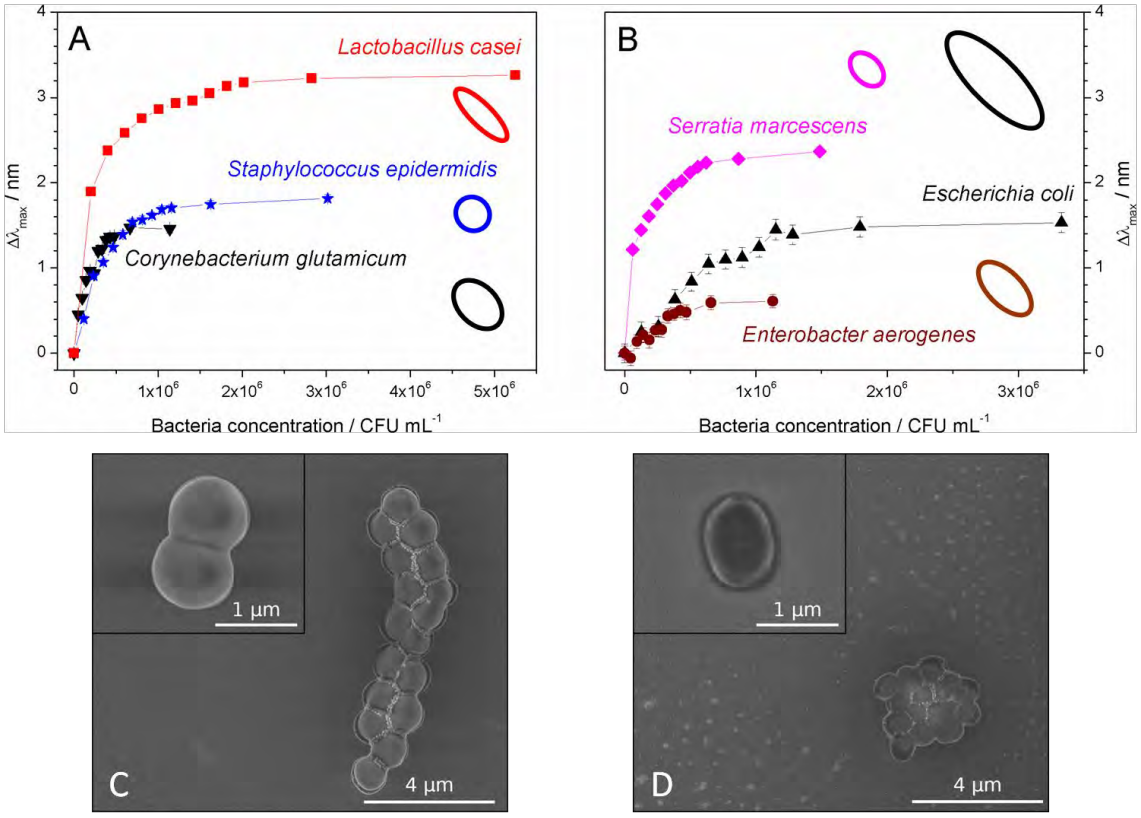

Fig. 73 Comparison of signals obtained from different strains of Gram-positive (A) and Gram-negative bacteria (B) of different sizes; SEM images of *S. epidermidis* (C) and *S. marcescens* (D) with insets showing size and shape of a single bacterial cell.

In order to distinguish living and dead bacteria using LSPR. *L. casei* (G+) and *E. coli* bacteria were compared. Shifts of AgCitNPs resonance wavelength upon addition of native bacteria, lysates and UV-treated bacteria were analyzed (*Fig. 74* and *Fig. 75*). Obtained results confirmed the assumption that the shift of the resonance wavelength depends on area occupied by single cell, chemical composition of the cell wall/membrane and viability of the cell.

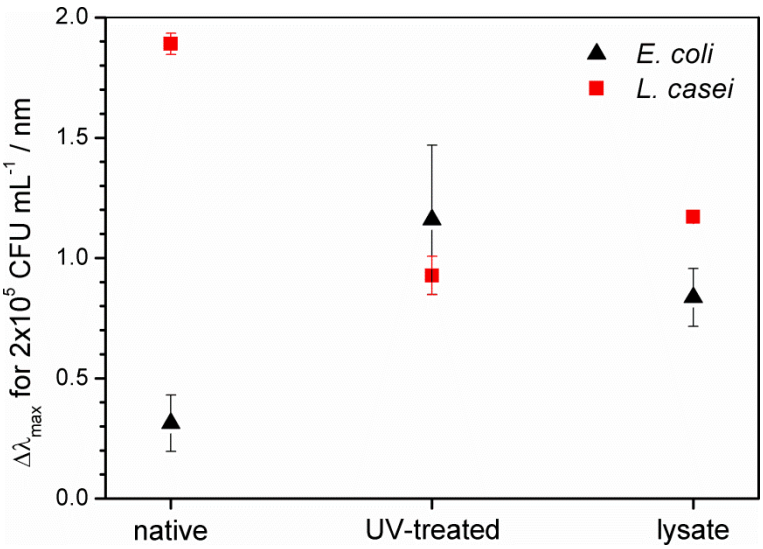

Fig. 74 Comparison of shifts of the resonance wavelengths obtained for 2×10^5 CFU mL^{-1} of E. coli batch in form of native cells, UV-treated cells or lysate.

The greater shifts in the resonance wavelength were obtained for native G+ bacteria (*L. casei*). For UV-treated cells the shift was in the same range. In case of lysates the signal obtained was slightly higher for G+. Those results confirmed the assumption that the shift of the resonance wavelength depends on area occupied by single cell, chemical composition of the cell wall/membrane and viability of the cell. Lysates consisted of objects much smaller than the whole bacterial cell - fragments of cell walls, membranes, DNA and other molecules. In consequence it was possible to observe growth of the layer of proteins obtaining the shift of about 12 nm (see right panel of *Fig. 75*). The shift was greater for G+ than for G- bacteria because of differences in the structure of the cell walls and membranes (more complicated and thicker for G+).

UV-treated bacteria are in fact big chunks of organic matter (in the shape of the cells, see AFM images on *Fig. 76*) with no metabolism. As such they do not build up any ionic and molecular gradients and do not exhibit dielectric properties typical for living cells. Thus, the shift of the resonance wavelength should depend only on the size and chemical composition of the cell wall. As can be seen on the left panel of *Fig. 75* for the unit of surface bigger amount of

smaller objects can be adsorbed (*L. casei* cells are smaller than *E. coli* cells) resulting in higher shifts of the resonance wavelength.

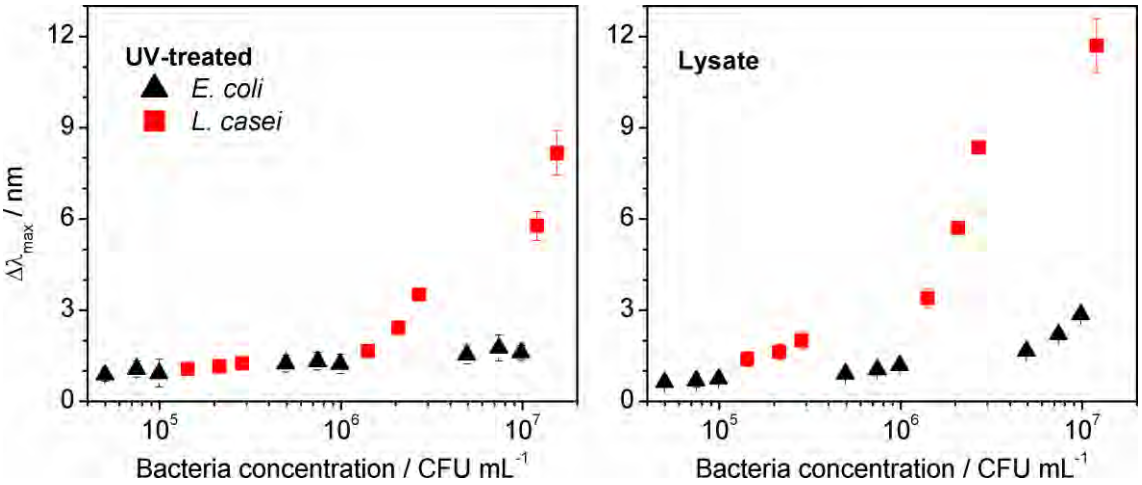

Fig. 75 Comparison of the shift of Ag resonance wavelength upon addition of UV-treated cells (left panel) and lysate (right panel) for *E. coli* and *L. casei*.

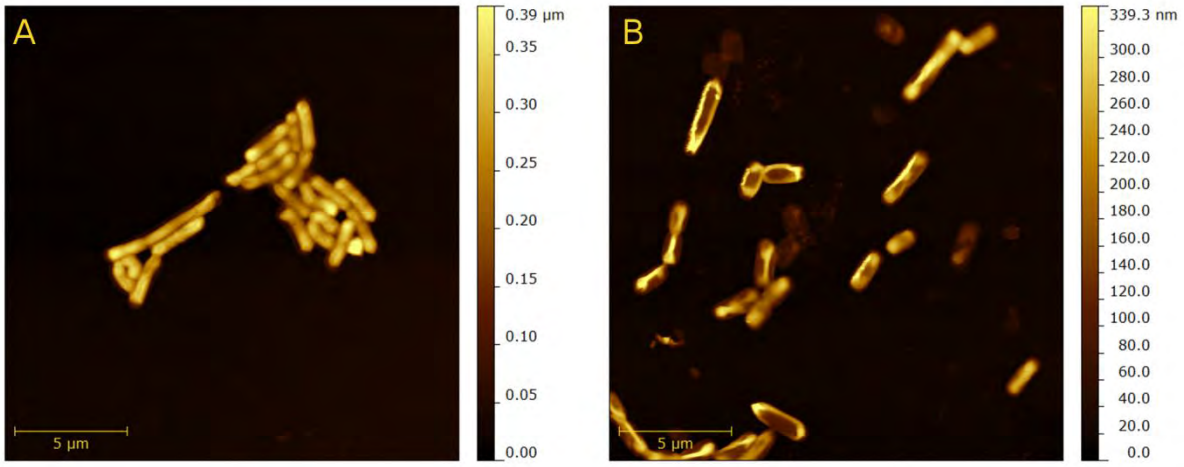

Fig. 76 Atomic Force Micrographs of *L. casei* cells (A) native, (B) UV-treated.

Finally, the experiment with viable but non-culturable (VBNC) *E. coli* was performed. As can be seen in *Fig. 77* the signal from VBNC is higher than for native bacteria. The most probable explanation bases on the fact that during transformation into VBNC, bacteria are changing their shape and the structure of the cell wall. Consequently they are decreasing the area occupied by one bacterium (enabling more dense coverage of the surface). The observed shape of the curve is very similar to the simple mass adsorption curve. It can be caused also by a drastic decrease of metabolism observed for VBNC and, in consequence, drastic change of dielectric coefficient.

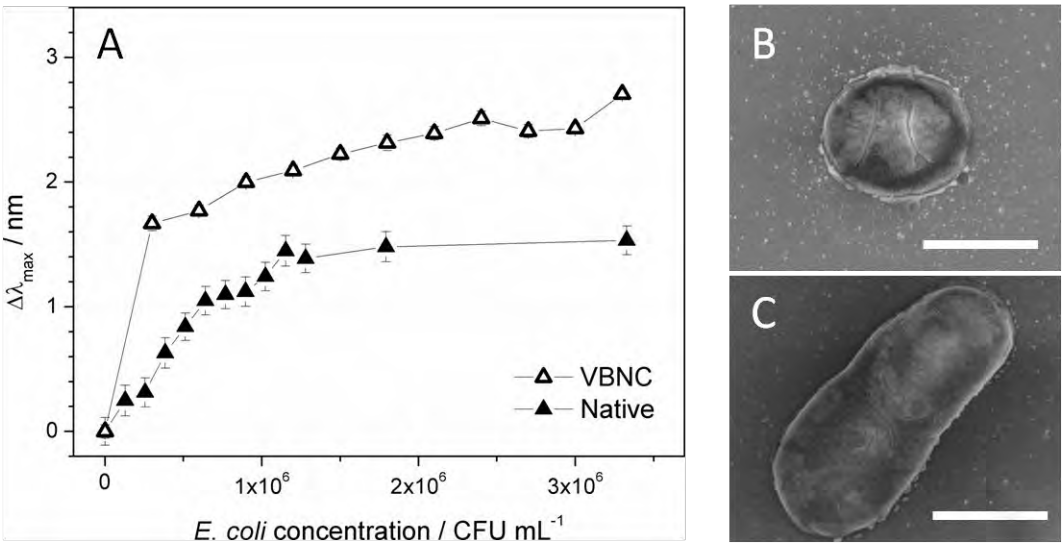

Fig. 77 A - Comparison of the shift of Ag resonance wavelength upon addition of native *E. coli* (full triangles), viable but non-culturable (VBNC) *E. coli* (empty triangles); B – SEM image of VBNC *E. coli*; C – SEM image of native *E. coli* (for both SEM images the scale bar is 1 μm).

It was shown that the localized surface plasmon resonance is a suitable technique for qualitative study of dielectric properties of bacteria. The resonance wavelength shift depends on the viability and type of the microorganism. In consequence it is possible to distinguish Gram-positive from Gram-negative bacteria. Moreover, it is a promising tool to analyze bacteria due to their viability. For the first time a study of changes in the

dielectric properties of *E. coli* after entering VBNC state is shown. The presented method is complementary (or alternative in some cases) to the traditional biological practice (as the Gram staining). It bases only on the physical properties of tested bacteria such as their size and dielectric coefficient.

4.2.4 Detection of T7 bacteriophages

Bacteriophages are probably the most common organisms on Earth. Their number is estimated to be around 10^{31} with 10^{8} different genotypes. [245, 246] They are very specific bacterial viruses. They use their bacterial hosts for multiplication and propagation of mature virions and thus are natural regulators of bacterial populations in nature. [247] Bacteriophages were discovered in early 20th century when Ernest Hankin noticed that waters of Ganges and Yamuna contained some antibacterial factor which prevented people from cholera. [246] Works on the topic started with publication of Felix Twort in 1915 and of Felix d`Herelle in 1917. [248]

Bacteriophages are composed of protein capsule enclosing the genetic material (DNA or RNA) and of adhesins – proteins responsible for specific recognition of host cell. Different shapes of these organisms are possible – rounded, elongated, with or without tail. In this study T7 bacteriophage (*Podoviridae* family) was used. It has a head containing DNA and a very short tail with fibers constructed with adhesins (see *Fig. 78*). It is specific to *E. coli*.

Nowadays, there are multiple reports about using bacteriophages as recognition elements in biosensors. [245, 249-253] Also, bacteriophages can be used in treatment of bacterial infections as an alternative to antibiotics (also for drug-resistant bacteria) [254] or in general prevention against bacterial infections in both, plants and animals. [246] They are also used in food industry, especially at fields were bacteria are used e.g. in diary production or brewery to eradicate any unwanted species of bacteria. [245, 255]

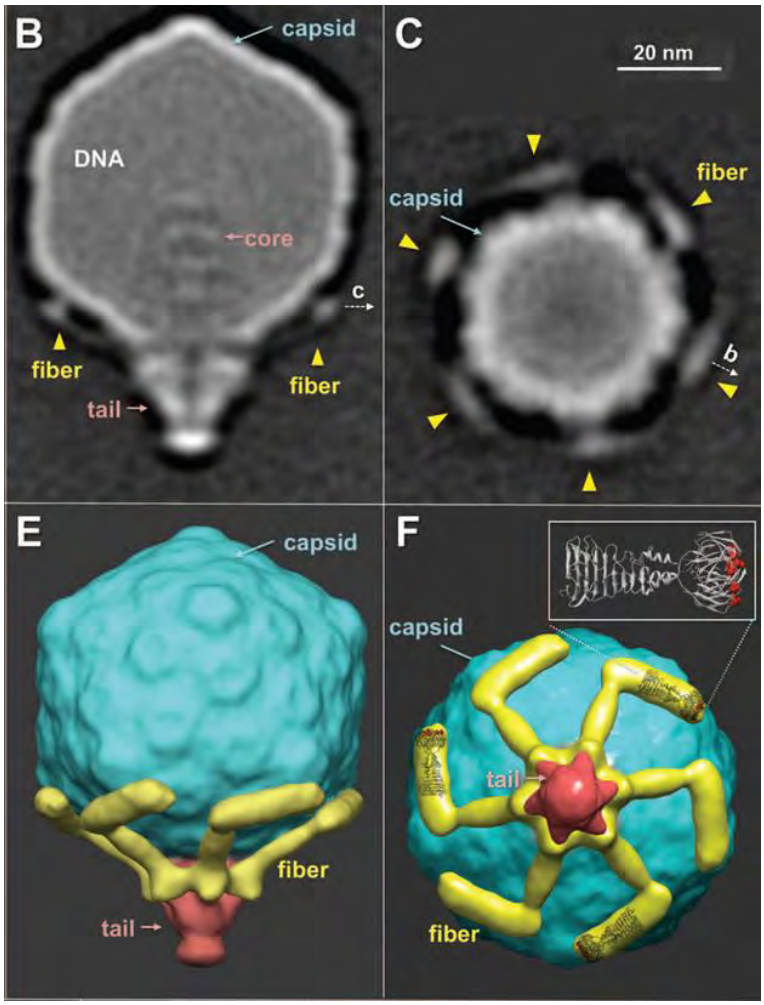

Fig. 78 Cryo–electron tomography images (B and C) with 3D surface rendering (E and F) of morphology of T7 bacteriophage (B and E – side view, C and F – bottom view); adapted from: [256]

Since bacteria are widely used in industry to produce biochemically relevant molecules, it is crucial to monitor possible contaminations with bacteriophages. [257-259] Furthermore, bacteriophages can be treated as model objects (non-toxic and safe for human) in studying virus detection. [260-262] There are several methods allowing to detect bacteriophages, among others polymeraze chain reaction (PCR) [261, 262], biochips [257, 259], quartz crystal microbalance [258], RNA hybridization. [263] Moreover Lesniewski *et al.* showed the possibility of detecting bacteriophages using colorimetric test on gold nanoparticles. [134] In their study LSPR effect was exploited – the UV-Vis spectrum changed after addition of T7 bacteriophages due to aggregation of

antibody-covered AuNPs. SPR technique was used by Garcia-Aljaro *et al.* to detect *E. coli*-specific bacteriophages. [264]

In this study the proof of concept for detection of T7 bacteriophages by means of LSPR on electrodeposited silver nanostructures is shown.

The AgCitNPs platforms were electrodeposited according to the protocol described in *Section 3.3*. In the next step thin films of silica were applied using plasma-assisted chemical vapor deposition (PACVD) in an Oxford PlasmaLab System 80+ (Oxford Instruments, Abingdon, UK). First samples were heated in 350˚C for 2 minutes in Ar atmosphere (flow 50 mL min^{-1}). Next PACVD was performed for 20 or 30 seconds in 350˚C under following conditions: flow of SiH_4 – 100 mL min^{-1}, flow of N_2O – 500 mL min^{-1}, power – 80 W, pressure – 1 Torr.

Obtained silica layer was functionalized with (3-aminopropyl)triethoxysilane (APTES, obtained from ABCR) via vapor deposition according to the procedure described in [265]. Samples were placed in dessicator along with two vials containing APTES in the first one and triethylamine (obtained from POCh) as a catalyst in the second one (APTES to catalyst volume ratio was 3:1). The reaction proceeded for 2 hours in N_2 atmosphere. After that time reagents were removed from dessicator and samples were left in N_2 atmosphere for next 48 hours.

As a detecting element polyclonal anti-T7-Tag antibodies from rabbit serum were used (IgG, obtained from MBL C.O. LTD., Japan). They were bound covalently to the $–NH_2$ functionalized surface. Carboxylic groups in antibodies were activated with N-(3-Dimethylaminopropyl)-N′-ethylcarbodiimide hydrochloride (EDC, obtained from Sigma) for 30 minutes. The solution contained 5 µL of 0.2 M EDC, 500 µL of phosphate buffer saline (PBS, pH 7.4, tablets obtained from Sigma) and 5 µL of antibodies (1.8 mg mL^{-1}). This

solution was dropcasted (20 µL) onto ITO|AgCit(T)NPs|SiO_2|APTES platform, left for 1 hour and washed gently with PBS.

T7 bacteriophages were cultured according to the protocol described in [134, 266]. Detection was performed after overnight adsorption of T7 from dropcasted 20 µL droplet of 10^{10} PFU mL^{-1} solution and gentle washing with PBS.

Every stage of preparation of platforms as well as detection were monitored using UV-Vis spectrophotometer. Each experiment was repeated three times.

Thin films of SiO_2 were deposited on the AgCitNPs platform to protect the surface against Cl^- ions present in PBS buffer. The thickness of the film was 55 nm for 30 seconds and 15 nm for 20 seconds of PACVD. SiO_2 was chosen because it can be easily modified using silane precursors with different functional groups. Functionalization with APTES allowed formation of covalent peptide bonds between –NH_2-terminated silane and –COOH groups present in antibodies. Exemplary UV-Vis spectra recorded for every stage of experiment are presented on inset of *Fig. 79*.

Fig. 79 shows the shifts of resonance wavelengths between each stage of the experiment. As can be seen covering the AgCitNPs with SiO_2 layers caused a significant shift of the λ_{max} – 31,9 nm for 20 seconds of PACVD and 32,2 nm for 30 seconds PACVD. Mean shift after vapor deposition of APTES was larger for 30 s sample. Those two steps were performed and measured in air. After binding of IgG, samples were kept in PBS and all measurements were done in PBS. The response of the system to the adsorption of IgG as well as to the addition of bacteriophages was bigger for samples with thinner SiO_2 layer. For detection of T7, the signal was three times higher (3.04 nm for 15 nm layer versus 0.92 nm for 55 nm layer). It is because plasmon resonance is a phenomenon confined to the surface and its decay length is in a range of tens of nanometers. [267, 268] Additional thin layer of a dielectric, such as SiO_2 allows electromagnetic coupling between metal and dielectric plasmons and spreading of coupled plasmons along the dielectric layer. The thicker the

dielectric layer, the weaker the improvement of the platform sensitivity can be obtained.

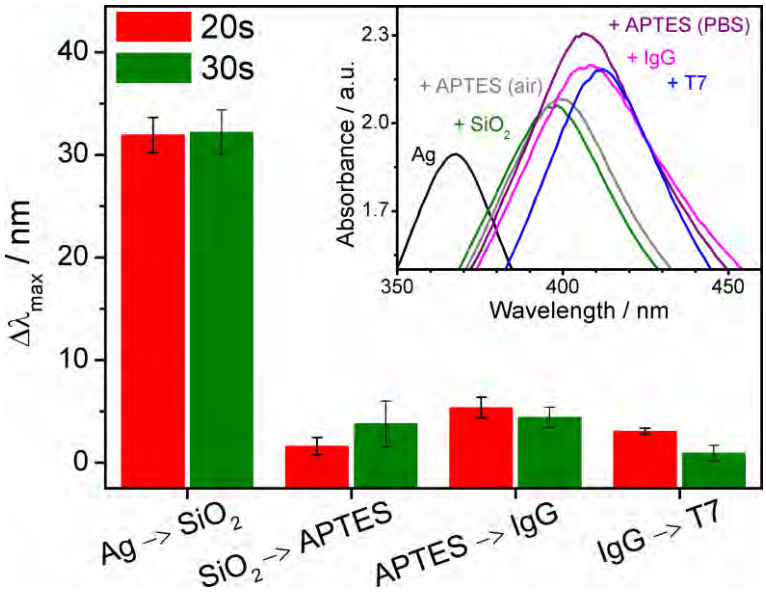

Fig. 79 Shift of the resonance wavelength in subsequent stages of experiment (error bars calculated for three separate samples); inset – example of adequate UV-Vis spectra (spectra black, green and grey were measured in air and violet, pink and blue in PBS). "Ag" refers to bare AgCit(T)NPs platform.

The proof of concept for detection of bacteriophages using LSPR system was shown. SiO_2 layer was used to protect AgCitNPs from Cl^- ions in solutions. Sensitivity of the system depended on the thickness of the SiO_2 layer.

Chapter 6

Summary and conclusions

Plasmonic-based sensors are valuable tools in studying molecular interactions and label-free detection in real time to mention just a couple examples. Used setups are relatively simple and can be miniaturized and integrated. Their crucial element is the sensing platform. Depending on the chosen technique the platform should exhibit different features. This dissertation was focused on fabrication of platforms showing:

- a narrow plasmon resonance peak in the UV-Vis spectrum and high refractive index sensitivity for use in LSPR, and/or
- a high enhancement factor for use in SERS.

The fabrication method of choice was electrodeposition. It does not require specific sample preparation or sophisticated equipment. It can be performed in aqueous solutions with environmentally friendly chemicals. It is also cheap and allows easy control over many parameters of deposition. Cyclic voltammetry was used to assure repeatable nucleation and growth cycles resulting in good surface coverage. Obtained platforms were ITO-based silver and gold submicrostructures. Chapters 3 and 4 describes the optimization of electrodeposition parameters.

The main conclusion from this part is that cyclic voltammetry is suitable to fabricate tailored morphologies of silver and gold deposits. Desired structures were obtained without any templates and using only plating baths consistent with the principles of “green chemistry”. Citrate ions and glucose worked well as reducing agents. Future work should be focused on improvement of the

morphology e.g. by introducing other working electrodes instead of ITO or by introducing an additional templating layer. A key point should be to gain more control over the interparticle distances since it is a crucial parameter in the creation of “hot spots”.

In Chapter 5 possible applications in SERS and LSPR are presented with detailed summaries. Summing up: fabricated platforms exhibited EF high enough to record SERS spectra of neurotransmitters in physiologically relevant concentrations. Although it was impossible to quantitatively determine the amount of choline in such a complex sample as human blood serum. Probably the protocol of sample preparation needs to be improved. In case of LSPR a broad range of possible applications was shown. Refractive index sensitivity test was demonstrated with monitoring BSA adsorption. Molecular interactions were studied with lectins-to-sugars binding using graphene oxide or reduced graphene oxide as a supporting layer for sugars. It was shown that functional groups on graphene oxide cause greater unspecific binding of lectins to the platform. Other ways of immobilizing sugars would be worth checking, e.g. covalent bonding through linkers or immobilization in gels. Another application was studying of dielectric properties of bacteria. Developed platforms were sensitive enough to sense the difference in dielectric coefficient between Gram-positive and Gram-negative bacteria. Moreover, it was possible to differentiate bacteria according to their viability. Further work can include quantitative measurement of dielectric coefficients of various microorganisms. As last, a proof-of-concept of a biosensor was shown. T7 bacteriophages were recognized with specific antibodies covalently bound to the platform. In this case a very important element was a thin dielectric film applied on top of the silver nanostructures. It not only allowed an easy functionalization of the platform but also protected the silver structures from chloride ions. In this particular system attention should be paid to the thickness of the dielectric layer. According to calculations performed by Lahav *et al.* if a very thin layer of dielectric having high refractive index and very low absorbance is applied onto the metal surface, the enhancement of the sensitivity can reach one order of magnitude. [269] Future works should not only be focused on increasing the enhancement of the sensitivity but also on checking limits of detection of the method.

With presented examples a broad range of applications of plasmonic methods was shown. What is more important, all those experiments were performed on platforms fabricated by means of easy and unwasteful electrodeposition from environmentally-friendly solutions. One of the presented platforms – AgCitNPs – is universal and can be used in both, SERS and LSPR studies.

References

1. Bellis, M. 15/09/2013]; Available from: http://inventors.about.com/od/estartinventions/a/Electroplating.htm.
2. Paunovic, M., Schlesinger, M. , ed. *Fundamentals of electrochemical deposition*. 2nd ed. 2006, Wiley.
3. Smee, A., *Elements of electro-metallurgy*. 1841, London.
4. Bard, A.J., Inzelt, G., Scholz, F. (Eds.), ed. *Electrochemical dictionary*. 2nd ed. 2012, Springer.
5. Caspari, W.A., *Über elektrolytische gasentwickelung.* Zeitschrift für physikalische Chemie, Stöchiometrie und Verwandtschaftslehre, *30* (**1899**) 89.
6. Tafel, J., Naumann, K., *Beziehungen zwischen kathodenpotential und elektrolytischer reduktionswirkung.* Zeitschrift für physikalische Chemie, Stöchiometrie und Verwandtschaftslehre, *50* (**1905**) 713.
7. Rogers, L.B., Krause, D. P., Griess, J. C. , Ehrlinger, D. B. , *The electrodeposition behavior of traces of silver.* Transactions of The Electrochemical Society, *95* (**1949**) 33.
8. Kolb, D.M., *et al.*, *Underpotential deposition of metals and work function differences.* Journal of Electroanalytical Chemistry and Interfacial Electrochemistry, *54* (**1974**) 25.
9. Erdey-Gruz, T., Volmer, M., *Zur frage der elektrolytischen metallüberspannung* Zeitschrift für physikalische Chemie, Abteilung A, Chemische Thermodynamik, Kinetik, Elektrochemie, Eigenschaftslehre, *157A* (**1931**) 165.
10. Frank, F.C., *The influence of dislocations on crystal growth.* Discussions of the Faraday Society, *5* (**1949**) 48.
11. Burton, W.K., *et al.*, *The growth of crystals and the equilibrium structure of their surfaces.* Philosophical Transactions of the Royal Society of London. Series A, Mathematical and Physical Sciences, *243* (**1951**) 299.
12. Motta, N., *et al.*, *Role of patterning in islands nucleation on semiconductor surfaces.* Comptes Rendus Physique, *7* (**2006**) 1046.
13. Schaltin, S., *et al.*, *High current density electrodeposition from silver complex ionic liquids.* Physical Chemistry Chemical Physics, *14* (**2012**) 1706.
14. Volmer, M., Weber, A., *Keimbildung in übersättigten gebilden (nucleation of supersaturated structures).* Z. Physik. Chem., *199* (**1926**) 277.
15. Erdey-Grúz, T.V., M., *Zur frage der wasserstoffüber- spannung.* Z. Phys. Chem., *150* (**1930**) 203.
16. Scharifker, B. and Hills, G., *Theoretical and experimental studies of multiple nucleation.* Electrochimica Acta, *28* (**1983**) 879.
17. Scharifker, B. and Mostany, J., *Three-dimensional nucleation with diffusion controlled growth: Part i. Number density of active sites and nucleation rates per site.* Journal of Electroanalytical Chemistry and Interfacial Electrochemistry, *177* (**1984**) 13.
18. Ustarroz, J., *et al.*, *New insights into the early stages of nanoparticle electrodeposition.* The Journal of Physical Chemistry C, *116* (**2011**) 2322.
19. Ustarroz, J., *et al.*, *A generalized electrochemical aggregative growth mechanism.* Journal of the American Chemical Society, *135* (**2013**) 11550.
20. Ustarroz, J., *et al.*, *The role of nanocluster aggregation, coalescence, and recrystallization in the electrochemical deposition of platinum nanostructures.* Chemistry of Materials, *26* (**2014**) 2396.
21. Milchev, A. and Stoyanov, S., *Classical and atomistic models of electrolytic nucleation: Comparison with experimental data.* Journal of Electroanalytical Chemistry and Interfacial Electrochemistry, *72* (**1976**) 33.
22. Fang, J., *et al.*, *How a silver dendritic mesocrystal converts to a single crystal.* Applied Physics Letters, *92* (**2008**) 173120.

23. Wang, C. and Fang, J., *Octahedral noble-metal nanoparticles and their electrocatalytic properties.* ChemSusChem, *6* (**2013**) 1848.
24. Solla-Gullon, J.*, et al.*, *Shape-dependent electrocatalysis: Methanol and formic acid electrooxidation on preferentially oriented pt nanoparticles.* Phys Chem Chem Phys, *10* (**2008**) 3689.
25. Lai, S.C.S.*, et al.*, *Nucleation, aggregative growth and detachment of metal nanoparticles during electrodeposition at electrode surfaces.* Chemical Science, *6* (**2015**) 1126.
26. Kaniyankandy, S.*, et al.*, *Electrodeposition of silver nanodendrites.* Nanotechnology, *18* (**2007**) 125610.
27. Huang, H.-l.*, et al.*, *Effects of direct current electric field on corrosion behaviour of copper, cl− ion migration behaviour and dendrites growth under thin electrolyte layer.* Transactions of Nonferrous Metals Society of China, *24* (**2014**) 285.
28. Nikolić, N.D.*, et al.*, *The potentiostatic current transients and the role of local diffusion fields in formation of the 2d lead dendrites from the concentrated electrolyte.* Journal of Electroanalytical Chemistry.
29. Wranglén, G., *Dendrites and growth layers in the electrocrystallization of metals.* Electrochimica Acta, *2* (**1960**) 130.
30. Hou, Q.*, et al.*, *Growth of porous zno nanosheets by electrodeposition with the addition of kbr in nitrate electrolyte.* Materials Letters, *89* (**2012**) 283.
31. Najdovski, I. and O'Mullane, A.P., *The effect of electrode material on the electrochemical formation of porous copper surfaces using hydrogen bubble templating.* Journal of Electroanalytical Chemistry, *722–723* (**2014**) 95.
32. Cherevko, S.*, et al.*, *Electrodeposition of three-dimensional porous silver foams.* Electrochemistry Communications, *12* (**2010**) 467.
33. Cherevko, S. and Chung, C.-H., *Direct electrodeposition of nanoporous gold with controlled multimodal pore size distribution.* Electrochemistry Communications, *13* (**2011**) 16.
34. Guo, S. and Wang, E., *Synthesis and electrochemical applications of gold nanoparticles.* Analytica Chimica Acta, *598* (**2007**) 181.
35. Jans, H. and Huo, Q., *Gold nanoparticle-enabled biological and chemical detection and analysis.* Chemical Society Reviews, *41* (**2012**) 2849.
36. Murphy, C.J.*, et al.*, *Gold nanoparticles in biology: Beyond toxicity to cellular imaging.* Accounts of Chemical Research, *41* (**2008**) 1721.
37. Lesniewski, A.*, et al.*, *Antibody modified gold nanoparticles for fast and selective, colorimetric t7 bacteriophage detection.* Bioconjugate Chemistry, *25* (**2014**) 644.
38. Zhu, Y.-p.*, et al.*, *Sonochemical synthesis of silver nanorods by reduction of sliver nitrate in aqueous solution.* Ultrasonics Sonochemistry, *17* (**2010**) 675.
39. Lee, Y.H.*, et al.*, *Using langmuir-schaefer technique to fabricate large-area of dense sers-active au nanoprism monolayer films.* Nanoscale, *5* (**2013**) 6404.
40. Winkler, K.*, et al.*, *Gold micro-flowers: One-step fabrication of efficient, highly reproducible surface-enhanced raman spectroscopy platform.* Plasmonics, *6* (**2011**) 697.
41. Datta, M. and Landolt, D., *Fundamental aspects and applications of electrochemical microfabrication.* Electrochimica Acta, *45* (**2000**) 2535.
42. Said, R.A., *Microfabrication by localized electrochemical deposition: Experimental investigation and theoretical modelling.* Nanotechnology, *14* (**2003**) 523.
43. Ye, W.*, et al.*, *Template-free and direct electrochemical deposition of hierarchical dendritic gold microstructures: Growth and their multiple applications.* The Journal of Physical Chemistry C, *114* (**2010**) 15617.
44. Nasirpouri, F.*, et al.*, *Electrodeposition and magnetic properties of three-dimensional bulk and shell nickel mesostructures.* Thin Solid Films, *519* (**2011**) 8320.
45. Mehmood, T.*, et al.*, *Mechanism for formation of fcc-cobalt nanowires in electrodeposition at ambient temperature.* Materials Letters, *130* (**2014**) 256.

46. Li, Z., *et al.*, *Electrodeposition of palladium nanoparticles on fullerene modified glassy carbon electrode for methane sensing.* Electrochimica Acta, *76* (**2012**) 288.
47. Zhang, H., *et al.*, *One-step electrodeposition of platinum nanoflowers and their high efficient catalytic activity for methanol electro-oxidation.* Electrochemistry Communications, *12* (**2010**) 882.
48. Simka, W., *et al.*, *Electrodeposition of metals from non-aqueous solutions.* Electrochimica Acta, *54* (**2009**) 5307.
49. Allemand, M., *et al.*, *Synthesis of cu-pd alloy thin films by co-electrodeposition.* Electrochimica Acta, *56* (**2011**) 7397.
50. Cojocaru, P., *et al.*, *Using deep eutectic solvents to electrodeposit cosm films and nanowires.* Materials Letters, *65* (**2011**) 3597.
51. Rapecki, T., *et al.*, *Electrodeposition of polypyrrole-au nanoparticles composite from one solution containing gold salt and monomer.* Electrochemistry Communications, *12* (**2010**) 624.
52. Lincot, D., *Electrodeposition of semiconductors.* Thin Solid Films, *487* (**2005**) 40.
53. Petersson, I. and Ahlberg, E., *Kinetics of the electrodeposition of pb-sn alloys: Part ii at polycrystalline gold electrodes.* Journal of Electroanalytical Chemistry, *485* (**2000**) 178.
54. Tian, Y., *et al.*, *Shape-controlled electrodeposition of gold nanostructures.* The Journal of Physical Chemistry B, *110* (**2006**) 23478.
55. Frank, A.C. and Sumodjo, P.T.A., *Electrodeposition of cobalt from citrate containing baths.* Electrochimica Acta, *132* (**2014**) 75.
56. Day, T.M., *et al.*, *Factors controlling the electrodeposition of metal nanoparticles on pristine single walled carbon nanotubes.* Nano Letters, *7* (**2006**) 51.
57. Siek, M., *et al.*, *Electrodeposition for preparation of efficient surface-enhanced raman scattering-active silver nanoparticle substrates for neurotransmitter detection.* Electrochimica Acta, *89* (**2013**) 284.
58. Khelladi, M.R., *et al.*, *Electrochemical nucleation and growth of copper deposition onto fto and n-si(1 0 0) electrodes.* Materials Chemistry and Physics, *115* (**2009**) 385.
59. Oskam, G. and et al., *Electrochemical deposition of metals onto silicon.* Journal of Physics D: Applied Physics, *31* (**1998**) 1927.
60. Cao, G., *et al.*, *Generation of gold nanostructures at the surface of platinum electrode by electrodeposition for ecl detection for ce.* Electrophoresis, *31* (**2010**) 1055.
61. Praig, V.G., *et al.*, *Seed-mediated electrochemical growth of gold nanostructures on indium tin oxide thin films.* Electrochimica Acta, *53* (**2008**) 7838.
62. Li, Y. and Shi, G., *Electrochemical growth of two-dimensional gold nanostructures on a thin polypyrrole film modified ito electrode.* The Journal of Physical Chemistry B, *109* (**2005**) 23787.
63. *Handbook of deposition technologies for films and coatings : Science, technology and applications*, R.F. Bunshah, Editor. 1994, Noyes Publications: Park Ridge, N.J. :.
64. Li, M., *et al.*, *Cobalt electrodeposition using urea and choline chloride.* Electrochimica Acta, *123* (**2014**) 325.
65. Serra , A., *et al.*, *One-step electrodeposition from ionic liquid and water as a new method for 2d composite preparation.* Electrochemistry Communications, *46* (**2014**) 79.
66. Lai, M. and Riley, D.J., *Templated electrosynthesis of nanomaterials and porous structures.* Journal of Colloid and Interface Science, *323* (**2008**) 203.
67. Sun, X.-Y., *et al.*, *Cyclic voltammetry for the fabrication of high dense silver nanowire arrays with the assistance of aao template.* Materials Chemistry and Physics, *90* (**2005**) 69.
68. Liu, H.-H., *et al.*, *Regular microarray of au flower-like structure formed by template-assisted electrodeposition: Influence factors and their electrochemical behavior.* Electrochimica Acta, *54* (**2009**) 7514.

69. Busbee, B.D., *et al.*, *An improved synthesis of high-aspect-ratio gold nanorods.* Advanced Materials, *15* (**2003**) 414.
70. Gao, F., *et al.*, *Electrochemical preparation of a au crystal with peculiar morphology and unique growth orientation and its catalysis for oxygen reduction.* Journal of The Electrochemical Society, *152* (**2005**) A1226.
71. Liu, G., *et al.*, *Trapeziform ag nanosheet arrays induced by electrochemical deposition on au-coated substrate.* Crystal Growth & Design, *8* (**2008**) 2748.
72. Gu, C. and Zhang, T.-Y., *Electrochemical synthesis of silver polyhedrons and dendritic films with superhydrophobic surfaces.* Langmuir, *24* (**2008**) 12010.
73. Tang, S. and Meng, X., *Controllable synthesis of metal particles by a direct current electrochemical approach.* Science in China Series E: Technological Sciences, *52* (**2009**) 2709.
74. Shang, L., *et al.*, *Electrochemical preparation of silver nanostructure on the planar surface for application in metal-enhanced fluorescence.* The Journal of Physical Chemistry C, *111* (**2007**) 10780.
75. He, P., *et al.*, *Electrochemical deposition of silver in room-temperature ionic liquids and its surface-enhanced raman scattering effect.* Langmuir, *20* (**2004**) 10260.
76. Zheng, X.-J., *et al.*, *Growth of silver nanowires by an unconventional electrodeposition without template.* Electrochemistry Communications, *9* (**2007**) 629.
77. Takahashi, Y. and Tatsuma, T., *Electrodeposition of thermally stable gold and silver nanoparticle ensembles through a thin alumina nanomask.* Nanoscale, *2* (**2010**) 1494.
78. Plieth, W., *et al.*, *Electrochemical preparation of silver and gold nanoparticles: Characterization by confocal and surface enhanced raman microscopy.* Surface Science, *597* (**2005**) 119.
79. Bian, J., *et al.*, *Double-potentiostatic electrodeposition of ag nanoflowers on ito glass for reproducible surface-enhanced (resonance) raman scattering application.* Electrochimica Acta, *67* (**2012**) 12.
80. Dogan, Ă., *et al.*, *Ag nanostructures on a poly(3,4-ethylenedioxythiophene) film prepared with electrochemical route: A controllable roughened sers substrate with high repeatability and stability.* Electrochimica Acta, *85* (**2012**) 220.
81. Jiang, F., *et al.*, *A rapid green route for fabricating efficient sers substrates.* Green Chemistry, *13* (**2011**) 2831.
82. Peraldo Bicelli, L., Bozzini, B., Mele, C., D'Urzo, L., *A review of nanostructural aspects of metal electrodeposition.* Int. J. Electrochem. Sci., *3* (**2008**) 356.
83. Zarkadas, G.M., *et al.*, *Influence of citric acid on the silver electrodeposition from aqueous agno3 solutions.* Electrochimica Acta, *50* (**2005**) 5022.
84. Mostany, J., *et al.*, *Electrochemical nucleation and the classical theory: Overpotential and temperature dependence of the nucleation rate.* Russian Journal of Electrochemistry, *44* (**2008**) 652.
85. Ramirez, C., *et al.*, *The effect of temperature on the kinetics and mechanism of silver electrodeposition.* Solid State Ionics, *169* (**2004**) 81.
86. Scheludko, A., Todorova, M., Bull. Acad. Bulg. Sci. Phys., *3* (**1952**).
87. Sandmann, G., *et al.*, *Preparation of silver nanoparticles on ito surfaces by a double-pulse method.* Journal of Electroanalytical Chemistry, *491* (**2000**) 78.
88. Sheridan, E., *Electrodeposited nanoparticles: Properties and photocatalytic applications.* 2009, Dublin City University.
89. Sheridan, E., *et al.*, *Electrodeposition of gold nanoparticles on fluorine-doped tin oxide: Control of particle density and size distribution.* Journal of Electroanalytical Chemistry, *608* (**2007**) 1.
90. Ivanova, O.S. and Zamborini, F.P., *Electrochemical size discrimination of gold nanoparticles attached to glass/indiumâˆ'tin-oxide electrodes by oxidation in bromide-containing electrolyte.* Analytical Chemistry, *82* (**2010**) 5844.
91. Ma, Y., *et al.*, *Direct electrodeposition of gold nanoparticles on indium tin oxide surface and its application.* Biosensors and Bioelectronics, *24* (**2009**) 1480.

92. Wang, J., *et al.*, *Disposable biosensor based on immobilization of glucose oxidase at gold nanoparticles electrodeposited on indium tin oxide electrode.* Sensors and Actuators B: Chemical, *135* (**2008**) 283.
93. Wang, L., *et al.*, *Direct electrodeposition of gold nanoparticles onto indium/tin oxide film coated glass and its application for electrochemical biosensor.* Electrochemistry Communications, *10* (**2008**) 673.
94. Wang, J., *et al.*, *Electrodeposition of gold nanoparticles on indium/tin oxide electrode for fabrication of a disposable hydrogen peroxide biosensor.* Talanta, *77* (**2009**) 1454.
95. Hu, Y., *et al.*, *Electrochemical synthesis of gold nanoparticles onto indium tin oxide glass and application in biosensors.* Thin Solid Films, *519* (**2011**) 6605.
96. Cheng, X.R., *et al.*, *Au nanoparticle-modified DNA sensor based on simultaneous electrochemical impedance spectroscopy and localized surface plasmon resonance.* Biosensors and Bioelectronics, *53* (**2014**) 513.
97. Sakai, N., *et al.*, *Electrodeposition of gold nanoparticles on ito: Control of morphology and plasmon resonance-based absorption and scattering.* Journal of Electroanalytical Chemistry, *628* (**2009**) 7.
98. El-Deab, M.S., *et al.*, *Morphological selection of gold nanoparticles electrodeposited on various substrates.* Journal of The Electrochemical Society, *152* (**2005**) C730.
99. Haes, A.J., *et al.*, *Plasmonic materials for surface-enhanced sensing and spectroscopy.* MRS Bulletin, *30* (**2005**) 368.
100. Dobrev, D., *et al.*, *Periodic reverse current electrodeposition of gold in an ultrasonic field using ion-track membranes as templates: Growth of gold single-crystals.* Electrochimica Acta, *45* (**2000**) 3117.
101. Hernandez-Santos, D., Gonzalez-Garcia, M., Costa-Garcia, A., *Effect of metals on silver electrodeposition: Application to the detection of cisplatin.* Electrochimica Acta, *50* (**2005**) 1895.
102. Bellus, D., *et al.*, *Science of synthesis: Houben-weyl methods of molecular transformations vol. 3: Compounds of groups 12 and 11 (zn, cd, hg, cu, ag, au).* 2014: Thieme.
103. Liu, H. and Penner, R.M., *Size-selective electrodeposition of mesoscale metal particles in the uncoupled limit.* The Journal of Physical Chemistry B, *104* (**2000**) 9131.
104. Gomez, E., *et al.*, *Electrodeposition of silver as a precursor matrix of magnetoresistive materials.* Materials Letters, *61* (**2007**) 1671.
105. EPA, U.S. *Perchlorate - toxicology*. 2014 28/12/2014]; Available from: http://clu-in.org/contaminantfocus/default.focus/sec/perchlorate/cat/Toxicology/.
106. Dai, X. and Compton, R.G., *Direct electrodeposition of gold nanoparticles onto indium tin oxide film coated glass: Application to the detection of arsenic(iii).* Analytical Sciences, *22* (**2006**) 567.
107. Ivanova, O.S. and Zamborini, F.P., *Electrochemical size discrimination of gold nanoparticles attached to glass/indiumâ□'tin-oxide electrodes by oxidation in bromide-containing electrolyte.* Analytical Chemistry, *82* (**2010**) 5844.
108. Turkevich, J., *et al.*, *A study of the nucleation and growth processes in the synthesis of colloidal gold.* Discussions of the Faraday Society, *11* (**1951**) 55.
109. Pillai, Z.S. and Kamat, P.V., *What factors control the size and shape of silver nanoparticles in the citrate ion reduction method?* Journal of Physical Chemistry B, *108* (**2004**) 945.
110. Chow, M.K. and Zukoski, C.F., *Gold sol formation mechanisms: Role of colloidal stability.* Journal of Colloid and Interface Science, *165* (**1994**) 97.
111. Rodríguez-González, B., *et al.*, *An electrochemical model for gold colloid formation via citrate reduction*, in *Zeitschrift für Physikalische Chemie*. 2007. p. 415.
112. Du, M., *et al.*, *Retention of virulence in a viable but nonculturable edwardsiella tarda isolate.* Applied and Environmental Microbiology, *73* (**2007**) 1349.

113. Ojea-Jimεnez, I. and Campanera, J.M., *Molecular modeling of the reduction mechanism in the citrate-mediated synthesis of gold nanoparticles.* The Journal of Physical Chemistry C, *116* (**2012**) 23682.
114. de Oliveira, G.M.*, et al.*, *Voltammetric study of the influence of edta on the silver electrodeposition and morphological and structural characterization of silver films.* Journal of Electroanalytical Chemistry, *578* (**2005**) 151.
115. Kaminska, I.*, et al.*, *Electrodeposition of gold nanoparticles at a solid|ionic liquid|aqueous electrolyte three-phase junction.* Electrochemistry Communications, *12* (**2010**) 1742.
116. Fu, C.*, et al.*, *Electrodeposition of gold nanoparticles from ionic liquid microemulsion.* Colloid and Polymer Science, *288* (**2010**) 1097.
117. Toledano, R. and Mandler, D., *Electrochemical codeposition of thin gold nanoparticles/sol-gel nanocomposite films.* Chemistry of Materials, *22* (**2010**) 3943.
118. Szunerits, S. and Boukherroub, R., *Introduction to plasmonics: Advances and applications*. 2015: CRC Press. 378.
119. Museum, T.B. *The lycurgus cup*. Available from: https://www.britishmuseum.org/explore/highlights/highlight_objects/pe_mla/t/the_lycurgus_cup.aspx.
120. Henderson, J., *The science and archaeology of materials: An investigation of inorganic materials*. 2013: Taylor & Francis.
121. Pines, D., *Collective energy losses in solids.* Reviews of Modern Physics, *28* (**1956**) 184.
122. Szunerits, S. and Boukherroub, R., *Introduction to plasmonics: Advances and applications*. 2015: Pan Stanford.
123. Jain, P.K.*, et al.*, *Noble metals on the nanoscale: Optical and photothermal properties and some applications in imaging, sensing, biology, and medicine.* Accounts of Chemical Research, *41* (**2008**) 1578.
124. Wang, X.*, et al.*, *Probing the location of hot spots by surface-enhanced raman spectroscopy: Toward uniform substrates.* ACS Nano, *8* (**2014**) 528.
125. Kumar, C.S.S.R., *Mixed metal nanomaterials*. 2009: Wiley.
126. Vaccari, A., *Modeling the interaction of light with photonic structures by direct numerical solution of maxwell's equations*. 2015, University of Trento.
127. Klimov, V., *Nanoplasmonics*. 2014: CRC Press.
128. Mayer, K.M. and Hafner, J.H., *Localized surface plasmon resonance sensors.* Chemical Reviews, *111* (**2011**) 3828.
129. Petryayeva, E. and Krull, U.J., *Localized surface plasmon resonance: Nanostructures, bioassays and biosensing - a review.* Analytica Chimica Acta, *706* (**2011**) 8.
130. Haes, A. and Duyne, R., *A unified view of propagating and localized surface plasmon resonance biosensors.* Analytical and Bioanalytical Chemistry, *379* (**2004**) 920.
131. Li, X.*, et al.*, *Localized surface plasmon resonance (lspr) of polyelectrolyte-functionalized gold-nanoparticles for bio-sensing.* Colloids and Surfaces A: Physicochemical and Engineering Aspects, *332* (**2009**) 172.
132. Haes, A.J. and Van Duyne, R.P., *A nanoscale optical biosensor: Sensitivity and selectivity of an approach based on the localized surface plasmon resonance spectroscopy of triangular silver nanoparticles.* J Am Chem Soc, *124* (**2002**) 10596.
133. Park, G.*, et al.*, *Full-color tuning of surface plasmon resonance by compositional variation of au@ag core–shell nanocubes with sulfides.* Langmuir, *28* (**2012**) 9003.
134. Lesniewski, A.*, et al.*, *Antibody modified gold nanoparticles for fast and selective, colorimetric t7 bacteriophage detection.* Bioconjugate Chemistry, *25* (**2014**) 644.
135. Cittadini, M.*, et al.*, *Graphene oxide coupled with gold nanoparticles for localized surface plasmon resonance based gas sensor.* Carbon, *69* (**2014**) 452.

136. Jain, P.K., *et al.*, *On the universal scaling behavior of the distance decay of plasmon coupling in metal nanoparticle pairs: A plasmon ruler equation.* Nano Letters, *7* (**2007**) 2080.
137. Li, M., *et al.*, *Plasmon-enhanced optical sensors: A review.* Analyst, *140* (**2015**) 386.
138. Jing, C., *et al.*, *A single gold nanorod as a plasmon resonance energy transfer based nanosensor for high-sensitivity cu(ii) detection.* Analyst, *139* (**2014**) 6435.
139. Choi, Y., *et al.*, *Plasmon resonance energy transfer (pret)-based molecular imaging of cytochrome c in living cells.* Nano Letters, *9* (**2009**) 85.
140. Robert, B., *Resonance raman spectroscopy.* Photosynthesis Research, *101* (**2009**) 147.
141. Nie, S. and Emory, S.R., *Probing single molecules and single nanoparticles by surface-enhanced raman scattering.* Science, *275* (**1997**) 1102.
142. Zou, S. and Schatz, G.C., *Silver nanoparticle array structures that produce giant enhancements in electromagnetic fields.* Chemical Physics Letters, *403* (**2005**) 62.
143. McQuillan, A.J., *The discovery of surface-enhanced raman scattering.* Notes and Records of the Royal Society, *63* (**2009**) 105.
144. Jeanmaire, D.L. and Van Duyne, R.P., *Surface raman spectroelectrochemistry: Part i. Heterocyclic, aromatic, and aliphatic amines adsorbed on the anodized silver electrode.* Journal of Electroanalytical Chemistry and Interfacial Electrochemistry, *84* (**1977**) 1.
145. Albrecht, M.G. and Creighton, J.A., *Anomalously intense raman spectra of pyridine at a silver electrode.* Journal of the American Chemical Society, *99* (**1977**) 5215.
146. Dieringer, J.A., *et al.*, *Introductory lecture surface enhanced raman spectroscopy: New materials, concepts, characterization tools, and applications.* Faraday Discussions, *132* (**2006**) 9.
147. Kneipp, K., *et al.*, *Single molecule detection using surface-enhanced raman scattering (sers).* Physical Review Letters, *78* (**1997**) 1667.
148. Le Ru, E.C., *et al.*, *Surface enhanced raman scattering enhancement factors: A comprehensive study.* The Journal of Physical Chemistry C, *111* (**2007**) 13794.
149. Wang, Y., *et al.*, *Electrodeposition of large size gold nanoparticles on indium tin oxide glass and application as refractive index sensor.* Electrochemistry Communications, *11* (**2009**) 1034.
150. Deng, J., *et al.*, *Label-free optical biosensor based on localized surface plasmon resonance of twin-linked gold nanoparticles electrodeposited on ito glass.* Biosens Bioelectron, *26* (**2010**) 615.
151. Zhu, J. and Deng, X.-c., *Improve the refractive index sensitivity of gold nanotube by reducing the restoring force of localized surface plasmon resonance.* Sensors and Actuators B: Chemical, *155* (**2011**) 843.
152. Deng, J., *et al.*, *Synthesis of ultrathin silver shell on gold core for reducing substrate effect of lspr sensor.* Electrochemistry Communications, *13* (**2011**) 1517.
153. Bhattarai, J.K., *et al.*, *Electrochemical synthesis of nanostructured gold film for the study of carbohydrate-lectin interactions using localized surface plasmon resonance spectroscopy.* Carbohydr Res, *405* (**2015**) 55.
154. Tao, H., *et al.*, *A plasmonic mercury sensor based on silver–gold alloy nanoparticles electrodeposited on indium tin oxide glass.* Electrochemistry Communications, *40* (**2014**) 75.
155. Deng, J., *et al.*, *Label-free optical biosensor based on localized surface plasmon resonance of twin-linked gold nanoparticles electrodeposited on ito glass.* Biosensors and Bioelectronics, *26* (**2010**) 615.
156. Yang, J., *et al.*, *Electrodeposition of silver nanoparticles on ito films with different thickness and application as lspr sensor.* ECS Electrochemistry Letters, *3* (**2014**) B30.

157. Yu, Y., *et al.*, *Growth and optical absorption properties of silver nanorod arrays in porous anodic aluminum oxide templates.* Wuhan University Journal of Natural Sciences, *17* (**2012**) 157.
158. Ye, W., *et al.*, *Electrochemical growth of flowerlike gold nanoparticles on polydopamine modified ito glass for sers application.* Electrochimica Acta, *55* (**2010**) 2004.
159. Sharma, D.K., *et al.*, *The facile formation of silver dendritic structures in the absence of surfactants and their electrochemical and sers properties.* Colloids and Surfaces A: Physicochemical and Engineering Aspects, *386* (**2011**) 98.
160. Zheng, J., *et al.*, *Comparison of the surface properties of the assembled silver nanoparticle electrode and roughened silver electrode.* The Journal of Physical Chemistry B, *106* (**2002**) 1019.
161. Bian, J., *et al.*, *Reproducible and recyclable sers substrates: Flower-like ag structures with concave surfaces formed by electrodeposition.* Applied Surface Science, *333* (**2015**) 126.
162. Lv, Z.-Y., *et al.*, *Shaped-controlled electrosynthesis of gold nanodendrites for highly selective and sensitive sers detection of formaldehyde.* Sensors and Actuators B: Chemical, *201* (**2014**) 92.
163. Bozzini, B., *et al.*, *A sers investigation of the electrodeposition of agâ€“au alloys from free-cyanide solutions.* Journal of Electroanalytical Chemistry, *563* (**2004**) 133.
164. Du, Y., *et al.*, *Sers enhancement dependence on the diameter and aspect ratio of silver-nanowire array fabricated by anodic aluminium oxide template.* Applied Surface Science, *255* (**2008**) 1901.
165. Fan, M., *et al.*, *A review on the fabrication of substrates for surface enhanced raman spectroscopy and their applications in analytical chemistry.* Analytica Chimica Acta, *693* (**2011**) 7.
166. Nogala, W., *et al.*, *Tailored gold nanostructure arrays as catalysts for oxygen reduction in alkaline media and a single molecule sers platform.* Nanoscale, *7* (**2015**) 10767.
167. Kęcki, Z., *Podstawy spektroskopii molekularnej.* 4th ed. 1998: Wydawnictwa Naukowe PWN.
168. Goldstein, J., Newbury, D.E., Joy, D.C., Lyman, C.E., Echlin, P., Lifshin, E., Sawyer, L., Michael, J.R., *Scanning electron microscopy and x-ray microanalysis.* 3rd edition ed. 2003: Springer.
169. Nikolic, N.D., *et al.*, *The potentiostatic current transients and the role of local diffusion fields in formation of the 2d lead dendrites from the concentrated electrolyte.* Journal of Electroanalytical Chemistry, *739* (**2015**) 137.
170. Zhang, J. and Oyama, M., *Gold nanoparticle arrays directly grown on nanostructured indium tin oxide electrodes: Characterization and electroanalytical application.* Analytica Chimica Acta, *540* (**2005**) 299.
171. Berkh, O., *et al.*, *The chemical and electrochemical activity of citrate on pt electrodes.* Journal of The Electrochemical Society, *158* (**2011**) F85.
172. Rycenga, M., *et al.*, *Controlling the synthesis and assembly of silver nanostructures for plasmonic applications.* Chemical Reviews, *111* (**2011**) 3669.
173. Schmid, G., *Nanoparticles: From theory to application.* 2006: Wiley.
174. Qin, Y., *et al.*, *Size control over spherical silver nanoparticles by ascorbic acid reduction.* Colloids and Surfaces A: Physicochemical and Engineering Aspects, *372* (**2010**) 172.
175. Raveendran, P., *et al.*, *A simple and "Green" Method for the synthesis of au, ag, and au-ag alloy nanoparticles.* Green Chemistry, *8* (**2006**) 34.
176. Wang, H., *et al.*, *Preparation of silver nanoparticles by chemical reduction method.* Colloids and Surfaces A: Physicochemical and Engineering Aspects, *256* (**2005**) 111.
177. Mehta, S.K., *et al.*, *Time dependence of nucleation and growth of silver nanoparticles generated by sugar reduction in micellar media.* Journal of Colloid and Interface Science, *343* (**2010**) 447.

178. Hussain, J.I., *et al.*, *Time dependence of nucleation and growth of silver nanoparticles.* Colloids and Surfaces A: Physicochemical and Engineering Aspects, *381* (**2011**) 23.
179. Shao, W. and Zhao, Q., *Influence of reducers on nanostructure and surface energy of silver coatings and bacterial adhesion.* Surface and Coatings Technology, *204* (**2010**) 1288.
180. Soukupova, J., *et al.*, *Silver voyage from macro- to nanoworld.* Journal of Chemical Education, *87* (**2010**) 1094.
181. Liebig, J., *Ueber versilberung und vergoldung von glas.* Justus Liebigs Annalen der Chemie, *98* (**1856**) 132.
182. Toghill, K.E., Compton, R. G., *Electrochemical non-enzymatic glucose sensors: A perspective and an evaluation.* Int. J. Electrochem. Sci., *5* (**2010**) 1246.
183. Sun, Y. and Xia, Y., *Shape-controlled synthesis of gold and silver nanoparticles.* Science, *298* (**2002**) 2176.
184. Tao, A., *et al.*, *Polyhedral silver nanocrystals with distinct scattering signatures.* Angewandte Chemie International Edition, *45* (**2006**) 4597.
185. Haaf, F., *et al.*, *Polymers of n-vinylpyrrolidone: Synthesis, characterization and uses.* Polym J, *17* (**1985**) 143.
186. Nobelprize.org. *Otto loewi - biographical.* 5 Apr 2015]; Available from: http://www.nobelprize.org/nobel_prizes/medicine/laureates/1936/loewi-bio.html.
187. Francis, P.T., *The interplay of neurotransmitters in alzheimer's disease.* CNS Spectr, *10* (**2005**) 6.
188. di Michele, F., *et al.*, *Neurosteroid and neurotransmitter alterations in parkinson's disease.* Frontiers in Neuroendocrinology, *34* (**2013**) 132.
189. Nutt, D.J., *Relationship of neurotransmitters to the symptoms of major depressive disorder.* J Clin Psychiatry, *69 Suppl E1* (**2008**) 4.
190. Morgan, P.T., *et al.*, *Cortical gaba levels in primary insomnia.* Sleep, *35* (**2012**) 807.
191. Nutt, D.J., *et al.*, *The dopamine theory of addiction: 40 years of highs and lows.* Nat Rev Neurosci, *16* (**2015**) 305.
192. Soreq, H., *Human cholinesterases and anticholinesterases.* 2012: Elsevier Science. 328.
193. Kneipp, K., *et al.*, *Surface-enhanced raman scattering and biophysics.* Journal of Physics: Condensed Matter, *14* (**2002**) R597.
194. Lee, N.S., *et al.*, *Surface-enhanced raman spectroscopy of the catecholamine neurotransmitters and related compounds.* Analytical Chemistry, *60* (**1988**) 442.
195. McGlashen, M.L., *et al.*, *Surface-enhanced raman scattering of dopamine at polymer-coated silver electrodes.* Analytical Chemistry, *62* (**1990**) 846.
196. Watanabe, M., *et al.*, *Determination of acetylcholine in human blood.* Biochemical Medicine and Metabolic Biology, *36* (**1986**) 355.
197. Ali, S., *et al.*, *A nonoxidative electrochemical sensor based on a self-doped polyaniline/carbon nanotube composite for sensitive and selective detection of the neurotransmitter dopamine: A review.* Sensors, *8* (**2008**) 8423.
198. Zeisel, S.H., *Choline: An essential nutrient for humans.* Nutrition, *16* (**2000**) 669.
199. Akutsu, H., *Direct determination by raman scattering of the conformation of the choline group in phospholipid bilayers.* Biochemistry, *20* (**1981**) 7359.
200. Blusztajn, J.K., *Choline, a vital amine.* Science, *281* (**1998**) 794.
201. Zeisel, S.H., *A brief history of choline.* Annals of Nutrition and Metabolism, *61* (**2012**) 254.
202. Lueders, C., *et al.*, *Evaluation of a chemiluminescent assay for analysis of choline in human plasma and whole blood.* Lab Medicine, *38* (**2007**) 726.
203. Mao, J., *et al.*, *A selective nmr method for detecting choline containing compounds in liver tissue: The 1hâ’14n hsqc experiment.* Journal of the American Chemical Society, *132* (**2010**) 17349.
204. Spratlin, J.L., *et al.*, *Clinical applications of metabolomics in oncology: A review.* Clinical Cancer Research, *15* (**2009**) 431.

205. Edsall, J.T., *Raman spectra of amino acids and related compounds. Vi. Sarcosine, ethanolamine, choline, betaine and betaine derivatives1.* Journal of the American Chemical Society, *65* (**1943**) 1767.
206. P. Gamache, Q.Z., K. Courtemanche. *Rapid analysis of choline in whole blood and plasma by high performance liquid chromatography with electrochemical detection.* in *Pittcon*. 2008. New Orleans, Louisiana, USA.
207. Holm, P.I.*, et al.*, *Determination of choline, betaine, and dimethylglycine in plasma by a high-throughput method based on normal-phase chromatographyâ€"tandem mass spectrometry.* Clinical Chemistry, *49* (**2003**) 286.
208. Yan, B. and Reinhard, B.r.M., *Identification of tumor cells through spectroscopic profiling of the cellular surface chemistry.* The Journal of Physical Chemistry Letters, *1* (**2010**) 1595.
209. Huang, Z.*, et al.*, *Raman spectroscopic characterization and differentiation of seminal plasma.* J Biomed Opt, *16* (**2011**) 110501.
210. Huang, T.T.*, et al.*, *Composite surface for blocking bacterial adsorption on protein biochips.* Biotechnology and Bioengineering, *81* (**2003**) 618.
211. Chang, B.S. and Mahoney, R.R., *Enzyme thermostabilization by bovine serum albumin and other proteins: Evidence for hydrophobic interactions.* Biotechnology and applied biochemistry, *22 (Pt 2)* (**1995**) 203.
212. Yamane, I.*, et al.*, *Role of bovine albumin in a serum-free suspension cell culture medium.* Experimental Biology and Medicine, *149* (**1975**) 439.
213. Gesztelyi, R.*, et al.*, *The hill equation and the origin of quantitative pharmacology.* Archive for History of Exact Sciences, *66* (**2012**) 427.
214. Arnaud, J.*, et al.*, *Binding sugars: From natural lectins to synthetic receptors and engineered neolectins.* Chem Soc Rev, *42* (**2013**) 4798.
215. Ambrosi, M.*, et al.*, *Lectins: Tools for the molecular understanding of the glycocode.* Org Biomol Chem, *3* (**2005**) 1593.
216. Imberty, A. and Varrot, A., *Microbial recognition of human cell surface glycoconjugates.* Curr Opin Struct Biol, *18* (**2008**) 567.
217. Varki, A., Cummings, R.D., Esko, J.D., et al., ed. *Essentials of glycobiology, 2nd edition*. 2009, Cold Spring Harbor Laboratory Press: Cold Spring Harbor (NY).
218. Bellapadrona, G.*, et al.*, *Optimization of localized surface plasmon resonance transducers for studying carbohydrate-protein interactions.* Analytical Chemistry, *84* (**2012**) 232.
219. Bhattarai, J.K.*, et al.*, *Electrochemical synthesis of nanostructured gold film for the study of carbohydrate-lectin interactions using localized surface plasmon resonance spectroscopy.* Carbohydrate Research, *405* (**2015**) 55.
220. Endo, T.*, et al.*, *Label-free detection of oligosaccharide-lectin interaction using plasmonic optical device for glycomics application.* Sensors and Materials, *23* (**2011**) 135.
221. Liu, X.*, et al.*, *Single gold nanoparticle localized surface plasmon resonance spectral imaging for quantifying binding constant of carbohydrate-protein interaction.* Analytical Chemistry, *85* (**2013**) 11851.
222. Ogiso, M.*, et al.*, *Carbohydrate immobilized on a dendrimer-coated colloidal gold surface for fabrication of a lectin-sensing device based on localized surface plasmon resonance spectroscopy.* Biosensors & Bioelectronics, *41* (**2013**) 465.
223. Yonzon, C.R.*, et al.*, *A comparative analysis of localized and propagating surface plasmon resonance sensors: The binding of concanavalin a to a monosaccharide functionalized self-assembled monolayer.* Journal of the American Chemical Society, *126* (**2004**) 12669.
224. Loris, R.*, et al.*, *The monosaccharide binding site of lentil lectin: An x-ray and molecular modelling study.* Glycoconj J, *11* (**1994**) 507.
225. Das, M.R.*, et al.*, *Synthesis of silver nanoparticles in an aqueous suspension of graphene oxide sheets and its antimicrobial activity.* Colloids and Surfaces B: Biointerfaces, *83* (**2011**) 16.
226. Yang, K.*, et al.*, *Preparation and functionalization of graphene nanocomposites for biomedical applications.* Nat. Protocols, *8* (**2013**) 2392.

227. Sutton, S. (2006) *The gram stain.* PMF NEWSLETTER **12**, 9.
228. *Differentiating gram-negative and gram-positive bacteria.* 2013 11.12.2014]; Available from: http://www.arrowscientific.com.au/index.php?option=com_content&view=article&id=48:differentiating-gram-negative-and-gram-positive-bacteria&catid=25&Itemid=40.
229. Wada A, K.M., Kawauchi S, Takagi Y, Morikawa T, Funakoshi K, *Rapid discrimination of gram-positive and gram-negative bacteria in liquid samples by using naoh-sodium dodecyl sulfate solution and flow cytometry.* PLoS ONE, *7* (**2012**).
230. Bogosian, G.B., Edward V, *A matter of bacterial life and death.* EMBO Reports, *2* (**2001**) 770.
231. Morishige, Y.*, et al.*, *Differential resuscitative effect of pyruvate and its analogues on vbnc (viable but non-culturable) salmonella.* Microbes and Environments, *28* (**2013**) 180.
232. Markx, G.H.*, et al.*, *Dielectrophoretic characterization and separation of micro-organisms.* Microbiology, *140* (**1994**) 585.
233. Liang, X.J.*, et al.*, *Determining refractive index of single living cell using an integrated microchip.* Sensors and Actuators A: Physical, *133* (**2007**) 349.
234. Prodan, E.*, et al.*, *The dielectric response of spherical live cells in suspension: An analytic solution.* Biophysical Journal, *95* (**2008**) 4174.
235. Esteban-Ferrer, D.*, et al.*, *Electric polarization properties of single bacteria measured with electrostatic force microscopy.* ACS Nano, *8* (**2014**) 9843.
236. Li, L.*, et al.*, *The importance of the viable but non-culturable state in human bacterial pathogens.* Frontiers in Microbiology, *5* (**2014**) 258.
237. Pethig, R. and Markx, G.H., *Applications of dielectrophoresis in biotechnology.* Trends in Biotechnology, *15* (**1997**) 426.
238. Jonsson, M.*, et al.*, *Bacteria counting with impedance spectroscopy in a micro probe station.* The Journal of Physical Chemistry B, *110* (**2006**) 10165.
239. Patel, P. and Markx, G.H., *Dielectric measurement of cell death.* Enzyme and Microbial Technology, *43* (**2008**) 463.
240. Kee, J.S.*, et al.*, *Plasmonic nanohole arrays for monitoring growth of bacteria and antibiotic susceptibility test.* Sensors and Actuators B: Chemical, *182* (**2013**) 576.
241. Baccar, H.*, et al.*, *Surface plasmon resonance immunosensor for bacteria detection.* Talanta, *82* (**2010**) 810.
242. Liu, F.*, et al.*, *Effects of nanoparticle size and cell type on high sensitivity cell detection using a localized surface plasmon resonance biosensor.* Biosensors and Bioelectronics, *55* (**2014**) 141.
243. Arana, I.*, et al.*, *Inability of escherichia coli to resuscitate from the viable but nonculturable state.* FEMS Microbiology Ecology, *62* (**2007**) 1.
244. Bolton, J.R., Cotton, Christine A. , *The ultraviolet disinfection handbook*. 2008: American Water Works Association. 150.
245. Singh, A.*, et al.*, *Recent advances in bacteriophage based biosensors for food-borne pathogen detection.* Sensors (Basel), *13* (**2013**) 1763.
246. Brzozowska, E.*, et al.*, *Funkcje białek bakteriofagowych.* Postępy Higieny i Medycyny Doświadczalnej, *65* (**2011**) 167
247. Clokie, M.R.J.*, et al.*, *Phages in nature.* Bacteriophage, *1* (**2011**) 31.
248. Adams, M.H., *Bacteriophages*. 1959: Interscience Publishers.
249. Shinde, S.B.*, et al.*, *Recent trends in in-vitro nanodiagnostics for detection of pathogens.* Journal of Controlled Release.
250. Nanduri, V.*, et al.*, *Phage as a molecular recognition element in biosensors immobilized by physical adsorption.* Biosensors and Bioelectronics, *22* (**2007**) 986.
251. Zourob, M.*, et al.*, *Principles of bacterial detection: Biosensors, recognition receptors and microsystems: Biosensors, recognition receptors, and microsystems*. 2008: Springer.

252. Smietana, M., *et al.*, *Detection of bacteria using bacteriophages as recognition elements immobilized on long-period fiber gratings.* Opt Express, *19* (**2011**) 7971.
253. Wu, L., *et al.*, *Trace detection of specific viable bacteria using tetracysteine-tagged bacteriophages.* Analytical Chemistry, *86* (**2014**) 907.
254. Lysiak, K., *Bacteriophages as an alternative to antibiotics - possibilities of their practical usage in dental surgery - review of literature.* Dent. Med. Probl., *41* (**2004**) 761.
255. Gilmartin, N. and O'Kennedy, R., *Nanobiotechnologies for the detection and reduction of pathogens.* Enzyme and Microbial Technology, *50* (**2012**) 87.
256. Hu, B., *et al.*, *The bacteriophage t7 virion undergoes extensive structural remodeling during infection.* Science, *339* (**2013**) 576.
257. Los, M., *et al.*, *Rapid detection of bacteriophage infection and prophage induction using electric biochips.* Microbial Cell Factories, *5* (**2006**) S38.
258. Dultsev, F., *et al.*, *Direct and quantitative detection of bacteriophage by "hearing" surface detachment using a quartz crystal microbalance.* Analytical Chemistry, *73* (**2001**) 3935.
259. Gabig-Ciminska, M., *et al.*, *Detection of bacteriophage infection and prophage induction in bacterial cultures by means of electric DNA chips.* Analytical biochemistry, *324* (**2004**) 84.
260. Grabow, W., *Bacteriophages: Update on application as models for viruses in water.* Water Sa, *27* (**2004**) 251.
261. Turgeon, N., *et al.*, *Comparison of five bacteriophages as models for viral aerosol studies.* Applied and Environmental Microbiology, *80* (**2014**) 4242.
262. O'Connell, K.P., *et al.*, *Real-time fluorogenic reverse transcription-pcr assays for detection of bacteriophage ms2.* Applied and Environmental Microbiology, *72* (**2006**) 478.
263. Scherberg, N.H. and Weiss, S.B., *Detection of bacteriophage t4-and t5-coded transfer rnas.* Proceedings of the National Academy of Sciences, *67* (**1970**) 1164.
264. García-Aljaro, C., *et al.*, *Surface plasmon resonance assay for real-time monitoring of somatic coliphages in wastewaters.* Applied and Environmental Microbiology, *74* (**2008**) 4054.
265. Ebner, A., *et al.*, *Comparison of different aminofunctionalization strategies for attachment of single antibodies to afm cantilevers.* Ultramicroscopy, *107* (**2007**) 922.
266. Kannan, P., *et al.*, *T7 bacteriophage induced changes of gold nanoparticle morphology: Biopolymer capped gold nanoparticles as versatile probes for sensitive plasmonic biosensors.* Analyst, *139* (**2014**) 3563.
267. Barbillon, G.g., *et al.*, *Biological and chemical gold nanosensors based on localized surface plasmon resonance.* Gold Bulletin, *40* (**2007**) 240.
268. Sagle, L.B., *et al.*, *Advances in localized surface plasmon resonance spectroscopy biosensing.* Nanomedicine (Lond), *6* (**2011**) 1447.
269. Lahav, A., *et al.*, *Sensitivity enhancement of guided-wave surface-plasmon resonance sensors.* Optics Letters, *33* (**2008**) 2539.